Max-Planck-Institut für Metallforschung
Stuttgart

On the Initial Oxidation of MgAl Alloys

M. S. Vinodh

Dissertation
an der
Universität Stuttgart

Bericht Nr. 182
Januar 2006

Max-Planck-Institut für Metallforschung
Stuttgart

On the Initial Oxidation of MgAl Alloys

M. S. Vinodh

Dissertation
an der
Universität Stuttgart

Bericht Nr. 182
Januar 2006

On the Initial Oxidation of MgAl Alloys

von der Fakultät Chemie der Universität Stuttgart
zur Erlangung der Würde eines Doktors der
Naturwissenschaften (Dr. rer. nat.) genehmigte Abhandlung

vorgelegt von

M. S. Vinodh

aus Erode/Indien

Hauptberichter:	Prof. Dr. Ir. E. J. Mittemeijer
Mitberichter:	Prof. Dr. Dr. h. c. M. Rühle
Mitprüfer:	Prof. Dr. F. Aldinger

Tag der Einreichung:	09.11.2005
Tag der mündlichen Prüfung:	16.01.2006

MAX-PLANCK-INSTITUT FÜR METALLFORSCHUNG STUTTGART
INSTITUT FÜR METALLKUNDE DER UNIVERSITÄT STUTTGART

Stuttgart 2006

Dedicated to my parents, brother and wife

Contents

Chapter 1

Introduction

1.1 General introduction

A fundamental and comprehensive understanding of the oxidation behaviour of metal and alloy surfaces is of great importance in a variety of different fields of research, development and application, such as heterogeneous catalysis [1, 2], integrated circuits [3], passivation of metals [4], or gas sensors [5]. Since the functional properties of the developing oxide films depend crucially on their microstructure (e.g. thickness, morphology, chemical composition, defect structure and oxide phase constitution), it is mandatory to have a comprehensive and in-depth understanding of the various processes that occur and the changes that take place at the substrate surface, in the developing oxide film, and at the substrate/oxide and oxide/gas interfaces during the initial and subsequent stages of oxide-film growth. In particular for the low temperature oxidation of alloy surfaces, as considered in this study, such knowledge of the relationships between the mechanism(s) that govern the oxide-film growth kinetics and the developing oxide-film microstructure as a function of the oxidation conditions (e.g. alloying content, partial oxygen pressure, oxidation time and temperature) lacks.

This study presents an investigation on the initial stages of oxide-film growth on bare, polycrystalline Mg-based MgAl alloys at room temperature as investigated by a combined approach of angle-resolved X-ray photoelectron spectroscopy (AR-XPS) and real-time in-situ spectroscopic ellipsometry (RISE). It addresses, in particular, the effects of the oxidation time, the bulk Al content, the partial oxygen pressure (pO_2) and the sputter-cleaning treatment (performed prior to each oxidation to remove the native oxide) on the oxide-film growth kinetics and the developing oxide-film microstructure. The complications that arise in the quantitative analysis of grown oxide films developing on binary alloy surfaces (as compared to the single-phase oxide film grown on a pure metal surface) by AR-XPS and RISE have been dealt with by the development of novel, accurate procedures for spectral evaluation and quantification.

Bare polycrystalline Mg-based MgAl substrates of various bulk Al alloying contents (i.e. 2.63, 5.78 and 7.31 at.%) were exposed at 304 K to pure oxygen gas in the pO_2 range of 10^{-6}-10^{-4} Pa. An UHV reaction chamber, which is directly coupled to the instrument for AR-XPS analysis, has been specially designed and constructed for these controlled oxidation experiments. The coupled UHV chambers are equipped with: (*i*) an ion-gun to clean the substrate surface prior to oxidation, (*ii*) a unit for the controlled admission of oxygen, (*iii*) a quadrupole mass spectrometer to monitor the residual gas content and control the pO_2 during growth, and (*iv*) the instrument for AR-XPS analysis of the bare and oxidized substrates and (*v*) an in-situ spectroscopic ellipsometer for dynamic analysis of the oxidizing alloy substrates. The microstructure of the grown oxide films has been determined using AR-XPS while RISE was applied to determine the oxide-film growth kinetics and the evolution of the oxide-film constitution (as evidenced from the variation of the optical constants of the growing oxide film).

1.2 Thermal oxidation of alloys at low temperatures

As for the thermal oxidation of pure metals, oxidation of a bare *alloy* surface proceeds via a series of steps, such as transport of oxygen molecules from the gas phase to the substrate surface, physisorption of O_2 molecules onto the surface, (dissociative) chemisorption, oxide nucleation and growth. After the formation of a closed oxide film covering the substrate surface, further oxide-film growth requires transport of (charged) species (possibly, cations, anions, electrons, holes and vacancies) through the developing oxide film towards the oxide-gas interface and/or the metal-oxide interface. If transport of one of the charged species occurs intrinsically at a relatively faster rate, then an electrostatic field develops within the growing oxide film, such that the transport of the intrinsically less mobile (i.e. rate-limiting) charged species is enhanced. Consequently, the transport of the charged species is determined by the gradients of both the chemical (related to the concentration) and electrostatic potentials in the developing oxide film (often referred to as the *electrochemical* potential gradients [6, 7]). Evidently, for the oxidation of an *alloy*, the additional concurrent processes of (oxidation-induced) chemical segregation and preferential oxidation, which induce compositional changes in the alloy subsurface during oxidation, also need to be adressed.

Up to date, investigations on the thermal oxidation of binary and ternary alloys have been mainly performed at high temperatures (i.e. $T > 800$ K) and high pressures (i.e. $0.1 < p < 10^5$ Pa), presumably because these conditions are relevant for the application of alloys in high-temperature-resistant coating systems (cf. Refs. [8-10]). At these high temperatures, local thermodynamic equilibrium generally prevails at the reacting metal/oxide, oxide/oxide and oxide/gas interfaces, and the thermal energy is sufficient to allow existing ions or electrons to surmount their energy barriers for movement into and through the developing oxide layer. Consequently, relatively thick (in the micrometer range) oxide scales, composed of multiple, crystalline oxide phases, develop on the alloy surface by sequential, preferential oxidation of the alloy constituents [8-10]. Then, continued oxide-layer growth is realized by the solid-state diffusion of charged reactants (i.e. cations, anions, electrons, vacancies and holes) through the developing oxide layer under the influence of the (electro)chemical potential gradients [11-13]. Once a dense, continuously-closed oxide scale has formed on the alloy surface, the oxidation kinetics obeys a parabolic growth law (cf. Refs. [9, 10]).

The thermal oxidation of binary and ternary alloys at low temperatures (of, say, $T <$ 600 K), on the other hand, has only been scarcely investigated up to date. At these low temperatures, the general assumption of local thermodynamic equilibria existing at the reacting metal/oxide, oxide/oxide and oxide/gas interfaces may not hold and the thermal energy is insufficient to allow existing ions or electrons to surmount their energy barriers for migration into and through the developing oxide film. Thus, the ionic and electronic transport rates through the developing oxide film by thermally activated (chemical) diffusion and thermionic emission of electrons in the conduction band of the oxide, respectively, are very small [14, 15]. Hence, an additional driving force, such as a surface-charge field set up by negatively charged oxygen species adsorbed at the developing oxide film surface [11, 13, 15], is required to explain the observed, initially very fast, and subsequent very slow, oxide-film growth kinetics (typically following a logarithmic or cubic growth law).

For the low-temperature oxidation of a bare alloy surface, one generally ends up with a thin oxide-film of near-limiting thickness (< 10 nm) that is constituted of a metastable, multi-element oxide phase (e.g. comprising an oxide solid solution, a spinel oxide phase and/or a doped oxide phase). However, in most cases, the detailed microstructure (i.e. oxide phase constitution, chemical composition, morphology and thickness) of the initial oxide-film formed on a bare alloy surface at low temperatures is unknown. For example, whereas an initially fully amorphous film is formed upon low-temperature oxidation of a bare Al metal surface [16], the corresponding structures of the initial oxide films formed on a bare Mg metal surface and a bare MgAl surface are unknown (presumably initially either fully amorphous or coherent crystalline). Further, no comprehensive knowledge exists on the effect of the concurrent processes of (oxidation-induced) chemical segregation and preferential oxidation on both the developing oxide-film microstructure and the induced compositional changes in the alloy subsurface at these low temperatures. Finally, it should be realized that for the very thin oxide films (< 3 nm) grown upon thermal oxidation of binary alloy surfaces at room temperature, a simple application of bulk oxide defect chemistry to explain the observed effect of the alloying constituent on the oxidation behavior may no longer be valid.

1.3 Mg-based MgAl alloys

Over the last decade, the need to produce lightweight components for the automotive and aerospace industries has focused new attention on the benefits of magnesium as a casting alloy. Magnesium combines a density two-thirds that of aluminum, which is only slightly higher than that of fiber-reinforced plastics. Addition of small amounts of aluminium to the base Mg metal improves its mechanical strength, corrosion properties and castability. The ductility and fracture toughness are gradually reduced with increasing bulk Al alloying content. The low density and high specific stiffness of magnesium-based alloys make them extremely attractive candidates for engineering applications where light weight is important (e.g. aerospace and automotive industries, laptop casings).

Despite their competitive material properties, the use of magnesium alloys is not fully realized yet, partly due to a perceived lack of corrosion resistance. The addition of aluminium is a long-known means of improving the corrosion resistance of Mg alloys [17, 18]. However, the mechanisms and limits of this improvement are still poorly understood.

1.4 Methods of characterization

Ultra-high-vacuum (UHV) chambers in combination with in situ surface-sensitive analytical techniques are prerequisites to investigate the initial oxidation of bare metal or alloy surfaces. In the present work, the combination of two powerful surface-sensitive analytical techniques, namely angle-resolved X-ray photoelectron spectroscopy (AR-XPS) and in situ multi-wavelength ellipsometry have been applied to study the initial and subsequent stages of oxide nucleation and growth on bare MgAl substrates.

1.4.1 Angle-resolved X-ray Photoelectron Spectroscopy (AR-XPS)

X-ray photoelectron spectroscopy has its origin in the investigations of the photoelectric effect (discovered by Hertz in 1887) in which X-rays were used as the exciting photon source. The technique employs the uniqueness of the kinetic energy of the photoelectrons that are ejected from the specific orbital(s) of a solid to determine the chemical state of solid atoms or ions. Recording a series of XPS spectra from a metal or alloy surface after various oxidations allows an accurate determination of the oxide-film thickness [14, 19, 20] and composition [14, 20, 21], as well as the chemical state of the constituent ions in the oxide film [22, 23], as a function of the oxidation conditions (i.e. time, temperature, partial oxygen pressure, substrate orientation, alloying content) for oxide-film thicknesses of the order of the attenuation length of the detected photoelectrons (i.e. up to about 6 nm).

The state-of-the-art, angle-resolved XPS (AR-XPS) instrument employed in the current investigation is based on the simultaneous recording of the emitted photoelectrons at various detection angles α (with respect to the sample surface). Since the escape depth is defined by the effective attenuation length (EAL, λ^{eff}) of the detected photoelectrons in the solid times the cosine of the detection angle α, i.e. $\lambda^{eff}\cos\alpha$, it follows that different depths within the oxide film are probed for different detection angles α. An angle-resolved measurement of the oxidized metal therefore additionally allows the investigation of the oxide-film morphology [21, 24] and constitution, expressed as the relative depth distribution of different chemical species within the oxide film [14, 20, 21, 24]).

The accuracy in the quantitative analysis of recorded X-ray photoelectron spectra depends on the methods used for the calculation (and subsequent subtraction) of the background of inelastically scattered electrons associated with each main peak in the measured spectra, as well as the functional descriptions employed for the reconstruction of the different intrinsic line shapes' contributions to the measured spectra (e.g. metallic, oxidic or plasmon peak shapes). For example, as demonstrated in Chapter 3 of this thesis, for the case of the core-level photoelectron spectra recorded from a bare or oxidized MgAl alloy substrate, the second bulk plasmon peak associated with the Mg 2p metallic main peak overlaps strongly with the Al 2p metallic main peak (Fig. 1.1). Consequently, errors in quantification will arise if this plasmon peak is not properly resolved from the Al 2p main peak.

In the present study on the initial thermal oxidation of bare Mg-based MgAl alloys at room temperature, AR-XPS has been employed to determine the oxide-film microstructure in terms of the thickness, morphology, constitution (i.e. the depth distribution of different chemical species), composition and defect structure of the grown oxide films as a function of the oxidation time, pO_2 and the bulk Al alloying content.

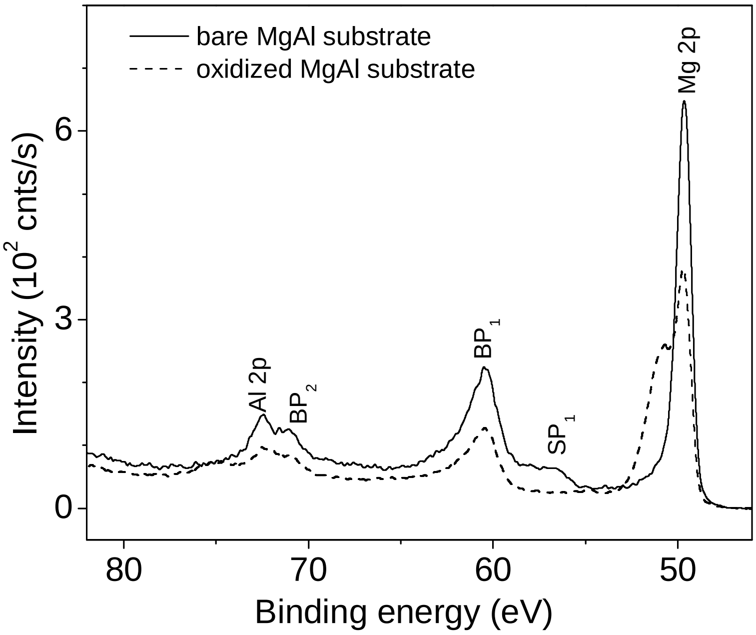

Figure 1.1. Measured Mg 2p – Al 2p spectra, as recorded from a bare Mg – 2.63 at.% Al substrate before (solid line) and after thermal oxidation (dashed line) for 1 h at 304 K and $pO_2 = 1\times10^{-4}$ Pa. The first and second bulk plasmon peaks and the first surface plasmon peak associated with the metallic Mg 2p main peak are indicated as BP_1, BP_2 and SP_1 respectively.

1.4.2 Real-time, In-situ Spectroscopic Ellipsometry (RISE)

The principle of ellipsometry is based on the measurement of the change in the polarization state of light reflected from the surface of the sample [25]. The measured parameters, ψ and Δ, represent the changes in amplitude and phase of the polarized light, reflected from the analyzing surface. More specific, ψ is the angle whose tangent equals the ratio of the amplitude attenuation (or magnification) upon reflection for the p and s polarizations (i.e. the components of the electric field vector of the polarized light vibrating in the plane of incidence and perpendicular to it, respectively); Δ is the difference between the phase shifts experienced upon reflection by the p and s polarizations.

Real-time, in-situ spectroscopic ellipsometry (RISE) provides a dynamic, non-destructive analysis of the oxide films during growth (i.e. the specimen can be monitored continuously as oxidation proceeds) (cf. Fig. 1.2). The spectroscopic ellipsometer used in the present work is equipped with a Xe polarized light source, covering a wavelength (λ) range from 250 to 900 nm, thereby obtaining information on the variation of Δ and ψ as a function of both the oxidation time and the wavelength.

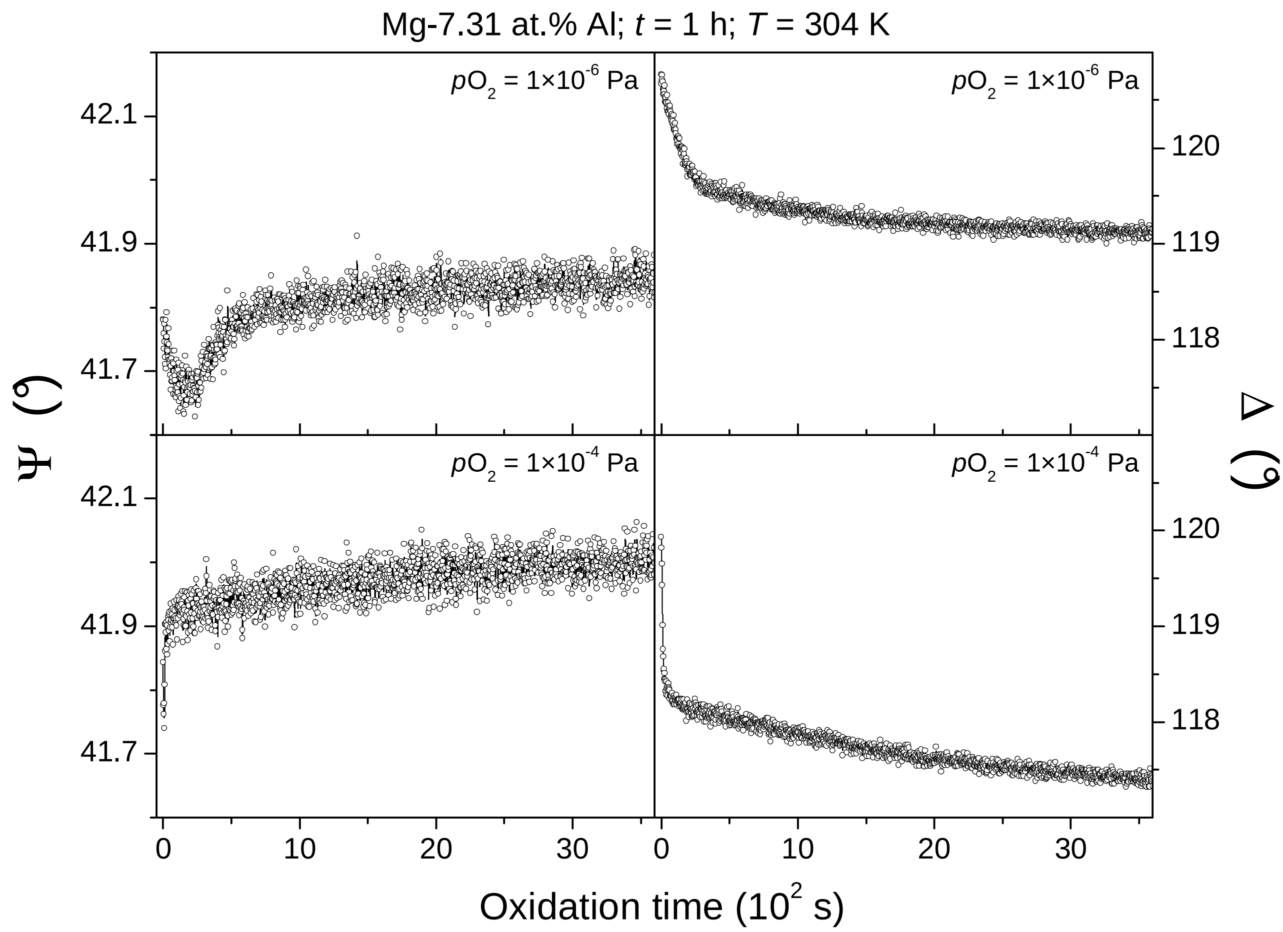

Figure 1.2. Measured values of ψ (*left panels*) and Δ (*right panels*) as a function of oxidation time (at a wavelength of λ = 525 nm) for the oxidation of a bare Mg – 7.31 at.% Al substrate at 304 K for 1 h at $pO_2 = 1\times10^{-6}$ Pa (*upper panels*) and $pO_2 = 1\times10^{-4}$ Pa (*lower panels*).

In the present study on the initial thermal oxidation of bare Mg-based MgAl alloys at room temperature, such RISE measurements were applied to determine the kinetics of oxide-film growth and the development of the oxide-film constitution at various pO_2's and for various bulk Al alloying contents (Chapter 5). To this end, a model has been developed which describes the measured time dependence of the spectra of $\Delta(\lambda)$ and $\psi(\lambda)$ for the initial and subsequent stages of oxidation (Chapter 4).

1.5 Outline of the thesis

Chapter 2 presents a fundamental investigation on the effects of the anisotropy of the photoionization cross-sections and elastic scattering of the detected photoelectrons in the solid on the quantitative analysis of the AR-XPS spectra recorded in parallel data acquisition mode. The procedures for spectra evaluation and subsequent quantification of the measured Mg 2p, Al 2p and O 1s AR-XPS spectra recorded from the bare and oxidized MgAl alloy substrates is the focus of the Chapter 3. In Chapter 4, a model has been developed to determine the growth kinetics of very thin (< 3 nm) oxide films developing on the bare MgAl substrates from the measured changes of the ellipsometric amplitude ratio and phase shift dependent parameters, ψ and Δ, versus wavelength, as recorded by real-time, in-situ spectroscopic ellipsometry. Finally, the thus obtained results on the growth kinetics and developing microstructure of thin oxide films (< 3 nm) grown on bare MgAl substrates by thermal oxidation at room temperature as a function of the oxidation time, the pO_2 (in the range of 10^{-6} – 10^{-4} Pa) and for various bulk Al alloying contents are discussed in Chapter 5.

Chapter 2

Quantitative analysis of angle-resolved XPS spectra recorded in parallel data acquisition mode

M.S. Vinodh, L.P.H. Jeurgens

Abstract

The effects of the anisotropy of the photoionization cross-section and elastic scattering of photoelectrons in the solids are investigated for angle-resolved XPS spectra (AR-XPS) recorded from α–Al_2O_3 substrate in parallel data acquisition mode. It is shown that, for the quantitative analysis of AR-XPS spectra recorded in parallel data acquisition mode, it is essential to account for the anisotropies of the photoionization cross-sections of the detected photoelectrons for the concerned elements in the solid due to the variation of the angle between the incident X-rays and the detected photoelectrons. Neglecting the effect of elastic scattering only leads to minor errors in the quantitative analysis of the AR-XPS spectra. By adopting experimentally determined values for the relative sensitivity factors of the concerned photoelectrons in the solid as a function of the detection angle, cumbersome corrections for the effects of the anisotropy of the photoionization cross-sections and elastic scattering can be avoided.

2.1 Introduction

In a conventional XPS instrumental setup, Angle-Resolved X-ray Photoelectron Spectroscopic (AR-XPS) measurements are performed by tilting the specimen, thereby maintaining a fixed angle ϕ between the incident X-rays and the analyzer (i.e. the detected electrons; see Fig. 2.1). In general, the angle ϕ is chosen to be close to 54°, corresponding to the so-called 'magic angle'. At this specific angle of ϕ, the effect of anisotropy of the photoionization cross-section on the recorded photoelectron intensity cancels out and, hence, the *total* photoionization cross-sections, σ, for the detected photoelectrons of the concerned elements in the solid can directly be used for quantification (see Sec. 2.2 and e.g. Refs. [26-28]). The total photoionization cross-section σ_{AX_n} is defined as the transition probability (per unit time) for exciting a photoelectron from the n^{th} subshell of core-level shell X of element A in the solid per unit incident photon flux.

The Thermo VG "Thetaprobe" instrument employed in the present investigation has the capability of detecting photoelectrons over a wide angular range without tilting the sample (so-called parallel data acquisition mode), which greatly speeds up the recording of a series of AR-XPS spectra. Further advantages, as compared to a conventional AR-XPS setup, are that the analyzed area and position remain constant, i.e. they are independent of the photoelectron detection angle α (with respect to the sample surface normal; see Fig. 2.1).

For an AR-XPS measurement recorded in parallel data acquisition mode, the solid angle of acceptance of the analyzer is divided into numerous channels, with each channel corresponding to a particular angular detection range (with a maximum possible 96 channels divided over a total detection range of α = 23 - 83°, in the present case). This implies that, in contrast to a conventional XPS setup, the angle ϕ between the incident X-rays and detected photoelectrons is not a constant, but varies with the detection angle α (see Fig. 2.1). As demonstrated in the present study, accurate quantitative analysis of these AR-XPS spectra then requires knowledge of the anisotropy of the photoionization cross-section for each core-level photoelectron line studied (see Sec. 2.2). This implies that, instead of the *total* photoionization cross-sections σ, as used in the quantification of conventional AR-XPS measurements, now the *differential* photoionization cross-sections, $d\sigma/d\Omega$, of the elements in the solid must be employed in the quantification. The differential photoionization cross-section describes the angular distribution of the emitted photoelectrons as a function of solid acceptance angle, and its value depends on the angle ϕ, between the directions of the incident

X-rays and the detected photoelectrons, the orbital angular quantum number and kinetic energy of the concerned photoelectrons (see Sec. 2.2).

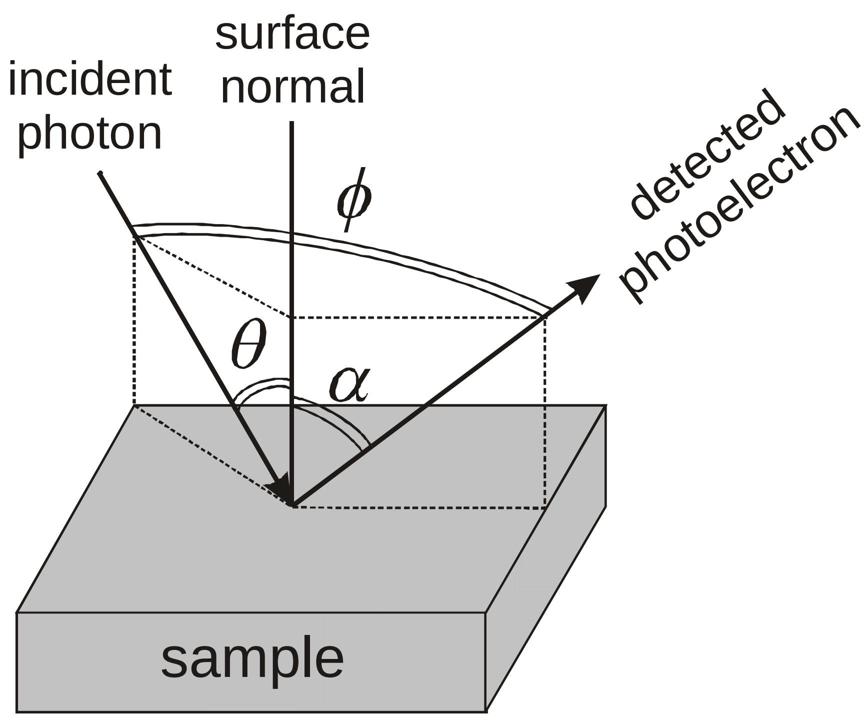

Figure 2.1. Schematic illustration of the interaction of incident photon with the sample surface: θ is the angle between the directions of the incident photon and the sample surface normal; α is the angle between the directions of the detected photoelectron and the sample surface normal; and ϕ is the angle between the directions of the incident photon and the detected photoelectron.

The present study investigates the effects of the anisotropy of the photoionization cross-section and elastic scattering of the emitted photoelectrons in the solid on the quantitative analysis of AR-XPS spectra recorded in parallel data acquisition mode. As a case study, the relative sensitivity factor (S) for the O 1s to Al 2p photoemission process in α-Al_2O_3 as a function of the angles α and ϕ is determined from their corresponding AR-XPS spectra recorded in parallel data acquisition mode. Such experimentally determined sensitivity factors (S) for various angles α and ϕ can be employed to calculate the composition, film thickness, or depth distributions of various oxidic species, for example, in thin oxide films grown on metal substrates by thermal oxidation (cf. Ref. [22]). The results will provide a framework for the interpretation of AR-XPS spectra as recorded with the state-of-the-art AR-XPS instruments employing parallel data acquisition mode.

In Sec. 2.2, the theory on the anisotropy of the photoionization cross-section, as well as the correction factors involved in quantification of AR-XPS spectra (with and without accounting for the effects of elastic scattering) are presented. Also, a simple method for the determination of relative sensitivity factors from measured AR-XPS spectra is given. Experimental details and the data evaluation procedure are given in Sec. 2.3. Finally, the results and discussion, in terms of the effects of the anisotropies of the photoionization cross-sections and elastic scattering on the relative O 1s to Al 2p sensitivity factor, as determined from the AR-XPS measurement of α-Al_2O_3 (in parallel data acquisition mode), are presented in Sec. 2.4.

2.2 Theory

The observed primary zero-loss (PZL) intensity $I^{\infty}_{AX_n}$ (cf. Ref. [29]) of photoelectrons ejected with a kinetic energy E from the n^{th} subshell of core-level shell, X, of an element A distributed within a solid, can be expressed by (cf. Ref. [30])

$$I^{\infty}_{AX_n} = K \cdot \left({d\sigma_{AX_n}}/{d\Omega} \right) \cdot \int_{z=0}^{\infty} C_A(z) \cdot \exp\left[-\int_{z'=0}^{z} \frac{dz'}{\lambda^{\mathrm{i}}_{AX_n}(z',E) \cdot \cos\alpha} \right] dz \qquad \textbf{(2.1)}$$

where K is an instrumental factor depending on factors such as area of analysis, energy and flux of the incident X-rays and solid acceptance angle of the analyzer (cf. Ref. [30]); the detection angle α is defined as the angle between the specimen surface normal and the solid acceptance angle of the analyzer (see Fig. 2.1); $C_A(z)$ is the atomic density of element A in the solid as a function of depth z below the sample surface; $\lambda^{\mathrm{i}}_{AX_n}(z,E)$ is the inelastic mean free path (IMFP) of the detected photoelectrons traversing with kinetic energy E through the solid as a function of depth z below the sample surface; and $\left(d\sigma_{AX_n}/d\Omega \right)$ is the differential photoionization cross-section. The depth dependence of IMFP due to possible changes in composition (as experienced for e.g. thin metal-oxide film systems when proceeding from the substrate to the oxide-film, cf. Ref. [30]) is accounted for by the second integral over dz'. In Eq. (2.1) the effect of elastic scattering of the photoelectrons propagating through the solid has been neglected.

2.2.1 *Anisotropy of photoionization cross-section*

The differential photoionization cross-section, $\left(d\sigma_{AX_n}/d\Omega \right)$ obtained in the dipole approximation (cf. p. 42 in Ref. [27]) for unpolarised X-rays and a randomly oriented set of atoms (or molecules) in the solid, as appropriate to studies of gaseous, polycrystalline or amorphous specimens, is expressed by (cf. Refs. [26, 28])

$$\left(d\sigma_{AX_n}/d\Omega\right)=\sigma_{AX_n}W(\phi,\beta_{AX_n})=\frac{\sigma_{AX_n}}{4\pi}\left[1-\frac{\beta_{AX_n}}{4}\left(3\cos^2\phi-1\right)\right] \quad \textbf{(2.2)}$$

where σ_{AX_n} is the total photoionization cross-section (integrated over the full 4π range for a given angle ϕ between the directions of the incident photon beam and the ejected photoelectrons; see Fig. 2.1), defined as the transition probability (per unit time) of emitting a photoelectron from the n^{th} subshell of core-level, X, of element A in the solid per unit incident photon flux; $W(\phi,\beta_{AX_n})$ is the asymmetry factor describing the intrinsic anisotropy of the photoionization cross-section; and β_{AX_n} is the asymmetry parameter, describing the angular distribution of the ejected photoelectrons concerned.

The allowed range for the asymmetry parameter β_{AX_n} is determined by the requirement that the cross-section should be non-negative (cf. Ref. [27]), i.e. $-1 \leq \beta_{AX_n} \leq 2$. A positive value of β_{AX_n} implies that photoelectrons are preferentially emitted at angles perpendicular to the direction of the incident photons (i.e. ϕ = 90°), whereas a negative value indicates preferential emission parallel or anti-parallel to this direction (i.e. ϕ = 0° or 180°). A value of β_{AX_n} = 0 yields an isotropic distribution. The exact value of β_{AX_n} depends upon the orbital angular momentum quantum number l (i.e. the type of subshell) and the kinetic energy of the emitted photoelectrons (and thus on the incident photon energy $h\nu$), where for all s-type subshells (i.e. l = 0) the value of β_{AX_n} = 2. Values of β_{AX_n} are tabulated in the literature only for elements in their gas phase (cf. Refs. [31-33]).

As follows from Eq. (2.2), due to the anisotropy of the photoionization cross-section, the recorded photoelectron intensity depends on the angle ϕ between the directions of the incident photons and the detected photoelectrons (see Fig. 2.1). In a conventional XPS setup, the X-ray source and the analyzer are fixed, and the angle between them is usually chosen close or equal to the so-called magic angle of ϕ = 54.74°, for which the β-dependent term on the right-hand side of Eq. (2.2) vanishes. In this case, even for angle-resolved measurements (obtained as a function of the detection angle α for a fixed angle of ϕ by tilting the sample; see Fig. 2.1), no correction for the anisotropy of the photoionization cross-section $W(\phi,\beta_{AX_n})$ is required upon quantification. This implies that only the total photoionization cross-section is required for the quantification of these AR-XPS spectra.

On the other hand, for a state-of-the-art AR-XPS measurement employing parallel data acquisition mode, the signal intensities are collected simultaneously over a wide range of detection angles α, while fixing both the sample position and the angle θ between the incident photon beam and the sample normal (see Fig. 2.1). Consequently, the angle ϕ does vary with the detection angle α, and separate values of $W(\phi, \beta_{AX_n})$ are required upon quantification for each detection angle concerned (see Sec. 2.4).

2.2.2 Effect of elastic scattering

Elastic scattering of emitted photoelectrons in a solid affects the distribution of the photoelectron trajectories, i.e. it partially randomizes the direction of electron motion. Consequently, the *observed* anisotropy of the differential photonionization cross-section of an element in the solid differs from the corresponding *intrinsic* anisotropy of the differential photonionization cross-section of the isolated atom; i.e. the anisotropy as observed for solids is a little less pronounced (the asymmetry parameter β_{AX_n} is relatively lower). The results of Monte Carlo (MC) simulations (cf Refs. [34, 35]) have shown that the effect of elastic scattering in solids can be accounted for by replacing the cross-section $\left(d\sigma_{AX_n}/d\Omega\right)$ of Eq. (2.1) with an effective differential photonionization cross-section, defined as

$$\left(d\sigma_{AX_n}/d\Omega\right)_{\text{eff}} = \sigma_{AX_n} W(\phi, \beta^{\text{eff}}_{AX_n}) = \sigma_{AX_n} Q_{AX_n} \frac{1}{4\pi}\left[1 - \frac{\beta^{\text{eff}}_{AX_n}}{4}\left(3\cos^2\phi - 1\right)\right] \qquad \textbf{(2.3a)}$$

where $\beta^{\text{eff}}_{AX_n}$ denotes the effective asymmetry parameter describing the actual, observed angular distribution of the measured photoelectron intensities, and Q_{AX_n} is a weak correction factor (ranging between 0.9 and 1) accounting for the reduction in the overall escape probability of photoelectrons due to elastic scattering within the solid (i.e. it describes the relative change in the observed photoelectron intensities due to elastic collisions). The incorporation of $\left(d\sigma_{AX_n}/d\Omega\right)_{\text{eff}}$ in Eq. (2.1) is equivalent to replacing the IMFP in Eq. (2.1) (i.e. $\lambda^{\text{i}}_{AX_n}$) by an effective attenuation length (EAL), $\lambda^{\text{eff}}_{AX_n}$, defined as (cf. Ref. [36])

$$\lambda^{\text{eff}}_{AX_n} = \lambda^{\text{i}}_{AX_n} Q_{AX_n} \frac{W(\phi, \beta^{\text{eff}}_{AX_n})}{W(\phi, \beta_{AX_n})} \qquad \textbf{(2.3b)}$$

Accurate expressions for the parameters Q_{AX_n} and $\beta^{\text{eff}}_{AX_n}$, as obtained within the so-called transport approximation, which neglects the structure in the differential elastic scattering cross sections (i.e. isotropic elastic scattering is assumed), are given by (cf. Ref. [37])

$$Q_{AX_n} = (1-\omega)\cdot(D_1 + D_2) \qquad \textbf{(2.4a)}$$

and

$$\beta_{AX_n}^{\text{eff}} = (1-\omega)\cdot\frac{\beta_{AX_n}}{Q_{AX_n}} \qquad \textbf{(2.4b)}$$

where

$$D_1 = \frac{H(\cos\alpha,\omega)}{\sqrt{(1-\omega)}} \qquad \textbf{(2.4c)}$$

and

$$D_2 = \frac{\omega\beta_{AX_n}}{16}\cdot(3\cos^2\phi-1)\cdot H(\cos\alpha,\omega)\cdot\int_0^1 x\cdot H(x,\omega)\cdot(x+\cos\alpha)^{-1}\cdot(3x^2-1)dx \qquad \textbf{(2.4d)}$$

In the above equations, ω is the so-called single scattering albedo defined as

$$\omega = \left(1+\lambda_{AX_n}^{\text{tr}}\Big/\lambda_{AX_n}^{\text{i}}\right)^{-1} \qquad \textbf{(2.5a)}$$

where $\lambda_{AX_n}^{\text{tr}}$ denotes the transport mean free path (TMFP) of the concerned photoelectrons of kinetic energy E in the solid, which for a solid compound consisting of m components is given by (cf. Ref. [38]),

$$\lambda_{AX_n}^{\text{tr}} = \left(M\sum_{k=1}^{m} x_k\sigma_{\text{tr},k}\right)^{-1} \qquad \textbf{(2.5b)}$$

Here, M is the total atomic density of the compound, x_k is the atom fraction of the k^{th} component in the compound and $\sigma_{\text{tr},k}$ represents the transport scattering cross-section of the k^{th} component for the concerned photoelectrons with kinetic energy E (cf. Ref. [38]). Finally, the term $H(\cos\alpha,\omega)$ in Eqs. (2.4c-d) is the Chandrasekhar function (Ref. [39]) which can either be solved by an iterative procedure (see Refs. [39]) (A matlab script to solve the function of Chandrasekar, $H(x, \omega)$, for any value of $0 \le x \le 1$ and $0 \le \omega \le 1$ by an iterative procedure can be obtained upon request from the corresponding author) or approximated by an analytical expression (cf. Ref. [36]).

The term D_2 in Eq. (2.4a) is generally neglected, because its value is in all cases considerably smaller than the value for the D_1 term (cf. Refs. [36, 37]). Further, it is noted that, for pure elements, simpler, approximate expressions for the estimation of the factors Q_{AX_n} and the $\beta_{AX_n}^{\text{eff}}$ are reported in the literature (cf. Ref. [40]).

2.2.3 Relative sensitivity factor in binary solids

Adopting Eqs. (2.1), (2.2) and (2.3b), it follows that the composition (i.e. the atomic ratio) of a homogeneous, infinitely thick (as compared to the IMFP), binary compound AB is related to the measured total primary zero-loss (PZL) photoelectron intensities $I_{AX_n}^{\infty}$ and $I_{BY_m}^{\infty}$, as recorded from the elements A and B in the solid, by

$$\frac{C_A}{C_B} = \frac{I_{AX_n}^{\infty}}{I_{BY_m}^{\infty}} \cdot \frac{\lambda_{BY_m}^{\mathrm{eff}}}{\lambda_{AX_n}^{\mathrm{eff}}} \cdot \frac{\sigma_{BY_m} W(\phi, \beta_{BY_m})}{\sigma_{AX_n} W(\phi, \beta_{AX_n})} = \frac{I_{AX_n}^{\infty}}{I_{BY_m}^{\infty}} \cdot \frac{\lambda_{BY_m}^{\mathrm{i}}}{\lambda_{AX_n}^{\mathrm{i}}} \cdot \frac{\sigma_{BY_m}}{\sigma_{AX_n}} \cdot \frac{Q_{BY_m} W(\phi, \beta_{BY_m}^{\mathrm{eff}})}{Q_{AX_n} W(\phi, \beta_{AX_n}^{\mathrm{eff}})} \qquad \textbf{(2.6a)}$$

where $I_{AX_n}^{\infty}$ and $I_{BY_m}^{\infty}$ denote the PZL intensities of the photoelectrons emitted from the n^{th} and m^{th} subshell of core-level shells X and Y of elements A and B within the (infinitely thick) solid, respectively. The relative sensitivity factor S_{AX_n/BY_m} for the AB reference compound with a known atomic ratio C_A/C_B is then defined as

$$S_{AX_n/BY_m} = \frac{C_B}{C_A} \cdot \frac{I_{AX_n}^{\infty}}{I_{BY_m}^{\infty}} = \frac{\lambda_{AX_n}^{\mathrm{eff}}}{\lambda_{BY_m}^{\mathrm{eff}}} \cdot \frac{\sigma_{AX_n} W(\phi, \beta_{AX_n})}{\sigma_{BY_m} W(\phi, \beta_{BY_m})} = \frac{\lambda_{AX_n}^{\mathrm{i}}}{\lambda_{BY_m}^{\mathrm{i}}} \cdot \frac{\sigma_{AX_n}}{\sigma_{BY_m}} \cdot \frac{Q_{AX_n} W(\phi, \beta_{AX_n}^{\mathrm{eff}})}{Q_{BY_m} W(\phi, \beta_{BY_m}^{\mathrm{eff}})} \qquad \textbf{(2.6b)}$$

Consequently, the relative sensitivity factor incorporates the combined effects of:

- The relative difference in the EALs $\lambda_{AX_n}^{\mathrm{eff}}$ and $\lambda_{BY_m}^{\mathrm{eff}}$ as a function of the angles α and ϕ (i.e. the relative difference in inelastic and elastic scattering of the concerned photoelectrons during their transport through the solid).
- The relative difference in the total photoionization cross-sections σ_{AX_n} and σ_{BY_m} (independent of α and ϕ).
- The relative difference in the asymmetry factors $W(\phi, \beta_{AX_n})$ and $W(\phi, \beta_{BY_m})$ as a function of the angle ϕ (i.e. the relative difference in the anisotropy in the angular distribution of the concerned photoelectrons).

As follows from Eq. (2.6b), the value for S_{AX_n/BY_m} as a function of the angle ϕ and/or the detection angle α (see Fig. 2.1) can simply be determined experimentally from the PZL intensity ratio $I_{AX_n}^{\infty}/I_{BY_m}^{\infty}$, as obtained from a series of measured XPS spectra recorded from the reference compound for a various set of angles of ϕ and α.

In a conventional XPS setup (for which the angle ϕ is fixed for various detection angles α, see Sec. 2.2.1), the experimentally obtained value of S_{AX_n/BY_m} should be independent of the detection angle α, provided that the EAL ratio $\lambda_{AX_n}^{\mathrm{eff}}/\lambda_{BY_m}^{\mathrm{eff}}$ is a constant and no photoelectron diffraction effects occur (as is valid for polycrystalline and amorphous solids). Moreover, if such a series of measurements is made at the magic angle of ϕ, the asymmetry factor ratio in Eq. (2.6b) vanishes (see Sec. 2.2.1).

On the other hand, for a similar AR-XPS measurement employing parallel data acquisition mode (for which the angle ϕ varies with the detection angle α, see Sec. 2.2.1), S_{AX_n/BY_m} does depend upon the detection angle α due to the accompanied change in the angle ϕ (see Fig. 2.1). Only for the special case where both subshells *n* and *m* are of the s-type (i.e. $\beta_{AX_n} = \beta_{AY_m} = 2$), the experimentally obtained value of S_{AX_n/BY_m} is independent of the detection angle α (again provided that $\lambda_{AX_n}^{\text{eff}} \big/ \lambda_{BY_m}^{\text{eff}}$ is a constant and no photoelectron diffraction effects occur).

Knowledge of the dependence of the value of S_{AX_n/BY_m} with the angles ϕ and α is required for the quantification of AR-XPS spectra recorded from binary compounds of unknown composition, as well as from thin layered structures on substrates (as, for example, in the determination of thicknesses and compositions of thin oxide films on metal substrates; cf. Ref. [22]). In the next section, the variation of the relative sensitivity factor $S_{\mathrm{O\,1}s/\mathrm{Al\,2}p}$ with the interdependent angles ϕ and α will be investigated for the AR-XPS spectra recorded in parallel data acquisition mode from an α-Al_2O_3 reference with a known O/Al atomic ratio of 1.5. The thus obtained values of $S_{\mathrm{O\,1}s/\mathrm{Al\,2}p}$ as a function ϕ and α may be adopted in the quantification of AR-XPS spectra recorded from e.g. thin Al-oxide films grown on Al substrates by thermal oxidation (cf. Ref. [22]).

2.3 Experimental & data evaluation

A one-side polished (< 0.25 μm), $(1\bar{1}00)$ oriented α-Al_2O_3 single crystal with an O/Al-ratio of 1.5 (purity < 99.99% supplied by Goodfellow Cambridge Ltd.) was thoroughly cleaned ultrasonically in acetone, ethanol and subsequently 2-propanol, and then dried by blowing with pure compressed nitrogen gas. Next, the sample was introduced into the UHV chamber for XPS analysis, with a base pressure of < 3×10^{-8} Pa. First, the adventitious carbon and any other contaminants present on the oxide surface were removed by a short (a few minutes), gentle sputter-cleaning treatment with low-energy (1 kV) Ar^+ ions. After this sputter-cleaning treatment, no surface contaminants were detected in the XPS spectra recorded over a binding energy (BE) range of 0 to 1400 eV (see below for instrumental details).

AR-XPS analysis of the specimen was performed with a Thermo VG Thetaprobe system operating in the so-called parallel data acquisition mode (see Sec. 2.1) using monochromatic incident Al Kα radiation ($h\nu$=1486.68 eV; spot size 400 μm). The emitted electrons were detected simultaneously over the angular range (with respect to the surface normal) of 23 to 83° in eight ranges of 7.5° each. The energy scale of the concentric hemispherical analyzer (CHA) was calibrated with high-purity, sputter-cleaned, reference samples of Au, Ag and Cu, such that the corresponding Au $4f_{7/2}$, Ag $3d_{5/2}$ and Cu $2p_{3/2}$ main peaks were positioned at the recommended BE values of 83.98 eV, 368.26 eV and 932.67 eV, respectively [41].

The survey spectra were recorded in the BE range of 0 to 1400 eV at a constant pass energy of 100 eV and step size of 0.1 eV. The angle-resolved spectra of Al 2p and O 1s photoelectron lines were measured in the BE range of 65 to 80 eV and 525 to 540 eV respectively, with a pass energy of 100 eV and a step size of 0.1 eV.

Charge compensation of the insulating α-Al_2O_3 specimen during the XPS analysis was achieved by irradiation of the sample surface with a diffuse beam of low energy electrons (kinetic energy of 3 eV; emission current ~35 μA) using a flood gun equipped with a LaB_6 cathode. The flood gun was operated at the lowest possible temperature (~1200K) to minimize the thermal energy spread within the incident electron beam. Optimum charge compensation was achieved by tuning the flood gun settings so as to obtain the most symmetrical and narrow-shaped oxidic Al 2*p* main peak possible from the insulating α-Al_2O_3 specimen.

The averaged value (and corresponding standard deviation for the AR-spectra recorded at the various emission angles; see above) for the BE position and Full Width at Half Maximum (FWHM) of the oxidic Al 2p main peaks of the α-Al_2O_3 reference correspond to 70.52(±0.05) eV and 1.86(±0.05) eV, respectively. The corresponding values for the BE position and Full Width at Half Maximum (FWHM) of the O 1s main peak of the α-Al_2O_3 reference equal 527.27(±0.04) eV and 2.16(±0.12) eV, respectively. This results in an average value (and standard deviation) for the Al-O binding state parameter, $E_{\text{Al-O}}$ = O 1s BE – Al 2p BE, for α-Al_2O_3 of 456.75(±0.02) eV. Note that the value of the $E_{\text{Al-O}}$ is independent upon the incident photon energy, reference level and charging effects (cf. Ref. [22]). The value of $E_{\text{Al-O}}$ = 456.75(±0.02) eV, as obtained for α-Al_2O_3 in the present study, is in excellent agreement with the corresponding value of 456.76 eV as reported in Ref. [42].

The total primary zero-loss (PZL) intensities (cf. Ref. [29]) of the oxidic Al 2p and O 1s main peaks as a function of the detection angle α (see Sec. 2.3) were resolved from the corresponding AR-XPS spectra recorded from the α-Al_2O_3 reference as follows. First, all measured Al 2p and O 1s spectra were corrected for the electron kinetic energy dependent transmission of the hemispherical analyzer of the spectrometer by adopting the corresponding correction factor as provided by the manufacturer (see above). Next, the relatively small background of inelastically scattered electrons in the BE region of the Al 2p and O 1s main peak was removed by subtraction of a Shirley-type background in the BE range of the main peak from 69 to 79 eV and from 525 to 538 eV, respectively. The total oxidic Al 2*p* and O 1*s* PZL intensities were taken equal to the integrated area under the corresponding, background corrected main peaks.

2.4 Results and discussion

The O 1s-to-Al 2p relative sensitivity factor (RSF), $S_{\mathrm{O\,1}s/\mathrm{Al\,2}p}$, for the α-Al_2O_3 reference is defined as (see Sec. 2.2.3)

$$S_{\mathrm{O\,1}s/\mathrm{Al\,2}p} = \frac{2}{3}\cdot\frac{I^{\infty}_{\mathrm{O\,1s}}}{I^{\infty}_{\mathrm{Al\,2}p}} = \frac{\lambda^{\mathrm{eff}}_{\mathrm{O\,1s}}}{\lambda^{\mathrm{eff}}_{\mathrm{Al\,2}p}}\cdot\frac{\sigma_{\mathrm{O\,1s}}W(\phi,\beta_{\mathrm{O\,1s}})}{\sigma_{\mathrm{Al\,2}p}W(\phi,\beta_{\mathrm{Al\,2}p})} = \frac{\lambda^{\mathrm{i}}_{\mathrm{O\,1s}}}{\lambda^{\mathrm{i}}_{\mathrm{Al\,2}p}}\cdot\frac{\sigma_{\mathrm{O\,1}s}}{\sigma_{\mathrm{Al\,2}p}}\cdot\frac{Q_{\mathrm{O\,1s}}W(\phi,\beta^{\mathrm{eff}}_{\mathrm{O\,1s}})}{Q_{\mathrm{Al\,2}p}W(\phi,\beta^{\mathrm{eff}}_{\mathrm{Al\,2}p})} \quad \textbf{(2.7)}$$

The value of $S_{\mathrm{O\,1}s/\mathrm{Al\,2}p}$, as determined from the total Al 2p and O 1s PZL intensities resolved from the measured AR-XPS spectra of the α-Al_2O_3 specimen (and adopting the known Al/O atomic ratio of $\frac{2}{3}$), is plotted as a function of the detection angle α and the angle ϕ in Fig. 2.2. Note that, since the concerned AR-XPS measurements were recorded in parallel data acquisition mode, a change in the detection angle α is accompanied by a corresponding change in the angle ϕ between the directions of the incident x-ray beam and the detected photoelectrons (see Sec. 2.1).

Evidently, the thus obtained values of $S_{\mathrm{O\,1}s/\mathrm{Al\,2}p}$ increases with increase of the interdependent angles α and ϕ. That is, the value for $S_{\mathrm{O\,1}s/\mathrm{Al\,2}p}$ is at a maximum (minimum) for the grazing (near-normal) angles of α with respect to the sample surface, corresponding to a large (small) ϕ between the directions of the incident x-ray beam and the detected photoelectrons (see Fig. 2.1). Note that, for a similar series of AR-XPS measurements performed in a conventional XPS setup (i.e. ϕ is a constant fixed at the magic angle, and the detection angle α is varied by tilting the sample), the RSF, $S_{\mathrm{O\,1}s/\mathrm{Al\,2}p}$, would be independent of the detection angle α (in the absence of elastic electron scattering and photoelectron diffraction effects within the solid; see Sec. 2.2).

As discussed in Sec. 2.2, the observed change in the RSF with the interdependent angles α and ϕ (in parallel data acquisition mode) is due to the combined effects of the anisotropies of the photoionization cross-sections and the elastic scattering of the detected photoelectrons within the solid. In this case, the relative difference between the intrinsic anisotropies of the Al 2*p* and O 1*s* photoionization cross-sections is expressed in Eq. (2.7) by the asymmetry-factor-ratio $W(\phi,\beta_{\mathrm{O\,1}s})/W(\phi,\beta_{\mathrm{Al\,2}p})$, the value of which depends only upon the angle ϕ (see Eq. (2.3a)). The relative difference in elastic (and inelastic) scattering of the detected O 1*s* and Al 2*p* photoelectrons within the solid, on the other hand, is expressed in Eq. (2.7) by the EAL-ratio $\lambda^{eff}_{\mathrm{O\,1}s}/\lambda^{eff}_{\mathrm{Al\,2}p}$, the value of which depends mainly on the detection angle α (due to the dependence of the corresponding *Q*-factors on the angle α; see Eqs. (2.4a – 2.4d)).

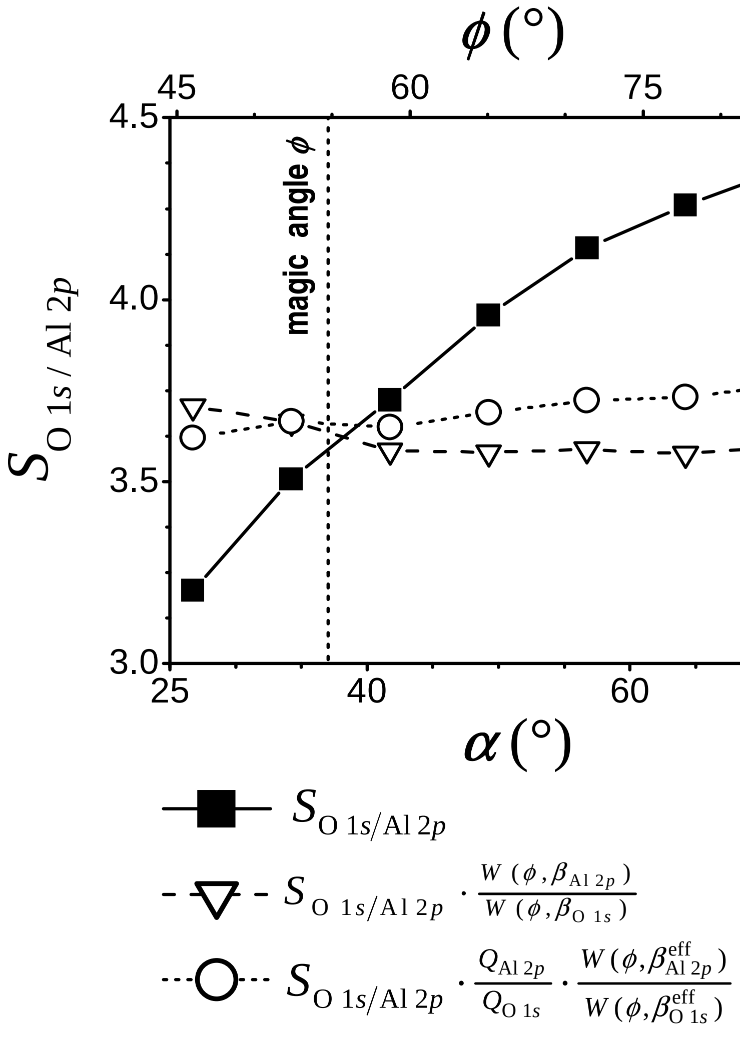

Figure 2.2. The relative sensitivity factor (RSF), $S_{\mathrm{O\,1}s/\mathrm{Al\,2}p}$, for α-Al_2O_3, versus the interdependent angles α (bottom *x*-axis) and ϕ (top *x*-axis) (see Fig. 2.1). The terms $S_{\mathrm{O\,1}s/\mathrm{Al\,2}p}\cdot W(\phi,\beta_{\mathrm{Al\,2}p})/W(\phi,\beta_{\mathrm{O\,1}s})$ and $S_{\mathrm{O\,1}s/\mathrm{Al\,2}p}\cdot Q_{\mathrm{Al\,2}p}/Q_{\mathrm{O\,1}s}\cdot W(\phi,\beta^{\mathrm{eff}}_{\mathrm{Al\,2}p})/W(\phi,\beta^{\mathrm{eff}}_{\mathrm{O\,1}s})$ are also plotted as a function of the interdependent angles α and ϕ. See text for details.

To investigate the effect of the intrinsic anisotropies of the Al 2p and O 1s photoionization cross-sections on the angular dependence of the RSF, the value of $S_{\mathrm{O\,1}s/\mathrm{Al\,2}p}$ is divided by the asymmetry-factor-ratio $W(\phi,\beta_{\mathrm{O\,1}s})/W(\phi,\beta_{\mathrm{Al\,2}p})$ (see Eq. (2.7)) and plotted as a function of the interdependent angles α and ϕ in Fig. 2.2. All data used for the calculation of the asymmetry factors $W(\phi,\beta_{\mathrm{O\,1}s})$ and $W(\phi,\beta_{\mathrm{Al\,2}p})$ (using the appropriate expressions as given in Sec. 2.2), as well as their resulting values, are reported in Tables 2.1 and 2.2, respectively. Evidently, the value of $S_{\mathrm{O\,1}s/\mathrm{Al\,2}p}\cdot W(\phi,\beta_{\mathrm{Al\,2}p})/W(\phi,\beta_{\mathrm{O\,1}s})$ is nearly constant over the angular detection range of 40° to 80° (corresponding to a ϕ -range of 56° to 91°). This implies that the *variation* of the RSF over this angular range is, to a first approximation, solely determined by the relative changes of the intrinsic anisotropies of the Al 2p and O 1s photoionization cross-sections with ϕ.

Nevertheless, the value of $S_{\mathrm{O\,1}s/\mathrm{Al\,2}p}\cdot W(\phi,\beta_{\mathrm{Al\,2}p})/W(\phi,\beta_{\mathrm{O\,1}s})$ shows a small, but distinct, increase with decreasing angles for the near-normal detection range (i.e. within the ranges 25° < α < 40° and 45°< ϕ < 56°; see Fig. 2.2), indicating that an additional factor is responsible for the variation of $S_{\mathrm{O\,1}s/\mathrm{Al\,2}p}$ within this angular range. To investigate whether the variation of the RSF within this near-normal detection range is to some extent caused by differences in elastic scattering of the detected Al 2p and O 1s photoelectrons, the term $S_{\mathrm{O\,1}s/\mathrm{Al\,2}p}\cdot Q_{\mathrm{Al\,2}p}/Q_{\mathrm{O\,1}s}\cdot W(\phi,\beta^{\mathrm{eff}}_{\mathrm{Al\,2}p})/W(\phi,\beta^{\mathrm{eff}}_{\mathrm{O\,1}s})$ (see Eq. (2.7)) is plotted as a function of the angles α and ϕ in Fig. 2.2. All data used for the calculation of the effective asymmetry factors and Q factors (using the appropriate expressions as given in Sec. 2.2), as well as their resulting values, are reported in Tables 2.1 and 2.2, respectively. Indeed, the value of $S_{\mathrm{O\,1}s/\mathrm{Al\,2}p}\cdot Q_{\mathrm{Al\,2}p}/Q_{\mathrm{O\,1}s}\cdot W(\phi,\beta^{\mathrm{eff}}_{\mathrm{Al\,2}p})/W(\phi,\beta^{\mathrm{eff}}_{\mathrm{O\,1}s})$, which incorporates the combined effects of the anisotropies of the photoionization cross-sections and elastic scattering, is approximately constant over the near-normal detection range (i.e. 25° < α < 40° and 45°< ϕ < 56°; see Fig. 2.2). This confirms that the *variation* of the RSF over this angular range is indeed, to some extent, also determined by differences in elastic scattering of the Al 2p and O 1s photoelectrons.

It should be noted that the value of the RSF in the grazing detection angle range of, say, α > 70°, will be affected by small deviations from stoichiometry at the α-Al_2O_3 surface (due to e.g. preferential sputtering effects upon cleaning; see Sec. 2.3). On the other hand, even for 10% deviation in the oxide stoichiometry, the changes in the corresponding asymmetry- and Q-factors are negligible.

As discussed in Sec. 2.2.2, the effect of elastic scattering of the detected photoelectrons on the observed PZL photoelectron intensity is two-fold: (*i*) it affects the intrinsic anisotropy of the photoionization cross-section, as described by the reduction of the parameter β_{AX_n} to an effective asymmetry parameter $\beta^{\mathrm{eff}}_{AX_n}$, and (*ii*) it affects the overall escape probability of the emitted photoelectrons, as described by the weak correction factor Q_{AX_n}. The separate contributions of these two elastic-scattering parameters to the observed variation of the RSF, $S_{\mathrm{O\,1}s/\mathrm{Al\,2}p}$, with α and ϕ are expressed by the corresponding values of

Table 2.1. Physical constants used for the calculations of the effective asymmetry parameters (β^{eff}), the *Q*-factors (*Q*), and the effective attenuation lengths (λ^{eff}).

Constant		Value	Units	Reference
Density of α-Al_2O_3		3.99×10^{6}	g/m^3	
Molecular mass of α-Al_2O_3		101.961	g/mol	
Band gap of α-Al_2O_3		8.7	eV	[43]
Asymmetry factor:	$\beta_{\mathrm{Al\,2}p}$	0.93		[33]
	$\beta_{\mathrm{O\,1}s}$	2.00		
Kinetic energy:	Al 2p photoelectrons	1416.16	eV	
	O 1s photoelectrons	954.41	eV	
Inelastic Mean Free Path:	$\lambda^{\mathrm{i}}_{\mathrm{Al\,2}p}$	3.257	nm	[44]
	$\lambda^{\mathrm{i}}_{\mathrm{O\,1}s}$	2.416	nm	
Transport cross-sections:	$\sigma_{\mathrm{tr,\,Al}}$(KE = 1416.16 eV)	6.93×10^{-22}	m^2	[45]
	$\sigma_{\mathrm{tr,\,O}}$(KE = 1416.16 eV)	3.25×10^{-22}	m^2	
	$\sigma_{\mathrm{tr,\,Al}}$(KE = 954.41 eV)	12.49×10^{-22}	m^2	
	$\sigma_{\mathrm{tr,\,O}}$(KE = 954.41 eV)	6.13×10^{-22}	m^2	
Transport Mean Free Path:	$\lambda^{\mathrm{tr}}_{\mathrm{Al\,2}p}$	17.98	nm	
	$\lambda^{\mathrm{tr}}_{\mathrm{O\,1}s}$	9.78	nm	
Single scattering albedo:	$\omega_{\mathrm{Al\,2}p}$	0.153		
	$\omega_{\mathrm{O\,1}s}$	0.198		

$Q_{\mathrm{Al\,2}p}/Q_{\mathrm{O\,1}s}$ and $W(\phi,\beta^{\mathrm{eff}}_{\mathrm{Al\,2}p})/W(\phi,\beta^{\mathrm{eff}}_{\mathrm{O\,1}s})\cdot W(\phi,\beta_{\mathrm{O\,1}s})/W(\phi,\beta_{\mathrm{Al\,2}p})$. The values for these two terms are plotted as a function of the angles α and ϕ in Fig. 2.3. Clearly, their contributions to the resulting value of $S_{\mathrm{O\,1}s/\mathrm{Al\,2}p}$ are very small, i.e. up to 3%, with the effect of elastic scattering on the relative difference in anisotropies of the photoionization cross-sections (i.e. the term $W(\phi,\beta^{\mathrm{eff}}_{\mathrm{Al\,2}p})/W(\phi,\beta^{\mathrm{eff}}_{\mathrm{O\,1}s})\cdot W(\phi,\beta_{\mathrm{O\,1}s})/W(\phi,\beta_{\mathrm{Al\,2}p})$) being more pronounced. Moreover, it can be concluded from Fig. 2.3 that the relative differences between the Al 2p and O 1s elastic scattering parameters (i.e. β^{eff} and Q), cancel out to some extent in the near-normal detection range (i.e. 25° < α < 40° and 45°< ϕ < 56°). Consequently, the effect of elastic scattering on the *absolute* value of the relative sensitivity factor is more pronounced for detection angles α > 40°.

Table 2.2. Calculated values of the Chandrasekhar functions ($H(x,\ \omega)$; see Ref. [39]), the effective asymmetry parameters (β^{eff}), the Q-factors (Q), and the effective attenuation lengths (λ^{eff}), as a function of the interdependent angles α and ϕ (see Fig. 2.1). The values are calculated from the appropriate expressions as given in Sec. 2.2, and employing the data as listed in Table 2.1. See Secs. 2.2 and 2.4 for details.

α (°)	ϕ (°)	$H(\cos\alpha, \omega_{\mathrm{Al\,2}p})$	$H(\cos\alpha, \omega_{\mathrm{O\,1}s})$	$\beta^{\mathrm{eff}}_{\mathrm{Al\,2}p}$	$\beta^{\mathrm{eff}}_{\mathrm{O\,1}s}$	$Q_{\mathrm{Al\,2}p}$	$Q_{\mathrm{O\,1}s}$	$\lambda^{\mathrm{eff}}_{\mathrm{Al\,2}p}$ (nm)	$\lambda^{\mathrm{eff}}_{\mathrm{O\,1}s}$ (nm)
26.75	45.86	1.0564	1.0751	0.8097	1.6639	0.9725	0.9639	3.2154	2.4438
34.25	51.71	1.0550	1.0732	0.8110	1.6682	0.9709	0.9615	3.1767	2.3544
41.75	57.84	1.0532	1.0706	0.8126	1.6736	0.9689	0.9584	3.1418	2.2889
49.25	64.17	1.0507	1.0673	0.8148	1.6803	0.9663	0.9546	3.1114	2.2408
56.75	70.62	1.0474	1.0629	0.8176	1.6886	0.9630	0.9498	3.0851	2.2050
64.25	77.16	1.0430	1.0569	0.8213	1.6992	0.9588	0.9439	3.0618	2.1779
71.75	83.75	1.0370	1.0488	0.8262	1.7131	0.9530	0.9362	3.0401	2.1563
79.25	90.37	1.0281	1.0370	0.8333	1.7326	0.9449	0.9257	3.0168	2.1367

It can be concluded that, for the recording of AR-XPS spectra in parallel data acquisition mode, the observed variation of the RSF with the interdependent angles α and ϕ can be fully ascribed to the combined effects of the anisotropies of the photoionization cross-sections and the elastic scattering of the detected photoelectrons within the solid. For the quantitative analysis of AR-XPS spectra recorded in parallel data acquisition mode, it is therefore essential to apply the correct RSFs for each angular range concerned.

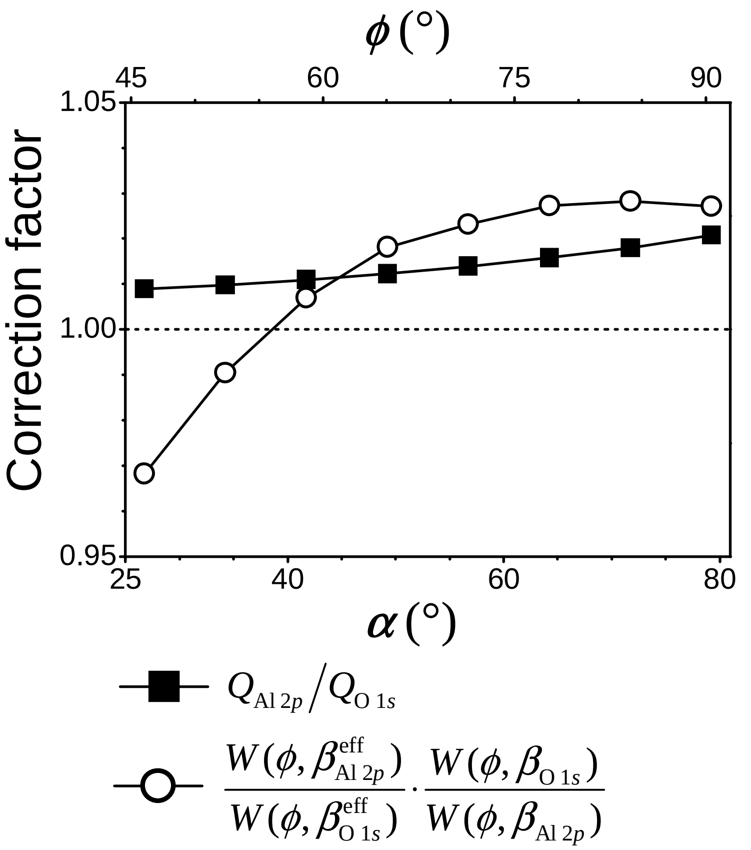

Figure 2.3. Calculated values of $W(\phi,\beta^{\mathrm{eff}}_{\mathrm{Al}\,2p})/W(\phi,\beta^{\mathrm{eff}}_{\mathrm{O}\,1s})\cdot W(\phi,\beta_{\mathrm{O}\,1s})/W(\phi,\beta_{\mathrm{Al}\,2p})$ and $Q_{\mathrm{O}\,1s}/Q_{\mathrm{Al}\,2p}$ for α-Al_2O_3, as a function of the interdependent angles α (bottom *x*-axis) and ϕ (top *x*-axis) (see Fig. 2.1). The term $W(\phi,\beta^{\mathrm{eff}}_{\mathrm{Al}\,2p})/W(\phi,\beta^{\mathrm{eff}}_{\mathrm{O}\,1s})\cdot W(\phi,\beta_{\mathrm{O}\,1s})/W(\phi,\beta_{\mathrm{Al}\,2p})$ is a measure of the effect of elastic scattering on the anisotropy of the intrinsic photoionization cross-section, whereas the term $Q_{\mathrm{O}\,1s}/Q_{\mathrm{Al}\,2p}$ describes the effect of elastic scattering on the overall escape probability of the detected photoelectrons. See text for details.

As an example, for the errors introduced in quantification when these effects are ignored, the determination of the composition of the measured α–Al_2O_3 reference (with a known O/Al-ratio of 3/2) is considered (see Fig. 2.4). The composition of the measured oxide reference, expressed as the oxygen to metal ratio, is calculated from (cf. Eq. (2.7))

$$\frac{C_{\mathrm{O}}}{C_{\mathrm{Al}}}=\frac{I^{\infty}_{\mathrm{O}\,1s}(\alpha,\phi)}{I^{\infty}_{\mathrm{Al}\,2p}(\alpha,\phi)}\cdot\frac{1}{S_{\mathrm{O}\,1s/\mathrm{Al}\,2p}(\alpha,\phi)} \tag{2.8}$$

where $I^{\infty}_{\mathrm{O}\,1s}(\alpha,\phi)$, $I^{\infty}_{\mathrm{Al}\,2p}(\alpha,\phi)$ and $S_{\mathrm{O}\,1s/\mathrm{Al}\,2p}(\alpha,\phi)$ denote the resolved O 1*s* PZL intensity, the resolved Al 2*p* PZL intensity and the corresponding experimentally determined RSF for a

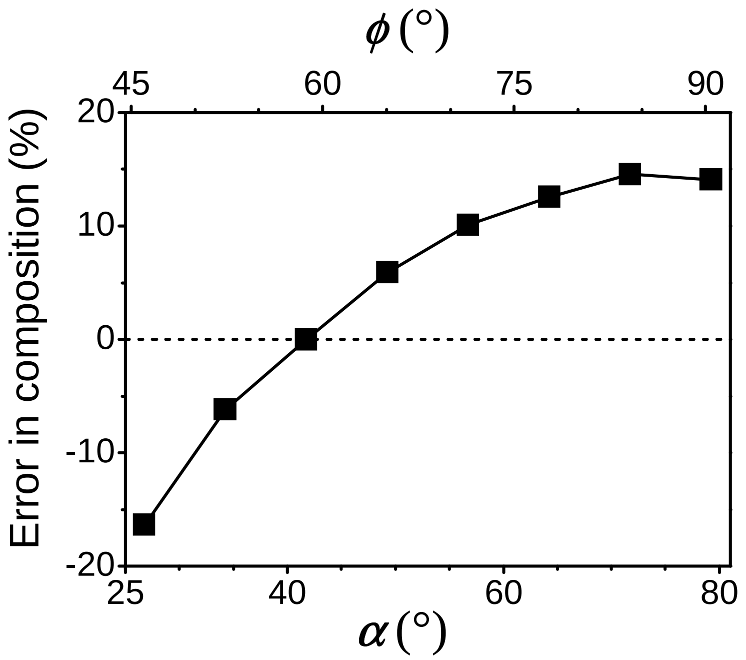

Figure 2.4. Error in the calculated composition (i.e. O/Al-ratio) of α-Al_2O_3 as a function of the interdependent angles α (bottom *x*-axis) and ϕ (top *x*-axis) introduced when adopting a single value for the relative sensitivity factor, $S_{\mathrm{O\ 1s/Al\ 2}p}(\alpha = 41.8°, \phi = 57.8°)$ (i.e. close to the magic angle of ϕ = 54.74°; see Sec. 2.2). The straight line along the ordinate indicates the correct O/Al-ratio for α-Al_2O_3 of 3/2, as would be obtained when accounting for the effects of the anisotropy of the photoionization cross-sections and the elastic scattering of the detected photoelectrons within the solid. See text for details.

given set of angles α and ϕ, respectively. Figure 2.4 shows the percentage of error introduced in the calculated values of the composition versus the angles α and ϕ, when not taking into account the effects of the anisotropy of photoionization cross-section and elastic scattering, i.e. when adopting a single value for the RSF, as taken equal to the experimentally determined sensitivity factor $S_{\mathrm{O\ 1s/Al\ 2}p}(\alpha = 41.8°, \phi = 57.8°)$ (i.e. close to the magic angle of ϕ = 54.74°). Clearly, when ignoring the effects of anisotropy of photoionization cross-section and elastic scattering, the magnitude of error induced in the compositional analysis of the AR-XPS spectra recorded from binary solids in parallel data acquisition mode can be as high as 16%. Here, it should be noted that the contribution of elastic scattering to the introduced error is relatively small. By adopting values for the relative sensitivity factors as a function of the angles α and ϕ, as determined experimentally from a reference solid of known composition, cumbersome corrections for the effects of the anisotropies of the photoionization cross-sections and elastic scattering can be avoided, e.g. for the quantitative analysis of solids and thin film structures of unknown composition and/or thickness.

2.5 Conclusions

For the quantitative analysis of angle-resolved XPS spectra recorded in parallel data acquisition mode, it is essential to account for the anisotropies of the photoionization cross-sections of the concerned elements in the solid due to the variation of the angle ϕ between the incident X-rays and the detected photoelectrons. The effect of elastic scattering on the quantitative analysis of the AR-XPS, as described by the effective asymmetry parameter β^{eff} and the correction factor Q, is relatively small (the effect being most pronounced in the grazing incidence angle range).

By adopting values for the relative sensitivity factors of the concerned elements in the solids as a function of the interdependent angles α and ϕ, cumbersome corrections for the effects of the anisotropies of the photoionization cross-sections and elastic scattering can be avoided, for example, in the quantitative analysis of solids and thin film structures of unknown thickness and/or composition. Values for the relative sensitivity factors as a function of the angles α and ϕ, which incorporate the combined effects of the anisotropies of the photoionization cross-sections and elastic scattering, can easily be determined from AR-XPS measurements of reference solids of known composition.

Acknowledgement

The authors are indebted to Prof. Dr. Ir. E. J. Mittemeijer and Prof. Dr. S. Hofmann for critical reading of the manuscript.

Chapter 3

Quantitative analysis of multi-element oxide thin films by angle-resolved XPS

Application to ultra-thin oxide films on MgAl substrates

L.P.H Jeurgens, M.S. Vinodh, E.J. Mittemeijer

Abstract

An original procedure has been developed for the quantitative analysis and microstructural interpretation of angle-resolved X-ray photoelectron spectra (AR-XPS) of very thin (< 6 nm), multi-element oxide films as grown on metallic binary alloy substrates by e.g. thermal or plasma oxidation. To this end, first an approach has been given to retrieve the different metallic, oxidic and oxygen primary zero-loss (PZL) intensities from the measured AR-XPS spectra of the bare and oxidized alloy. The principal equations for the determination of the oxide-film thickness, composition and constitution from the thus resolved PZL intensities have been presented. On this basis, various corresponding calculation routes have been distinguished. The procedure has been applied to the case of very thin (< 6 nm), mixed (Mg,Al)-oxide films on bare Mg-based MgAl substrates as grown by dry, thermal oxidation at room temperature. The results obtained on the thickness, composition, defect structure and constitution of the oxide-film have been discussed as function of the bulk Al alloying content and the applied partial oxygen pressure.

3.1 Introduction

The development of reliable and accurate methods for the determination of the microstructure of very thin oxide films (< 6 nm) by application of a surface-sensitive technique, such as X-ray photoelectron spectroscopy (XPS), is of great interest in numerous application areas such as microelectronics, catalysis and surface coatings (cf. Refs. [19, 46]). At present, such procedures exist for the quantitative analysis of XPS spectra recorded from *single-element* oxide (e.g. pure M_xO_y) films grown on their parent metal substrates [20, 29, 47, 48]. Recording a series of XPS spectra from the metal substrate after various oxidations allows an accurate determination of the oxide-film thickness [14, 19, 20] and composition [14, 20, 21], as well as the chemical state of the constituent ions in the oxide film [22, 23], as a function of the oxidation conditions (i.e. time, temperature, partial oxygen pressure, substrate orientation). Further, if a series of XPS spectra is recorded from the oxidized metal at various photoelectron detection angles with respect to the specimen surface, as in angle-resolved XPS (AR-XPS) [21, 49], detailed knowledge on the oxide-film morphology [21, 24] and constitution (expressed as the relative depth distribution of different chemical species within the developing oxide film) [14, 20, 21, 24] can be obtained.

However, for the analysis of *multiple-element* oxide films, composed of e.g. a solid solution of two oxide phases, a spinel oxide phase or a doped oxide phase, up to date no well-defined procedures have been developed to determine the thickness, composition and constitution of such thin films by quantitative (angle-resolved) XPS, which can be ascribed to the increasing complexity in the procedures for spectra evaluation and subsequent quantification. For example, for the XPS spectra recorded from an oxide film grown on a binary alloy by thermal or plasma oxidation, at least five different photoelectron signals should be considered in the quantification (i.e. from the metallic and oxidic intensity for each alloy constituent plus the oxygen intensity; see this work and Ref. [50]). Moreover, for the determination of the oxide-film thickness and composition from these photoelectron intensities (i.e. from the total intrinsic intensities; see Ref. [29]), pre-existing knowledge and/or reasonable estimates of e.g. the intrinsic plasmon excitation probabilities [29, 51-53] in the alloy, the oxide-film density and/or the effective attenuation lengths [36] of the corresponding detected photoelectrons in the oxide film are required.

In this contribution, a detailed procedure is presented for the evaluation and subsequent quantification of a series of AR-XPS spectra recorded from bare (Figs. 3.1 and 3.2) and oxidized (Fig. 3.3) binary alloys. The method is applied to a series of measured AR-XPS spectra of ultra-thin (< 2 nm), mixed (Mg,Al)-oxide films on bare Mg-based MgAl substrates as grown by dry, thermal oxidation at room temperature at a partial oxygen pressure (pO_2) range of 10^{-7}-10^{-4} Pa (and for bulk Al contents of 2.63 and 7.31 at.%). The treatment starts with the determination of the total metallic Mg 2p and Al 2p, oxidic Mg 2p and Al 2p and oxygen O 1s primary zero loss (PZL) intensities from the measured XPS spectra of the bare and oxidized alloy. Then, the derivation of the principal equations used and the calculation schemes for the determination of the oxide-film thickness, composition and constitution from the thus resolved PZL intensities are given. Finally, the results thus obtained for the oxidation of the investigated MgAl alloys for the oxide-film thickness, composition, defect structure and constitution are discussed as a function of the bulk Al alloying content and the applied pO_2.

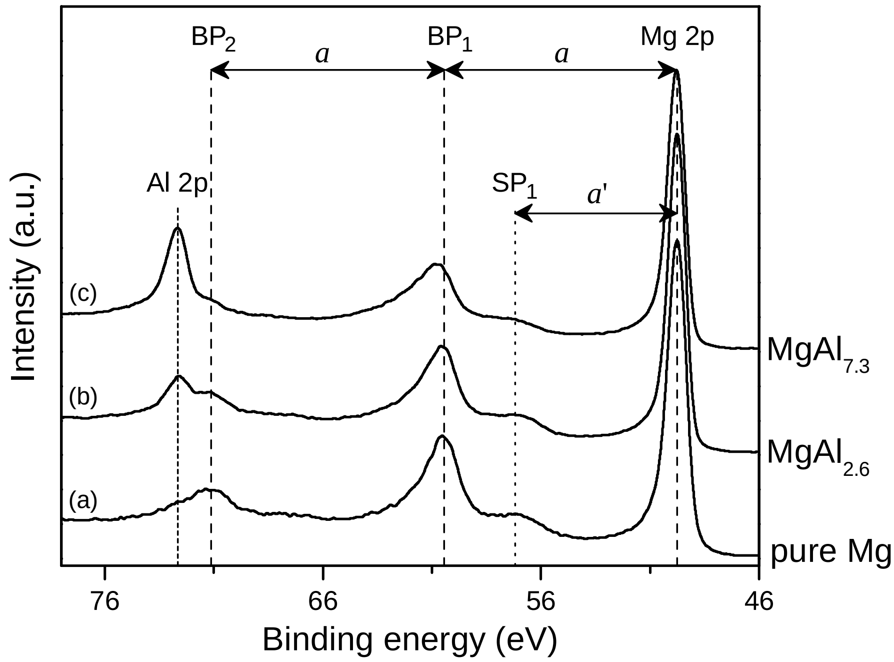

Figure 3.1. As-measured Mg 2p – Al 2p AR-XPS spectra recorded from bare substrates of (a) pure Mg metal, (b) a Mg-Al alloy containing 2.6 at.% Al, and (c) a Mg-Al alloy containing 7.3 at.% Al. The metallic Mg 2p and Al 2p main peaks, and the first surface plasmon peak (SP_1), the first (BP_1) and second (BP_2) bulk plasmon peaks, all associated with the Mg 2p main peak, have been indicated. The SP_1, BP_1 and BP_2 plasmon peaks are positioned at energies $a' = E_0 - \hbar\omega_{sp}$, $a = E_0 - \hbar\omega_{bp}$ and $2a = E_0 - 2\hbar\omega_{bp}$ at the higher BE side of the asymmetric core-level, ground-state metallic main peak positioned at a kinetic energy E_0, respectively ($\hbar\omega_{sp}$ and $\hbar\omega_{bp}$ denote the plasmon energies for surface and bulk plasmon excitations in the alloy, respectively). The spectra were recorded and subsequently averaged over the (entire) angular detection range from (α, ϕ) = (23°, 43°) to (α, ϕ) = (83°, 94°) (Sec. 3.2.2).

3.2 Experimental

3.2.1 Specimen preparation and oxidation

Two single-phase MgAl alloys with Al contents of 2.63 and 7.31 at.% were prepared by casting a liquid, prepared of appropriate weight fractions of high purity Mg (< 99.999 wt.%) and Al (<99.99 wt.%)) in a vacuum–melting furnace, and subsequent annealing and quenching (for details, see Ref. [50]). To homogenize the grain size distribution, as well as to decrease the average grain size, the rods were hammered down by 1 mm (from φ = 11 mm to φ = 10 mm) and subsequently annealed for 1 h at 693 K in a conventional furnace (and then again quenched). Next, disc-shaped specimens (φ = 10 mm and thickness 1 mm) were prepared by grinding and subsequent polishing down to 0.25 μm [50]. As confirmed by X-ray diffraction (XRD) analysis, all specimens are single-phased (i.e. an Mg-Al solid solution) and, as shown by light optical microscopic analysis, possess an average grain size within the range of 50 – 100 μm.

The specimen was introduced in the UHV chamber for angle-resolved XPS analysis (AR-XPS; base pressure < 5×10^{-8} Pa) directly coupled to the UHV reaction chamber for controlled oxidation (RC; base pressure < 3×10^{-8} Pa). Prior to each oxidation, the (native) oxide and other contaminants (possibly some adventitious carbon) on the specimen surface were removed by sputter-cleaning (SC) with a focused 1 kV Ar^+ beam (rastering the entire specimen surface) until no other elements than Mg and Al were detected in a measured XPS survey spectra recorded over the binding energy (BE) range from 0 to 1400 eV (for instrumental details, Sec. 3.2.2). The MgAl specimens, as obtained after the aforementioned SC treatment are further designated as *bare* substrates.

Next, an oxide film was grown on the bare substrate in the RC by exposure to pure oxygen gas (99.997 vol %) for 1 h at 304 K (i.e. room temperature) at a pO_2 range of 1×10^{-6} - 1×10^{-4} Pa. The oxygen gas was introduced in the RC by a needle valve and adjusted by hand to the required pO_2 (as measured with a quadrupole mass spectrometer) within about 30 s.

3.2.2 AR-XPS analysis

AR-XPS analysis of the specimen surface before and after oxidation was performed with a Thermo VG Thetaprobe system employing monochromatic Al Kα radiation ($h\nu$ = 1486.68 eV; spot size 400 μm). The energy scale of the analyzer was calibrated as described in Ref. [49]. XPS survey spectra, covering a binding energy (BE) range of 0 eV to 1200 eV, were recorded with a step size of 0.2 eV at constant pass energy of 200 eV. For the bare and oxidized substrate, detailed AR-XPS spectra of the combined Mg 2p and Al 2p regions (BE range 40 - 85 eV) were recorded; the O 1s region (BE range 525 - 540 eV) was measured only for the oxidized substrate. All spectra were recorded with a step size of 0.1 eV at a constant pass energy of 100 eV. The AR-XPS measurements were performed in so-called parallel data acquisition mode by detecting the photoelectrons simultaneously over the angular detection range of (α, ϕ) = (23°, 43°) to (α, ϕ) = (83°, 94°) in eight ranges of 7.5° each (for details, see Ref. [49]). Here, the interdependent angles α and ϕ are defined as the angle between the directions of the detected photoelectrons and the specimen surface normal and the angle between the directions of the detected photoelectrons and the incident photon beam, respectively. To avoid possible grain orientation effects for the weakly textured specimens (as verified by XRD), the AR-XPS spectra of the bare and oxidized substrate were measured at 9 and 16 defined points (spot size 400 μm), respectively, equally distributed over an entire analysis area of 3×3 mm^2 on the measured specimen and then averaged for each angular range of photoelectron detection (see above and Sec. 3.3). To avoid any contamination or pre-oxidation of the bare substrate during measurement, the AR-XPS measurements of the bare substrate were performed in a so-called iterative mode, consisting of successive cycles of sputter cleaning (for 90 s with either 1 or 3 kV Ar^+ ions) and subsequent measurement at each defined position.

3.2.3 AR-XPS spectra reconstruction

First, all measured AR-XPS spectra were averaged over all measured positions of the specimen surface for each angular range of photoelectron detection concerned (Sec. 3.2). Next, the thus obtained spectra were corrected for dependence of the transmission of the spectrometer analyzer on the electron kinetic energy by adopting the corresponding correction factor as provided by the manufacturer (Sec. 3.2.2).[1] Then, for each detection angle set employed (Sec. 3.2.2), the Mg 2p and Al 2p PZL intensities of the asymmetric metallic main peaks and the symmetric oxidic main peaks [29, 48, 52-54] were determined from the thus corrected AR-XPS spectra (further designated as '*as-measured*' spectra; see Fig. 3.2a) of both the bare and the oxidized substrate as follows.

[1] Note that, only for the XPS spectra as presented in Fig. 3.1, the thus obtained AR-XPS spectra were subsequently (i.e. after averaging over all measured positions and correcting for the analyzer transmission function) summed over the entire detection angle range employed.

3.3 AR-XPS spectra of the bare alloy substrate

3.3.1 Resolving the metallic Mg 2p main peak

For the case of the *bare* MgAl substrate, the PZL intensity of the metallic Mg 2p main peak (i.e. including the tail towards higher BE values, but excluding the intrinsic plasmon PZL intensity, see Refs. [29, 51-53]) was determined from the corresponding, as-measured Mg 2p XPS spectra (and for each detection angle set; see Sec. 3.2) as follows (see Fig. 3.2b).

(i) First, the lower BE side of the metallic main peak was set to zero (background) intensity by subtraction of a constant background, the value of which was taken equal to the averaged minimum intensity at the lower BE side of the Mg 2p main peak.

(ii) Next, a background of inelastically scattered photoelectrons was subtracted from the thus obtained spectrum over the BE range from 46.5 eV to 53 eV, using Tougaard's formalism [51] for a bare homogeneous substrate and adopting a three-parameter universal cross section for inelastic-electron scattering [55] with B = 13 eV^2, C = 118.6 eV^2 and D = 3.5 eV^2 (as determined in the present study) (see also Ref. [29]).

(iii) Subsequently, the shape of the Mg 2p metallic main peak was determined by linear least squares (LLS) fitting of the intrinsic part of the metallic main peak, as obtained after (*ii*), with the sum of two Doniach-Sunjic (DS) line shape functions [54] of identical shape (representing the Mg $2p^3/_2$-$2p^1/_2$ spin-orbit doublet) after their convolution with a Gauss function to account for instrumental broadening.[2] LLS fitting was performed simultaneously for the entire set of AR-XPS spectra recorded at different detection angle sets from a single bare alloy substrate (over the BE range from 46.5 to 53 eV and using the Nelder-Mead simplex search method as implemented in Matlab) [56]. The position, height, full-width-at-half-maximum (FWHM) and singularity index (γ) of the Mg $2p^3/_2$ DS line shape function, as well as the instrumental broadening factor (dE) were adopted as fit parameters, while, allowing only the position and height of the Mg $2p^3/_2$ DS line shape to vary with

---

[2] A DS line shape function is defined by its height, position, full-width-at-half-maximum (FWHM) and the singularity index, γ, which determines the extent of the asymmetric tail towards higher BEs [54]. Now, to describe the Mg $2p^3/_2$-$2p^1/_2$ spin-orbit doublet, two DS line shape functions of identical shape (i.e. the same FWHM and singularity index) and a known spin-orbit splitting and relative intensity ratio of 0.265 eV and 0.5 were used, respectively (cf. Ref. 52). The thus constructed Mg 2p main peak is then convolved with a Gauss function of unit area and FWHM equal to dE, to account for instrumental broadening.

detection angle. To minimize the total number of fit parameters during the fitting, only those fit parameters which show a clear dependence on the detection angle (as indicated from a separate parameter study for each fit procedure employed for spectral evaluation; see also Secs. 3.1.2 and 3.2) were allowed to vary with detection angle. For the remaining fit parameters a single value was fitted for all detection angles employed.

(iv) Finally, the PZL intensity of the metallic Mg 2p main peak in the spectrum of the bare alloy substrate was obtained (for each detection angle) by integrating the intrinsic metallic Mg 2p main peak, as obtained after (*ii*), and adding to this intensity the integrated intensity of the excluded intrinsic tail-part of the metallic main peak extending below the plasmon structure from 53 eV towards higher BE values (Fig. 3.2b). The excluded tail-part is constructed by extrapolation of the optimized DS line shape function of the metallic Mg 2p main peak, as determined in step (*iii*), over the BE range from 53 eV to 63 eV (Fig. 3.2b).

3.3.2 Resolving the metallic Al 2p main peak

As follows from Figs. 3.1 and 3.2a, the Al 2p metallic main peak in the XPS spectra of the bare Mg-Al substrate overlaps strongly with the second bulk plasmon peak of the metallic Mg 2p main peak (further designated as BP_2 peak). The *extrinsic* parts of the surface and bulk plasmon structures belong to the background of inelastically scattered electrons of the Mg 2p main peak (cf. Refs. [29, 51-53]). This implies that their contributions to the measured Mg 2p –Al 2p AR-XPS spectra can be calculated and subtracted from the as-measured spectra [51], provided that the differential cross sections for *extrinsic* surface and bulk plasmon excitations are known for the alloy composition under investigation [51-53, 55]. However, detailed knowledge of these cross sections for binary alloys does not exist, because both the amplitude and frequency of the collective oscillations of the conduction electrons in the alloy depend on the alloying content, as well as on the detection angle set (α, ϕ) employed in the angle-resolved XPS investigation (see Sec. 3.3 and Fig. 3.1). Moreover, after correct subtraction of the extrinsic bulk plasmon structure, the *intrinsic* part of the bulk plasmon structure still remains [29, 48, 51-53].

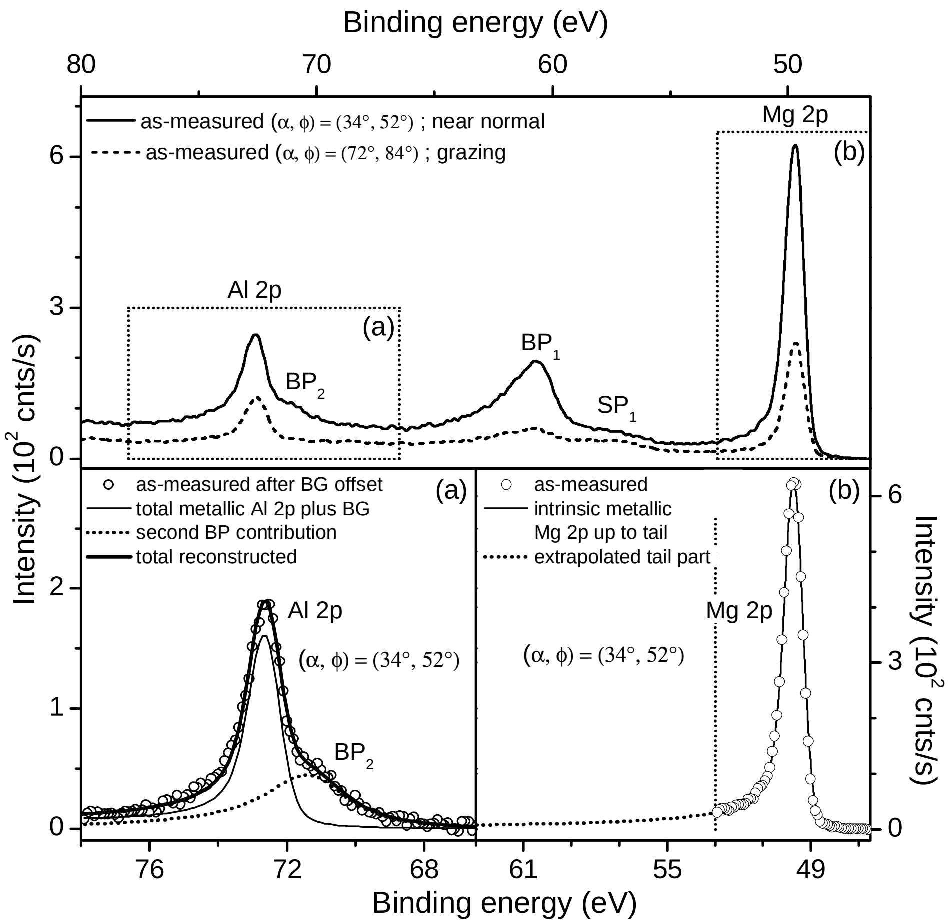

Figure 3.2. As-measured Mg 2p – Al 2p AR-XPS spectra recorded from a bare Mg – 7.31 at.% Al substrate recorded at near-normal and grazing detection angle sets of (α, ϕ) = (34°, 52°) and (α, ϕ) = (72°, 84°), respectively. (**a**) Reconstruction of the total metallic Al 2p main peak (plus its inelastic background, BG) and the second bulk plasmon peak of the Mg 2p main peak (BP_2) for the as-measured Al 2p spectra of the bare Mg – 7.31 at.% Al alloy substrate recorded at (α, ϕ) = (34°, 52°) after zero-background offset (for details, see Sec. 3.3.2). (**b**) Reconstruction of the primary zero-loss (i.e. intrinsic) metallic Mg 2p main peak for the as-measured Mg 2p spectra of the bare Mg – 7.31 at.% Al alloy substrate recorded at (α, ϕ) = (34°, 52°) (for details, see Sec. 3.3.1).

Therefore, a different approach has been proposed and used here to separate the *total* bulk plasmon peak (i.e. the sum of its intrinsic and extrinsic parts) from a core-level main peak in a measured AR-XPS spectrum of a bare or oxidized ‘free-electron’-like metal or alloy. The approach (as described in detail below) is based on the existing knowledge that the total differential cross section for extrinsic and intrinsic bulk plasmon excitations can be approximated by a simple Lorentz function [52, 53, 55]. This implies that the *shape* (but not the position or intensity) of the bulk plasmon peaks associated with the metallic Mg 2p main peak in a measured XPS spectrum of a MgAl alloy can be described by the *shape* of the intrinsic Mg 2p metallic main peak after its convolution with a Lorentz function of given width and unit height [52, 53]. On this basis, for the case of the *bare* MgAl substrate, the spectral contributions due to the metallic Al 2p main peak and the BP_2 peak were now resolved from the as-measured Mg 2p - Al 2p AR-XPS spectra, as follows (see Fig. 3.2a).

(i) First, the lower BE side of the Al 2p - BP_2 peak envelop was set to zero (background) intensity by subtraction of a constant background, the value of which was taken equal to the averaged minimum intensity in the BE range of 65-71 eV between the first and second BP peak of the Mg 2p main peak (cf. Fig. 3.2a).

(ii) Because the measured Al 2p spectra of the bare alloy also contain a contribution from the BP_2 peak, a subtraction of the inelastic background prior to the reconstruction of the intrinsic metallic main peak (as for the procedure employed in Sec. 3.1.1 to resolve the Mg 2p main peak) is not possible. In stead, the metallic Al 2p main peak and BP_2 peak were resolved from the zero-background corrected spectrum, as obtained after (*i*), by LLS fitting of the spectrum with the sum of two different asymmetric line shape functions (Fig. 3.2a). As for the metallic Mg 2p main peak (Sec. 3.3.1), the PZL metallic Al 2p main peak is represented by the sum of two identically shaped DS functions (representing the Al $2p^3/_2$-$2p^1/_2$ spin-orbit doublet) convolved with a pure Gauss function.[3] The inelastic background associated with the PZL metallic Al 2p main peak is calculated according to the procedure described in Sec. 3.3.1. The shape of the BP_2 peak, on the other hand, is described by the previously determined Mg 2p DS line shape function (i.e. also the sum of two identically shaped DS functions, as obtained after step (*iii*) in Sec. 3.3.1) after its convolution with a Lorentz function (of given FWHM and unit height). LLS fitting of the total reconstructed to the zero-background-corrected Al 2p – BP_2 spectrum was performed simultaneously for the entire set of AR-XPS spectra recorded at different detection angle sets from a single bare alloy substrate (over the BE range from 65 to 78 eV). The position, height and FWHM of the Al $2p^3/_2$ DS function, the FWHM of the Lorenz function, as well as the position and height of the BP_2 peak, were adopted as fit parameters, while allowing only the height of the Al $2p^3/_2$ DS line shape function and the position and height of the BP_2 peak as varying with detection angle (see step (*iii*) in Sec. 3.3.1).

---

[3] The Al $2p^3/_2$-$2p^1/_2$ spin-orbit splitting and intensity ratio were fixed at known values of 0.36 eV and 0.5, respectively (cf. Ref. 52). The singularity index γ and the instrumental broadening factor, dE, were taken equal to the values as determined for the metallic Mg 2p main peak (see Sec. 3.3.1).

(iii) Finally, the PZL intensity of the metallic Al 2p main peak (for each detection angle) was obtained by integrating the optimized metallic Al 2p main peak as determined by the fitting described in (*ii*), after subtraction of its associated inelastic background.

3.4 AR-XPS spectra of the oxidized alloy substrate

3.4.1 Resolving the metallic and oxidic Mg 2p main peaks

For the case of the *oxidized* MgAl substrate, the PZL intensities of the metallic and oxidic Mg 2p main peaks were determined from as-measured Mg 2p XPS spectra, as follows (see Fig. 3.3b).

(i) First, the lower BE side of the Mg 2p peak envelop was set to zero (background) intensity by subtraction of a constant background (see Sec. 3.3.1).

(ii) Next, the PZL metallic Mg 2p main peak (due to Mg in the substrate) plus its associated inelastic background was constructed from the shape and position of the metallic Mg 2p main peak as resolved from the corresponding spectrum of the bare alloy substrate (Sec. 3.3.1) and adopting Tougaard's formalism [55] for the case of the alloy substrate covered with a thin MgO film of uniform thickness (see also Refs. [29, 48]). Similarly [29, 48], an *oxidic* Mg 2p main peak plus its associated inelastic background was constructed using a symmetric, mixed Gaussian-Lorentzian line shape function [30]. For the calculation of the inelastic 'Tougaard' background associated with the PZL metallic and oxidic Mg 2p main peak, separate three-parameter universal cross sections for inelastic-electron scattering [55] in the alloy (as defined in Sec. 3.3.1) and the oxide (as taken non-zero for energy losses larger than the band gap energy of 7.8 eV for MgO with B = 307 eV^2, C = 100 eV^2 and D = 822 eV^2; see Ref. [55]) were adopted. LLS fitting of the total reconstructed to the zero-background-corrected Mg 2p spectrum of the oxidized alloy was performed simultaneously for the entire set of AR-XPS spectra recorded at different detection angle sets from a single oxidized alloy substrate (over the BE range from 46.5 to 54 eV). To account for possible small energy shifts of the metallic main peak in the measured spectrum of the oxidized alloy with respect to the BE position of the metallic main peak as observed from the bare alloy (e.g. as a result of charging of the thin oxide film during XPS analysis), the BE range of the oxidized alloy spectrum was allowed to shift up to ± 0.05 eV during the fitting. Thus, the position, height, FWHM and Gaussian fraction of the oxidic Mg 2p main peak [30], the height of the metallic Mg 2p main peak, as well as the oxide-film thickness and the BE shift of the oxidized alloy spectrum, were employed as fit parameters, while allowing only the position and height of the oxidic main peak to vary with detection angle.

(iii) Finally, the PZL intensity of the metallic Mg 2p main peak was obtained as described in Sec. 3.3.1. The corresponding PZL intensity of the oxidic Mg 2p main peak was obtained by integration after subtraction of its associated inelastic background (Fig. 3.3b).

3.4.2 Resolving the metallic and oxidic Al 2p main peaks

For the case of the *oxidized* MgAl substrate, the PZL intensities of the metallic and oxidic Al 2p main peaks, as well as the overlapping BP_2 peak (Sec. 3.3.2), were determined from the as-measured Mg 2p - Al 2p XPS spectra, as follows (see Fig. 3.3a).

(i) First, the lower BE side of the Al 2p - BP_2 peak envelop was set to zero (background) intensity by subtraction of a constant background (see Sec. 3.3.2).

(ii) Next, the PZL metallic and oxidic Al 2p main peaks plus their individual inelastic backgrounds, as well as the BP_2 peak, were constructed over the BE range of 65-80 eV according to the procedure described in Sec. 3.4.1 (Fig. 3.3a). To this end, the previously determined shapes and positions of the metallic Al 2p main peak and the BP_2 peak (from the analysis of the corresponding *bare* alloy spectrum; Sec. 3.3.2) and the previously determined (Sec. 3.4.1) values for the oxide-film thickness, the BE shift of the oxidized alloy spectrum and the Gaussian fraction of the oxidic main peak were used. LLS fitting of the total reconstructed to the zero-background-corrected Al 2p – BP_2 spectrum of the oxidized alloy over the BE range from 66 to 78 eV was performed simultaneously for the entire set of AR-XPS spectra recorded at different detection angle sets from a single oxidized alloy substrate. The positions and heights of the metallic and oxidic Al 2p main peaks and the BP_2 peak, as well as the FWHM of the oxidic Al 2p main peak, were employed as fit parameters, while allowing only the heights of the peaks to vary with detection angle.

(iii) Finally, the PZL intensities of the metallic and oxidic Al 2p main peaks were obtained as described in Sec. 3.4.1.

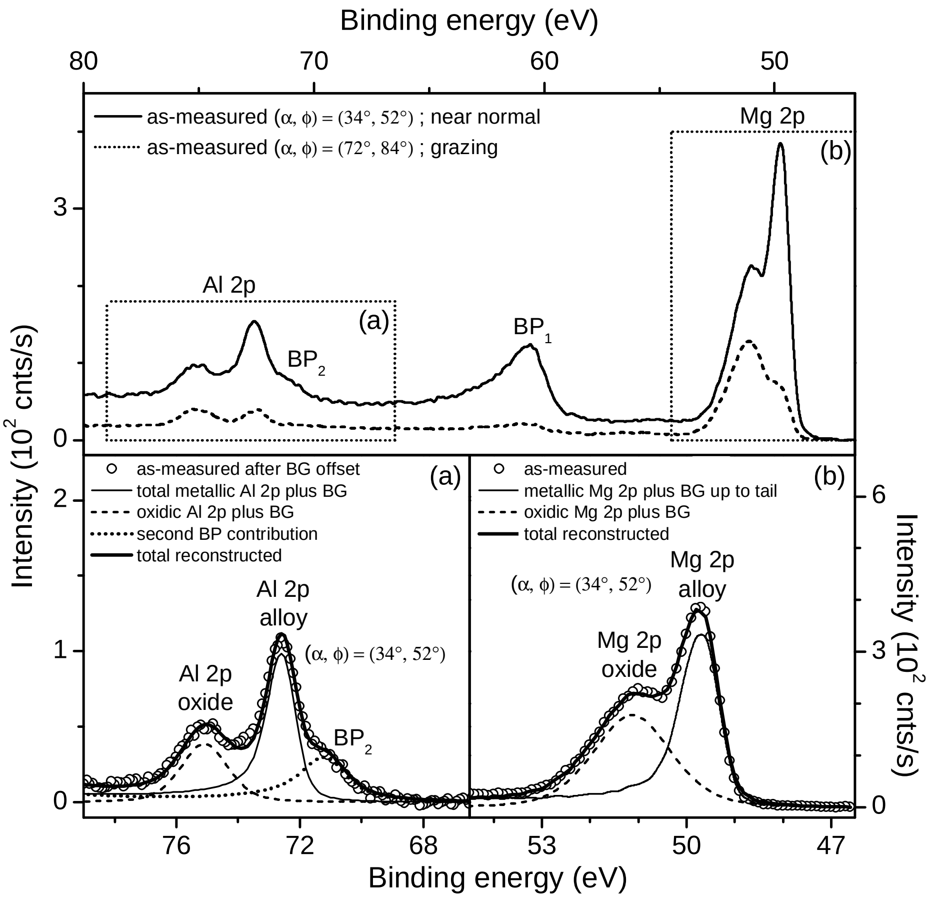

Figure 3.3. As-measured Mg 2p – Al 2p AR-XPS spectra recorded from an oxidized Mg – 7.31 at.% Al substrate (oxidized for 1 h at 304 K at pO_2 = 1×10^{-4} Pa) recorded at near-normal and grazing detection angle sets of (α, ϕ) = (34°, 52°) and (α, ϕ) = (72°, 84°), respectively. (**a**) Reconstruction of the metallic and oxidic Al 2p main peaks (plus their individual inelastic backgrounds, BG) and the second bulk plasmon peak of the Mg 2p main peak (BP_2) for the as-measured Al 2p spectra of the oxidized Mg – 7.31 at.% Al alloy substrate recorded at (α, ϕ) = (34°, 52°) after zero-background offset (for details, see Sec. 3.2.1). (**b**) Reconstruction of the metallic and oxidic Mg 2p main peaks (plus their individual inelastic backgrounds) for the as-measured Mg 2p spectra of the oxidized Mg – 7.31 at.% Al alloy substrate recorded at (α, ϕ) = (34°, 52°) (for details, see Sec. 3.4.1).

3.4.3 Resolving the O 1s main peaks

For the case of the *oxidized* MgAl substrate, the PZL intensities of the identified O 1s main peaks were determined from the as-measured O 1s XPS spectra, as follows (see Fig. 3.4).

(i) First, a Shirley-type background [47, 57] was subtracted from the as-measured O 1s spectra over the BE range of 527-540 eV.

(ii) Next, the background-corrected O 1s spectra was fitted with two symmetric, mixed Gaussian-Lorentzian line shape functions [22, 30], representing the identified, two different O 1s main peaks (see Fig. 3.4). LLS fitting of the total reconstructed O 1s spectrum to the background-corrected O 1s spectrum of the oxidized alloy over the BE range from 527 to 540 eV was performed simultaneously for the entire set of AR-XPS spectra recorded at different detection angle sets from a single oxidized alloy substrate. The positions, heights, FWHM's and the Gaussian fraction of the O 1s main peaks (adopting the same Gaussian fraction for both main peaks) were employed as fit parameters, while allowing only the positions and heights of the peaks to vary with detection angle.

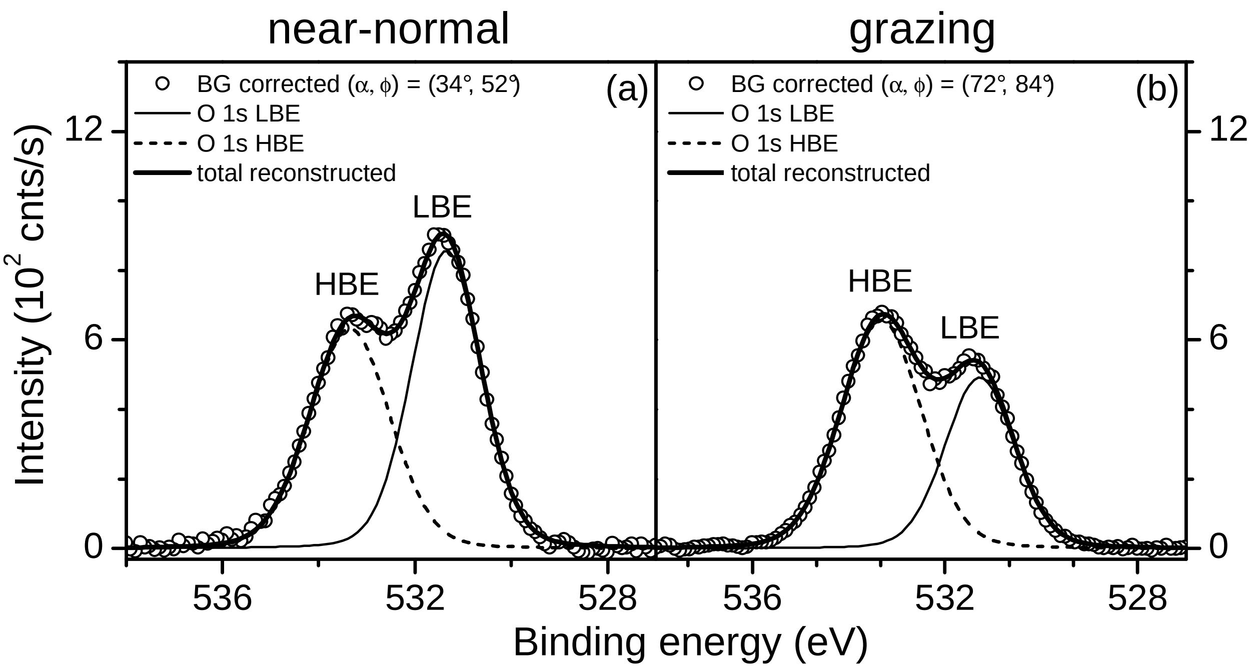

Figure 3.4. Reconstruction of the as-measured O 1s AR-XPS spectra (after subtraction of a Shirley background) as recorded from a oxidized Mg – 7.31 at.% Al substrate (oxidized for 1 h at 304 K and at pO_2 = 1×10^{-4} Pa) at (**a**) near-normal and (**b**) grazing detection angle sets of (α, ϕ) = (34°, 52°) and (α, ϕ) = (72°, 84°), respectively (for details, see Sec. 3.4.3). Two different O 1s main peaks were identified, designated as higher-binding-energy (HBE) and lower-binding-energy (LBE) main peak, respectively.

(iii) Finally, the PZL intensities of the O 1s main peaks were obtained by integration of the spectrum obtained by fitting (Sec. 3.3.1).

3.5 Quantification

3.5.1 Oxide-film thickness and composition

The values of the thickness (and the corresponding standard deviations) of the grown oxide films were calculated from the Mg 2p, Al 2p and O1s PZL intensities, as resolved from the measured AR-XPS of the bare and oxidized alloy substrates (for various detection angle sets; see Sec. 3.3) by using Eqs. (3.A3) to (3.A6) in Appendix A. Further, it is noted that the *total* metallic Mg 2p and Al 2p PZL intensities, i.e. the PZL intensity of the resolved metallic main peak (see Secs. 3.4.1 and 3.4.2, respectively) *plus* their associated intrinsic plasmon intensities, were employed in the calculations by adopting the estimated value of $P_{\mathrm{BP}} = 0.13$ [29, 48] for the intrinsic bulk plasmon excitation probability of both the Mg 2p and Al 2p photoelectron emission processes in the alloy. Five different methods were employed to calculate the thickness of the grown oxide film for a single AR-XPS measurement of the oxidized MgAl substrate (and adopting the physical constants reported in Table 3.1):

(1) From the resolved metallic to oxidic intensity ratio, $I_{\mathrm{MgAl}}^{\mathrm{ovl}} / I_{\mathrm{MgAl\text{-}ox}}^{\mathrm{ovl}}$, by using Eqs. (3.A4) and (3.A5), while adopting the material properties of either MgO or $MgAl_2O_4$ (Table 3.1) to estimate values for the effective attenuation lengths (EALs) $\lambda_{\mathrm{MgAl,ovl}}^{\mathrm{av}}$, $\lambda_{\mathrm{MgAl\text{-}ox,ovl}}^{\mathrm{av}}$ and the total cation molar density, $C_{\mathrm{MgAl\text{-}ox}}$ in the grown oxide film.

(2) Iteratively, from the resolved metallic to oxygen intensity ratio $I_{\mathrm{MgAl}}^{\mathrm{ovl}} / I_{\mathrm{O\text{-}ox}}^{\mathrm{ovl}}$ by using Eqs. (3.A4) and (3.A6) and adopting values for $\lambda_{\mathrm{MgAl,ovl}}^{\mathrm{av}}$, $\lambda_{\mathrm{O\text{-}ox,ovl}}$, $C_{\mathrm{MgAl\text{-}ox}}$ and $C_{\mathrm{O\text{-}ox}}$ as calculated for either MgO or $MgAl_2O_4$.

(3) According to method (1), but now solving the total cation molar density $C_{\mathrm{MgAl\text{-}ox}}$ by iteration (see also Ref. [22]), while assuming a constant oxide-film density (as taken equal to that of either MgO or $MgAl_2O_4$). Thus, any change in the oxide-film density due to a change in the overall stoichiometric composition (i.e. the overall anion to cation ratio) is not accounted for [22].

(4) According to method (2), but now solving the total anion molar density $C_{\mathrm{O\text{-}ox}}$ by iteration (see also Ref. [22]), while again assuming a constant oxide-film density (see above).

(5) From the resolved metallic, oxidic and oxygen intensities (i.e. $I_{\mathrm{MgAl}}^{\mathrm{ovl}}$, $I_{\mathrm{MgAl\text{-}ox}}^{\mathrm{ovl}}$ and $I_{\mathrm{O\text{-}ox}}^{\mathrm{ovl}}$) using Eqs. (3.A4-3.A6), while solving *both* the total cation and anion molar density $C_{\mathrm{MgAl\text{-}ox}}$ and $C_{\mathrm{O\text{-}ox}}$ by iteration (again assuming a constant oxide-film density).

Values for the EALs and asymmetry factors, as required in the various thickness calculations, were determined according to Refs. [36, 49] and using the physical constants as reported in Table 3.1. Note that the effects of the anisotropy of the photoionization cross-section and elastic scattering of the emitted photoelectrons in the solid are accounted for in the quantification by employing the asymmetry factor and the EAL (instead of the inelastic mean free path) in the calculations, respectively [36, 49].

Following the above outlined procedure for each employed detection angle set between (α, ϕ) = (31°, 49°) to (α, ϕ) = (76°, 87°), a total of 30 thickness values are obtained (i.e. 5 different methods of calculation using the PZL photoelectron intensities, as resolved for a set of 6 measured AR-XPS spectra of the oxidized alloy, each recorded at a different detection angle). For each oxidized substrate, the average value of the oxide-film thickness and the error in this value were taken equal to the average and standard deviation of the 30 calculated thickness values, respectively.

Analogously, from the 30 calculated oxide-film thickness values, a corresponding averaged value (and standard deviation) for the overall anion to cation ratio in the oxide film (i.e. $C_{\text{O,ox}}/C_{\text{MgAl,ox}}$) was determined using Eqs. (3.A5) and (3.A6), while adopting values for the EALs $\lambda^{\text{av}}_{\text{MgAl-ox,ovl}}$ and $\lambda_{\text{O-ox,ovl}}$ as calculated for either MgO or $MgAl_2O_4$ (Appendix A). Finally, a corresponding averaged value (and standard deviation) for the overall Mg cation to Al cation ratio in the oxide film was calculated similarly using the expressions for the oxidic intensities $I^{\text{ovl}}_{\text{Mg-ox}}$ and $I^{\text{ovl}}_{\text{Al-ox}}$ (equivalent to Eq. (3.A5)).

3.5.2 Effective depth distribution of resolved species

As follows from the reconstruction of Mg 2p, Al 2p and O 1s spectra of the oxidized alloy substrates (see Figs. 3.3 and 3.4 and Sec. 3.3.2), a total of six different spectral components, corresponding to the different chemical states of Mg, Al and O in the substrate and the oxide film, were identified: i.e. Mg and Al in the alloy substrate and the oxide film (corresponding to the resolved metallic and oxidic Mg 2p and Al 2p main peaks, respectively; Fig. 3.3) and two different chemical species of oxygen in the oxide film (corresponding to the resolved lower (LBE) and higher BE (HBE) O 1s main peaks; Fig. 3.4). By employing their corresponding PZL intensities as resolved for a set of near-normal and grazing detection angles (in the range of α = 25-35º and α = 60-75º, respectively [20, 49]), the corresponding effective depths, <z>, below the specimen surface for the various identified species (Mg, Al and O) within the oxide film and within the region of the alloy substrate adjacent to the alloy/oxide interface (further designated as the alloy *subsurface* region) could be calculated using Eqs. (3.B2) and (3.B3) given in Appendix B, respectively (adopting in Eq. (3.B2) the average oxide-film thickness as calculated according to the procedure described in Sec. 3.4.1).

Table 3.1. Physical constants used for the quantification of the AR-XPS spectra recorded from the oxidized Mg-based MgAl alloys (see Sec. 3.4).

Material	Constant	Value	Unit	Reference
MgAl alloy	$\rho_{MgAl_{2.63}}$	1.76	g/cm^3	from XRD (this work)
	$\rho_{MgAl_{5.78}}$	1.78	g/cm^3	"
	$\rho_{MgAl_{7.31}}$	1.79	g/cm^3	"
	P_{BP}	0.13		[29, 48]
MgO	ρ_{MgO}	3.58	g/cm^3	[58]
	E_g of MgO	7.8	eV	[48]
$MgAl_2O_4$	$\rho_{MgAl_2O_4}$	3.64	g/cm^3	[58]
	E_g of $MgAl_2O_4$	5.8	eV	[59]
MgAl / oxide	$\sigma_{Mg\ 2p}$	0.3335		[60]
	$\sigma_{Al\ 2p}$	0.5371		"
	$\sigma_{O\ 1s}$	2.9300		"
	$\beta_{Mg\ 2p}$	0.93		[33]
	$\beta_{Al\ 2p}$	0.86		"
	$\beta_{O\ 1s}$	2.00		"

Generally the resolved species will be distributed over a certain depth range around the thus obtained effective depth value. Qualitative information on the effective depth *range* of the chemical species can be obtained by calculating the effective depth of the species for a number of different combinations of detection angles (see Sec. 3.5). A relatively large spread of the thus obtained effective depth values then indicates a relatively broad distribution range of the chemical species concerned around the average value of the thus determined effective depth values (see Sec. 3.4.5).

3.6 Results and discussion

The oxide-film thickness has been plotted in Fig. 3.5 as a function of the partial oxygen pressure (pO_2) for the oxidation of a bare 2.63at.% Al and 7.31at.% Al substrates for 1 h at 304 K. These oxide-film thickness values (and the corresponding standard deviations) were calculated according to the procedure described in Sec. 3.4.1, while adopting the material properties of MgO (Table 3.1) to estimate the EALs and molar densities for the oxide film.

The oxide-film thickness values (and the corresponding standard deviations) for the oxidation of the 7.31at.% Al substrate, as determined by adopting either MgO or $MgAl_2O_4$ (Table 3.1) in the thickness calculations, can be compared in Fig. 3.6. It follows that practically identical thickness values were obtained, irrespective of the type of oxide reference (i.e. MgO or $MgAl_2O_4$) used in the calculations. However, the standard deviations for the calculated oxide-film thicknesses are considerably larger when adopting $MgAl_2O_4$ in the thickness calculations (Fig. 3.6), suggesting that the overall oxide film is an 'Al-doped' MgO-type of oxide rather than an $MgAl_2O_4$ spinel-type of oxide (in accordance with the determined oxide-film composition; see below). Further, it can be concluded (Fig. 3.5) that an increase of the bulk Al content from 2.63 to 7.31 at.% only results in a very small decrease of the 'limiting' oxide-film thickness (cf. Refs. [14, 19, 20, 61]) as reached after 1 h oxidation at room temperature. This implies that the oxidation resistance of a Mg-based MgAl alloys at room temperature does not noticeably increase with increasing bulk Al content beyond 2.63 at.% (Fig. 3.5). The 'limiting' oxide-film thickness at room temperature increases distinctively with increasing pO_2 in the range of 10^{-6} to 10^{-4} Pa (Fig. 3.5).

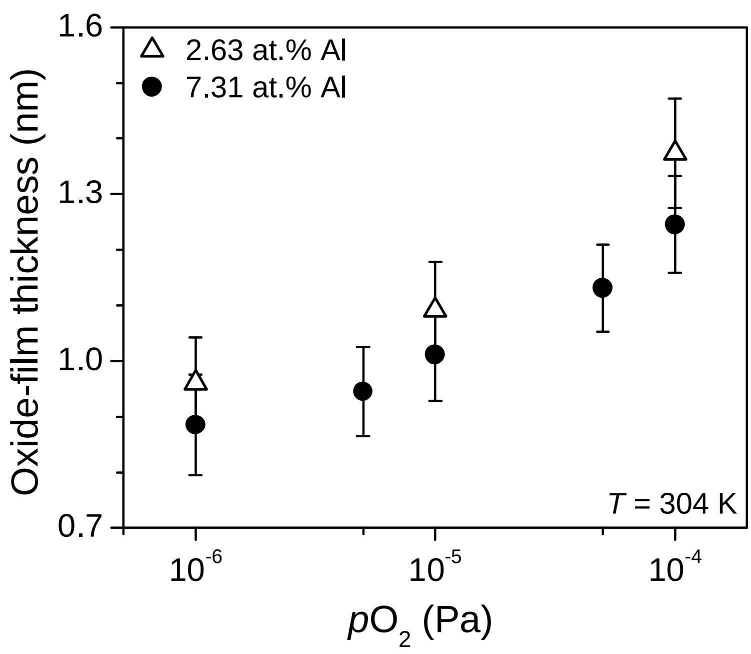

Figure 3.5. Oxide-film thickness as a function of the partial oxygen pressure (pO_2) for the oxidation of the bare Mg – 2.63 at.% Al and Mg – 7.31 at.% Al substrates for 1 h at 304 K. The oxide-film thickness values were determined from the total metallic and oxidic Mg 2p and Al 2p PZL intensities and the O 1s intensities, as resolved from the measured AR-XPS spectra of the oxidized alloy substrate over the angular detection range of (α, ϕ) = (31°, 49°) to (α, ϕ) = (76°, 87°), while using the material properties of MgO (see Table 3.1) to estimate the values for the EALs and molar densities in the grown oxide films (see Sec. 3.4.1).

The calculated effective depths of the resolved metallic and oxidic Mg 2p and Al 2p species, as well as of the resolved O 1s LBE and HBE species, (see Sec. 3.4.2) have been plotted as a function of pO_2 in Figs. 3.7a and b, respectively, for the oxidation of the Mg – 2.63 at.% Al and Mg – 7.31 at.% Al alloy for 1 h at 304 K. It follows that, although the *effective* depths of the resolved species slightly increase with increasing pO_2 and increasing bulk Al content, the *relative* depth distribution of the resolved species is independent of both the bulk Al content and the pO_2. Hence, all grown *oxide films* are relatively enriched in Al *at* the alloy-oxide interface (note that the values for the effective depth of the oxidic Al species are approximately equal to the corresponding oxide-film thickness values; compare Figs. 3.5 and 3.7a). Also the *parent alloy subsurface* region is relatively enriched in Al adjacent to the alloy/oxide interface (Fig. 3.7a).

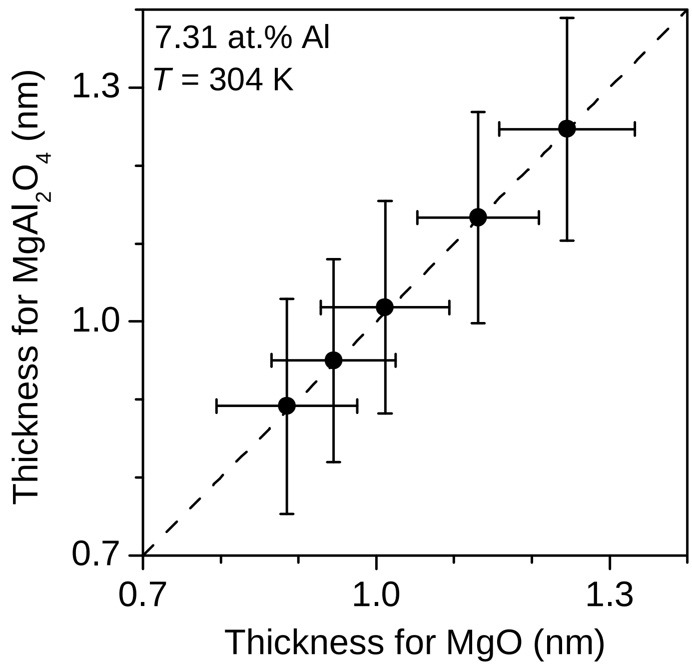

Figure 3.6. Oxide-film thickness values and corresponding standard deviations, as calculated by adopting the EALs and molar densities for $MgAl_2O_4$ as compared with the oxide-film thickness values and standard deviations as determined by using the EALs and molar densities for MgO (see Sec. 3.4.1 and Table 3.1). The data pertain to the oxidation of the bare Mg – 7.31 at.% Al substrate for 1 h at 304 K at various pO_2's (Fig. 3.5).

Further, it follows from Fig. 3.7b that the O 1s LBE represents oxygen in the interior of the grown oxide films, whereas the O 1s HBE species represents oxygen near the outer oxide surface. The thus obtained results on the oxide film and alloy subsurface constitution can be explained supposing that oxide film growth occurs by preferential oxidation of Mg and its subsequent outward cation transport, as discussed in detail in Ref. [50]. The surface of the bare MgAl substrate is already enriched in Al prior to oxidation; due to the combined processes of preferential sputtering and bombardment-enhanced segregation of Mg during the sputter-cleaning treatment (to remove the native oxide; see Sec. 3.2.1), the bare alloy surface is left enriched in Al [62].

The average molar densities of the anionic (i.e. O) and combined-cationic species (i.e. Mg plus Al) in the grown oxide films are shown as function of pO_2 for both alloying element contents in Figs. 3.8a and b. These molar densities are the outcomes of the iterative, thickness calculation schemes 3 to 5 as described in Sec. 3.4.1 (while using the material properties of MgO to estimate values for the EALs in the grown oxide films). The Mg/Al-ratio of the grown oxide films is shown in Fig. 3.8c (calculated as described at the end of Sec. 3.4.1). It follows that the grown oxide films are, on average, deficient of oxygen anions and, to a lesser extent, enriched in cations (with respect to both MgO and $MgAl_2O_4$; see Fig. 3.8a and b,

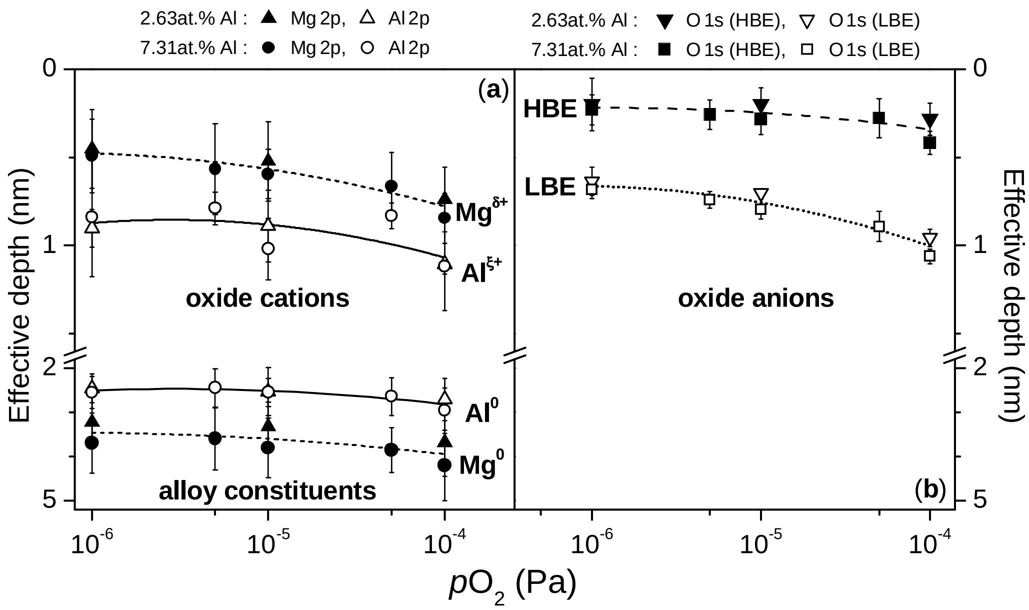

Figure 3.7. Effective depths below the oxide surface as a function of pO_2 for the (**a**) metallic and oxidic Mg 2p and Al 2p species and (**b**) the low (LBE) and high binding energy (HBE) oxidic O 1s species, as resolved (Sec. 3.3.2) from the measured AR-XPS spectra of the oxidized Mg – 2.63 at.% Al and Mg – 7.31 at.% Al substrate (oxidized for 1 h at 304 K). The effective depths of the various species were calculated according to the procedure described in Sec. 3.4.2 (see also Appendix B), while using the material properties of MgO (Table 3.1) to estimate values for the corresponding EALs in the grown oxide films (see Sec. 3.4.1). The dashed and dotted lines are 2nd-order polynomial fits (to guide the eyes) through all data points for a given metallic or oxidic species.

respectively). Further, the anion and cation molar densities are considerably closer to those for MgO than those for $MgAl_2O_4$, which indicates the formation of an 'Al-doped' Mg-oxide film upon room-temperature oxidation of the MgAl alloys, which is consistent with the results

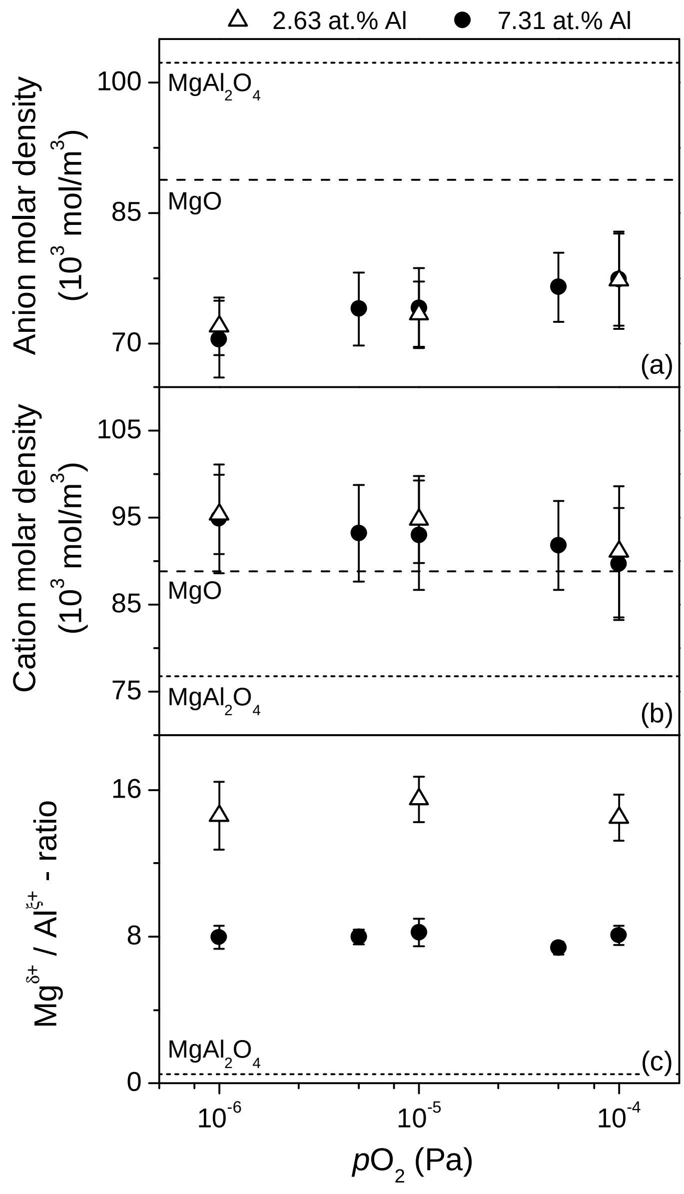

Figure 3.8. Calculated, overall (a) anion molar density, (b) cation molar density and (c) Mg-to-Al cation ratio within the grown oxide films as a function of pO_2 for the oxidation of the bare 2.63 at.% Al and 7.31 at.% Al substrates for 1 h at 304 K. The molar densities and Mg/Al cation ratio for MgO and $MgAl_2O_4$ are represented by the dashed and short-dashed lines, respectively. The average molar densities and Mg/Al-ratios (and their standard deviations) were obtained from the thickness calculation schemes 3 to 5 as described in Sec. 3.4.1 (while using the material properties of MgO to estimate values for the EALs in the grown oxide films).

obtained for the oxide-film thicknesses (see above). Moreover, the Mg/Al ratio of cations in the grown oxide films is much higher (i.e. ≥ 8) than the corresponding stoichiometric value of $^1/_2$ for $MgAl_2O_4$ (Fig. 3.8c). With increasing pO_2, independent of the bulk composition of the alloy, the grown oxide films tend to approach the stoichiometric composition of MgO (Figs. 3.8a and b), while maintaining a constant ratio of Mg to Al cations in the oxide film (Fig. 3.8c). The Al content of the grown oxide films is considerably larger for a higher bulk Al content of the alloy (Fig. 3.8c).

The actual crystallographic structure of the grown oxide films is unknown; i.e. it might be fully amorphous, posses some degree of long range ordering (as for the Al-oxide films in Ref. [23]), or a coherent crystalline oxide film may have formed. For the hypothetical case of crystalline structure of the grown oxide films, the observed overall anion deficiency in combination with overall cation enrichment does not necessarily imply that the defect structure of the non-homogeneous (cf. Fig. 3.7) oxide film actually consists of excess cations on sites of the oxygen anion sublattice. Instead, the overall anion deficiency may arise from a defect structure of the oxide film at its surface (i.e. corresponding with the resolved HBE O1s species; see Fig. 3.7), whereas the slight cation enrichment (relatively smaller as compared to the anion deficiency) may originate from a space charged region in the oxide film adjacent to the alloy/oxide interface (i.e. due the contact potential established at the interface to equilibrate the intrinsic Fermi level of the alloy with that of the oxide [22, 61]).

3.7 Conclusions

Generally applicable methods have been developed for the quantitative determination of PZL intensities from angle-resolved X-ray photoelectron spectra (AR-XPS) of very thin (< 6 nm), multi-element oxide films as grown on metallic binary alloy substrates.

The shape of a bulk plasmon peak associated with a core-level metallic main peak in a measured XPS spectrum of a metal or alloy can be well described by the shape of the resolved intrinsic metallic main peak after its convolution with a Lorentz function of given width and unit height.

Formalism and calculation schemes have been developed to determine accurate values for the thickness, composition and constitution of the grown oxide films on the basis of the resolved total metallic, oxidic and oxygen primary zero-loss intensities.

Application of the outlined procedures to the dry, thermal oxidation of bare Mg-based MgAl substrates at room-temperature revealed that the initial oxide film formed is constituted of an 'Al-doped' MgO-type of oxide phase (rather than an $MgAl_2O_4$ spinel-type of oxide phase). Al-enrichments occur in the regions of the oxide film and the alloy substrate adjacent to the alloy/oxide interface. Two O 1s components were identified: the oxygen species corresponding to the lower and higher BE O1s components occur in the interior of the oxide film and near the outer oxide surface, respectively. The oxide films are, on average, deficient of oxygen anions and (to a lesser extent) enriched in cations (with respect to MgO) and possess an overall Mg/Al-ratio ≥ 8. With increasing pO_2, the grown oxide films tend to approach the stoichiometric composition of MgO. The Al content of the initial oxide film is considerably higher for a higher bulk Al content of the alloy. An increase of the pO_2 upon oxidation results in a considerable increase of the 'limiting' oxide-film thickness reached at room temperatures.

Appendix A. Expressions for the resolved PZL intensities

The total *metallic* Mg 2p and *metallic* Al 2p PZL intensities (i.e. including both the intrinsic tail part towards higher BE's and the intrinsic plasmon loss intensity (see Sec. 3.5.1) associated with each main peak [29, 48, 51-53]), as resolved from the measured spectra of the *bare* alloy substrates (Sec. 3.3.1 and 3.3.2, respectively), will be further denoted as $I_{\mathrm{Mg}}^{\mathrm{bare}}$ and $I_{\mathrm{Al}}^{\mathrm{bare}}$. Employing Eq. (3.B1) in Appendix B, it then follows that the corresponding *summed* metallic PZL intensity, $I_{\mathrm{MgAl}}^{\mathrm{bare}} = I_{\mathrm{Mg}}^{\mathrm{bare}} + I_{\mathrm{Al}}^{\mathrm{bare}}$, is given by

$$I_{\mathrm{MgAl}}^{\mathrm{bare}} = K \cdot \cos\alpha \cdot N\left[(1-x_{\mathrm{Al}})\sigma_{\mathrm{Mg}}\lambda_{\mathrm{Mg}}W_{\mathrm{Mg}} + x_{\mathrm{Al}}\sigma_{\mathrm{Al}}\lambda_{\mathrm{Al}}W_{\mathrm{Al}}\right] \qquad \textbf{(3.A1)}$$

where K is an instrumental factor; α is the angle between the specimen surface normal and the detected photoelectron, N is the atomic density of the alloy; x_{Al} is the bulk atom fraction of Al in the alloy; σ_{Mg} and σ_{Al} are the total photoionization cross-sections for the Mg 2p and Al 2p core level, respectively; W_{Mg} and W_{Al} are the Mg 2p and Al 2p asymmetry factors (see Appendix B); and λ_{Mg} and λ_{Al} are the effective attenuation lengths (EALs) of the detected Mg 2p and Al 2p photoelectrons in the alloy (see Appendix B). With C_{Mg} and C_{Al} denoting the molar densities of Mg and Al in the alloy, the corresponding total molar density, C_{MgAl}, of Mg and Al atoms in the alloy substrate is given by

$$C_{\mathrm{MgAl}} = (1-x_{\mathrm{Al}}) \cdot C_{\mathrm{Mg}} + x_{\mathrm{Al}} \cdot C_{\mathrm{Al}} \qquad \textbf{(3.A2a)}$$

Defining *averaged* values for the *combined* Mg 2p – Al 2p photoionization cross section ($\sigma_{\mathrm{MgAl}}^{\mathrm{av}}$), asymmetry factor ($W_{\mathrm{MgAl}}^{\mathrm{av}}$) and EAL ($\lambda_{\mathrm{MgAl}}^{\mathrm{av}}$) within the alloy as

$$\sigma_{\mathrm{MgAl}}^{\mathrm{av}} \equiv (1-x_{\mathrm{Al}}) \cdot \sigma_{\mathrm{Mg}} + x_{\mathrm{Al}} \cdot \sigma_{\mathrm{Al}} \qquad \textbf{(3.A2b)}$$

$$W_{\mathrm{MgAl}}^{\mathrm{av}} \equiv (1-x_{\mathrm{Al}}) \cdot W_{\mathrm{Mg}} + x_{\mathrm{Al}} \cdot W_{\mathrm{Al}} \qquad \textbf{(3.A2c)}$$

$$\lambda_{\mathrm{MgAl}}^{\mathrm{av}} \equiv (1-x_{\mathrm{Al}}) \cdot \lambda_{\mathrm{Mg}} + x_{\mathrm{Al}} \cdot \lambda_{\mathrm{Al}} \qquad \textbf{(3.A2d)}$$

respectively, Eq. (3.A1) simplifies to

$$I_{\mathrm{MgAl}}^{\mathrm{bare}} = K \cdot \cos\alpha \cdot C_{\mathrm{MgAl}} \cdot \sigma_{\mathrm{MgAl}}^{\mathrm{av}} \cdot \lambda_{\mathrm{MgAl}}^{\mathrm{av}} \cdot W_{\mathrm{MgAl}}^{\mathrm{av}} \qquad \textbf{(3.A3)}$$

Analogously, it follows for the measured spectra of the *oxidized* alloy substrates that the *summed* Mg 2p – Al 2p *metallic* PZL intensity, $I_{\mathrm{MgAl}}^{\mathrm{ovl}} = I_{\mathrm{Mg}}^{\mathrm{ovl}} + I_{\mathrm{Al}}^{\mathrm{ovl}}$ (superscript 'ovl' stands for 'overlayer'), can be expressed by (cf. Eq. (3.B1))

$$I_{\mathrm{MgAl}}^{\mathrm{ovl}} = K \cdot \cos\alpha \cdot C_{\mathrm{MgAl}} \cdot \sigma_{\mathrm{MgAl}}^{\mathrm{av}} \cdot \lambda_{\mathrm{MgAl}}^{\mathrm{av}} \cdot W_{\mathrm{MgAl}}^{\mathrm{av}} \cdot \exp\left(-\frac{L}{\lambda_{\mathrm{MgAl,ovl}}^{\mathrm{av}} \cdot \cos\alpha}\right) \qquad \textbf{(3.A4)}$$

where L denotes the oxide-film thickness and $\lambda^{\text{av}}_{\text{MgAl,ovl}} = (1 - x_{\text{Al}}) \cdot \lambda_{\text{Mg,ovl}} + x_{\text{Al}} \cdot \lambda_{\text{Al,ovl}}$ represents the *combined* (i.e. average) EAL for the detected Mg 2p and Al 2p photoelectrons originating from the alloy and traversing through the oxide.

The total *oxidic* Mg 2p, *oxidic* Al 2p and the O 1s PZL intensities, as resolved from the measured spectra of the *oxidized* alloy substrates, are denoted by $I^{\text{ovl}}_{\text{Mg-ox}}$, $I^{\text{ovl}}_{\text{Al-ox}}$ and $I^{\text{ovl}}_{\text{O-ox}}$, respectively. Employing Eq. (3.B1) in Appendix B, it follows that the corresponding *summed* Mg 2p – Al 2p *oxidic* PZL intensity, $I^{\text{ovl}}_{\text{MgAl-ox}} \equiv I^{\text{ovl}}_{\text{Mg-ox}} + I^{\text{ovl}}_{\text{Al-ox}}$, and the *total oxygen* PZL intensity, $I^{\text{ovl}}_{\text{O-ox}}$, as resolved from the measured spectra of the *oxidized* alloy substrates, are given by

$$I^{\text{ovl}}_{\text{MgAl-ox}} = K \cdot C_{\text{MgAl-ox}} \cdot \sigma^{\text{av}}_{\text{MgAl}} \cdot \lambda^{\text{av}}_{\text{MgAl-ox,ovl}} \cdot W^{\text{av}}_{\text{MgAl}} \cdot \cos\alpha \cdot \left[1 - \exp\left(-\frac{L}{\lambda^{\text{av}}_{\text{MgAl-ox,ovl}} \cdot \cos\alpha}\right)\right] \qquad \textbf{(3.A5)}$$

and

$$I^{\text{ovl}}_{\text{O,ox}} = K \cdot C_{\text{O-ox}} \cdot \sigma_{\text{O}} \cdot \lambda_{\text{O-ox,ovl}} \cdot W_{\text{O}} \cdot \cos\alpha \cdot \left[1 - \exp\left(-\frac{L}{\lambda_{\text{O-ox,ovl}} \cdot \cos\alpha}\right)\right] \qquad \textbf{(3.A6)}$$

respectively. In Eqs. (3.A5) and (3.A6), $C_{\text{MgAl,ox}}$ is the total cation oxide molar density (cf. Eq. (3.A2a)); $\lambda^{\text{av}}_{\text{MgAl-ox,ovl}}$ is the *combined* EAL for the detected Mg 2p and Al 2p photoelectrons originating from and traversing through the oxide (cf. Eq. (3.A2d)), $C_{\text{O-ox}}$ is the total oxygen (i.e. anion) molar density of the oxide film, σ_{O} is the total O 1s photoionization cross section, $\lambda_{\text{O-ox,ovl}}$ is the EAL for the detected O 1s photoelectrons originating from and traversing through the oxide and W_{O} denotes the O 1s asymmetry factor.

Appendix B. Calculation of the effective depths of resolved species

For a given set of angles (α, ϕ) (as defined in Sec. 3.2.2), the observed total primary zero-loss (PZL) intensity, $I_{\text{A}X_n}(\alpha,\phi)$, of photoelectrons ejected with a kinetic energy E from the n^{th} subshell of core-level shell, X, of an elemental species A distributed between depths d_1 and d_2 below the specimen surface, is expressed by (cf. Ref. [49])

$$I_{\text{A}X_n}(\alpha,\phi) = K\sigma_{\text{A}X_n} W_{\text{A}X_n}(\alpha,\phi) \int_{z=d_1}^{d_2} C_{\text{A}}(z) \exp\left[-\int_{z'=0}^{z} \frac{dz'}{\lambda(z',\alpha,\phi,E)\cdot\cos\alpha}\right] dz \qquad \textbf{(3.B1)}$$

where K is an instrumental factor depending on the area of analysis, the energy and flux of the incident X-rays and the solid acceptance angle of the analyzer (*note*: for the AR-XPS measurements performed in the so-called parallel data acquisition mode in the present study [49], K is independent of the angles α and ϕ); $\sigma_{\mathrm{A}X_n}$ is the total photoionization cross-section for the concerned core-level subshell of element A in the solid; $W_{\mathrm{A}X_n}(\alpha,\phi)$ is the asymmetry factor describing the intrinsic anisotropy of the photoionization cross-section [49]; $C_{\mathrm{A}}(z)$ is the molar density (see Appendix A) of elemental species A in the solid as a function of depth z below the specimen surface; $\lambda(z,\alpha,\phi,E)$ is the effective attenuation length (EAL) of the detected photoelectrons with kinetic energy E in the solid as a function of depth z below the specimen surface (*note*: the difference of the EAL's of the photoelectrons traveling through the alloy substrate and the oxide film (i.e. the depth dependence of the EAL) is accounted for by the second integral over dz' [63]). Except close to the extreme near-normal and grazing detection angles ($\alpha < 30°$ and $\alpha > 75°$, respectively), the change in the value of the $\lambda(z,\alpha,\phi,E)$ with the detection angle set (α, ϕ) can in general be neglected [49].

Now, consider the case of an alloy substrate covered with a thin (as compared to the EAL) oxide film of uniform thickness, L. If the species A is distributed over a depth range of d_1 to d_2 *within* the oxide film, the ratio of the corresponding *oxidic* PZL intensities of species A as recorded at two different detection angle sets (α_1,ϕ_1) and (α_2,ϕ_2) is given by

$$\frac{I_{\mathrm{A}X_n}(\alpha_1,\phi_1)}{I_{\mathrm{A}X_n}(\alpha_2,\phi_2)} = \frac{W_{\mathrm{A}X_n}(\alpha_1,\phi_1)\int\limits_{z=d_1}^{d_2} C_A(z)\exp\left(-\frac{z}{\lambda_{ox}(E)\cos\alpha_1}\right)dz}{W_{\mathrm{A}X_n}(\alpha_2,\phi_2)\int\limits_{z=d_1}^{d_2} C_A(z)\exp\left(-\frac{z}{\lambda_{ox}(E)\cos\alpha_2}\right)dz} \qquad \textbf{(3.B1a)}$$

The actual distribution of the oxidic species A over the depth range between d_1 to d_2 is now expressed in terms of an average concentration of the species A at an average, effective depth, <z> by taking the limit of Eq. (3.B1a) for $d_1 \rightarrow d_2$ or for $d_2 \rightarrow d_1$, which both result in the following expression for the effective depth, <z>, of species A in the oxide film:

$$\langle z\rangle = \lambda_{\mathrm{ox}}(E)\frac{\cos\alpha_1\cos\alpha_2}{\cos\alpha_1-\cos\alpha_2}\ln\left[\frac{I_{\mathrm{A}X_n}(\alpha_1,\phi_1)W_{\mathrm{A}X_n}(\alpha_2,\phi_2)}{I_{\mathrm{A}X_n}(\alpha_2,\phi_2)W_{\mathrm{A}X_n}(\alpha_1,\phi_1)}\right] \qquad \textbf{(3.B2)}$$

where $\lambda_{\mathrm{ox}}(E)$ denotes the EAL of the detected photoelectrons with kinetic energy E in the oxide film (as taken independent of the detection angle set (α, ϕ); see above).

For the other case that the elemental species A is concentrated over a depth range of d_1 and d_2 in the subsurface region of the alloy *substrate* (below the thin oxide film of uniform thickness, L), the ratio of the corresponding *metallic* PZL intensities of species A as recorded at two different detection angle sets (α_1,ϕ_1) and (α_2,ϕ_2) is given by

$$\frac{I_{\mathrm{AX}_n}(\alpha_1,\phi_1)}{I_{\mathrm{AX}_n}(\alpha_2,\phi_2)}=\frac{W_{\mathrm{AX}_n}(\alpha_1,\phi_1)\int\limits_{z=d_1}^{d_2} C_A(z)\exp\left(-\frac{L}{\lambda_{ox}(E)\cos\alpha_1}-\frac{d_2-L}{\lambda_{ox}(E)\cos\alpha_1}\right)dz}{W_{\mathrm{AX}_n}(\alpha_2,\phi_2)\int\limits_{z=d_1}^{d_2} C_A(z)\exp\left(-\frac{z}{\lambda_{ox}(E)\cos\alpha_2}-\frac{d_2-L}{\lambda_{ox}(E)\cos\alpha_2}\right)dz} \qquad \textbf{(3.B2a)}$$

Then, the corresponding effective depth, <z>, for the *metallic* species A in the subsurface region of the substrate, as analogously obtained by the taking the limit of Eq. (3.B1c) for $d_1 \rightarrow d_2$, is expressed by

$$\left\langle z\right\rangle = L\left(1-\frac{\lambda_{\mathrm{sub}}(E)}{\lambda_{\mathrm{ox}}(E)}\right)-\lambda_{\mathrm{sub}}(E)\frac{\cos\alpha_1\cos\alpha_2}{\left(\cos\alpha_1-\cos\alpha_2\right)}\cdot\ln\left[\frac{I_{\mathrm{AX}_n}(\alpha_2,\phi_2)W_{\mathrm{AX}_n}(\alpha_1,\phi_1)}{I_{\mathrm{AX}_n}(\alpha_1,\phi_1)W_{\mathrm{AX}_n}(\alpha_2,\phi_2)}\right] \qquad \textbf{(3.B3)}$$

where $\lambda_{\mathrm{sub}}(E)$ and $\lambda_{\mathrm{ox}}(E)$ denote the EAL of the detected photoelectrons originating from the alloy substrate and traversing through the alloy and oxide, respectively.

Chapter 4

Real-time, in-situ spectroscopic ellipsometry for analysis of the kinetics of ultra-thin oxide-film growth on MgAl alloys

M. S. Vinodh, L. P. H. Jeurgens, E. J. Mittemeijer

Abstract

A procedure has been developed to determine the growth kinetics of thin (< 3 nm) oxide films on bare binary alloys from the measured changes of the ellipsometric amplitude ratio and phase shift dependent parameters, ψ and Δ, versus wavelength, as function of oxidation time, as recorded by real-time, in-situ spectroscopic ellipsometry (RISE). The approach has been applied to the dry, thermal oxidation of Mg-based MgAl substrates of low (2.63 at.%) and high bulk Al (7.31 at.%) content at 304 K within the pO_2 range of 10^{-6} to 10^{-4} Pa. Various models have been developed to describe the measured time dependence of the spectra of $\Delta(\lambda)$ and/or $\psi(\lambda)$ for the initial and subsequent stages of oxidation. It followed that the initial oxide-film growth kinetics can be accurately described by adopting a three-node graded oxide layer using the Maxwell-Garnet Effective Medium Approximation (MGEMA) to assess the optical properties of the compositionally inhomogeneous, Al-doped MgO film developing on the MgAl alloy surface. The specific complications that arise in the ellipsometric analysis of the oxidation of binary alloys (as compared to that of pure metals), such as due to the concurrent processes of selective oxidation and (oxidation-induced) chemical segregation, have been discussed.

4.1 Introduction

Ellipsometry is a non-destructive, optical technique based on the principle that linearly polarized light incident on a sample surface is generally reflected as elliptically polarized light upon interaction with the solid. The technique in principle allows the determination of the kinetics of film growth, such as in case of the initial thermal or plasma oxidation of *bare* metal and alloy surfaces under controlled conditions in a UHV chamber.

The amount of ellipticity induced in the reflected polarized light depends, among other factors, on the optical properties of the substrate and the overlying film, as well as on the individual film thickness (cf. Ref. [25, 64-66]). For the in-situ investigation of film growth kinetics by real-time, in-situ spectroscopic ellipsometry (RISE), the changes in the ellipsometric amplitude ratio and phase shift dependent parameters ψ and Δ as a function of oxidation time are measured simultaneously for various wavelengths of the incident polarized light source. The tangent of the angle ψ corresponds to the ratio of the magnitudes of the total reflection coefficients (i.e. the relative amplitude of the reflected wave with respect to that of the incident wave) for the components of the electric field vector of the polarized light vibrating in the plane of incidence (*p-wave*) and perpendicular to it (*s-wave*), respectively. The angle Δ is the difference between the phase shifts experienced upon reflection by the p- and s-waves, respectively (for details, cf. Refs. [25, 64, 66]).

Accurate fitting of the measured changes in *both* $\psi(\lambda)$ and $\Delta(\lambda)$, as a function of time, by adopting a suitable model for the evolving substrate/oxide-film system can give detailed and conclusive information on the growth kinetics, constitution and chemical composition of the developing oxide film as function of the oxidation conditions (as time, temperature, partial oxygen pressure, substrate orientation) [14, 20, 67-70]. These mentioned RISE studies have also shown that the optical properties of the initially grown, non-stoichiometric oxide-films may differ significantly from those of the corresponding bulk oxide (cf. Ref. [14, 20, 67, 68, 71]).

Until now, RISE investigations on initial oxide-film growth on metallic surfaces have mainly been developed for the initial stages of oxygen interaction and subsequent oxidation of *pure metal* surfaces of e.g. Cu [72], Si [73, 74], Be [69], Al [67, 70], Ni [75], Zr [14, 20] and Mg [76-78]. Further, in most of these studies [72-75, 79], only the measured changes in the thickness-sensitive (see Sec. 4.2) parameter $\Delta(\lambda)$ as a function of time have been utilized in the applied fitting procedure to obtain the data on the oxide-film growth kinetics; the associated changes in the $\psi(\lambda)$ as a function of time have only been interpreted qualitatively by comparison with complementary results as obtained by e.g. LEED or work-function measurements [76].

For the thermal or plasma oxidation of pure metals at low temperatures (i.e. $T < \sim 600$ K), where the rate of dissolution and the maximum solubility of oxygen in the parent metal substrate is negligibly small, the optical properties of the parent substrate can generally be taken constant as a function of oxidation time in the quantitative analysis (cf. Refs. [14, 20]). Moreover, the growing oxide-film consists of a single oxide phase (although possibly non-uniform and inhomogeneous). This contrasts with the oxidation of a binary alloy, where the optical properties of the parent alloy substrate surface will vary with oxidation time as a result of compositional changes in the alloy substrate induced by the concurrent processes of preferential oxidation and chemical segregation (cf. [50, 80-82] and Secs. 4.3 and 4.4). Moreover, a multiple-element oxide-film (e.g. comprising an oxide solid solution, a spinel oxide phase and/or a doped oxide phase) of unknown and variable optical constants is generally formed upon oxidation of a binary alloy surface [50].

Probably because of the increased complexity of the oxidation behaviour of alloys as compared to pure metals, except for a single study on the plasma oxidation of GaAs [74, 79], no RISE studies have been reported in the literature, which provide data on the kinetics of oxide-film growth on a bare alloy surface through quantitative analysis of the measured changes of both $\psi(\lambda)$ and $\Delta(\lambda)$ as a function of oxidation time.

In the present RISE study, a method is presented to establish the kinetics of oxide-film growth on Mg-based alloys by modelling the measured changes in $\psi(\lambda)$ and $\Delta(\lambda)$ as a function of oxidation time over the wavelength range of 350-700 nm. To this end, bare Mg-based MgAl alloy substrates with two different Al contents, 2.63 and 7.31 at.% Al, were exposed to pure oxygen gas in a UHV reaction chamber (RC) at 304 K in the partial oxygen pressure (pO_2) range of 10^{-6}-10^{-4} Pa. Three different models are presented that describe the measured variations in $\psi(\lambda)$ and $\Delta(\lambda)$ as function of time. The limitations of each model are discussed based on the ability of the model to describe the measured time dependence of $\psi(\lambda)$ and $\Delta(\lambda)$. The experimentally obtained growth curves as a function of pO_2 and Al alloying content are compared with those obtained independently by angle-resolved x-ray photoelectron spectroscopy (AR-XPS).

4.2 Experimental

Two MgAl alloys with Al contents of 2.63 and 7.31 at.% were employed in the present investigation (for details on sample preparation, see [50]). The samples were introduced in the

UHV chamber for angle-resolved XPS analysis (AR-XPS; base pressure < 5×10^{-8} Pa; see below) directly coupled to the UHV reaction chamber (RC; base pressure < 3×10^{-8} Pa) for controlled oxidation and RISE analysis. Prior to each oxidation, the (native) oxide and other contaminants on the sample surface (generally only adventitious carbon) were removed by sputter-cleaning (SC) applying a 1 kV Ar^+ beam, rastering the entire sample surface, until no other elements than Mg and Al were detected in a measured XPS survey spectra recorded over the binding energy (BE) range from 0 to 1200 eV (for instrumental details, see below). The MgAl specimens, as obtained after the aforementioned SC treatment are further designated as bare substrates.

Next, oxide films were grown at 304 K by exposure of the bare substrates to pure oxygen gas (99.997 vol.%) at a partial oxygen pressure (pO_2) in the range of 10^{-6} - 10^{-4} Pa, for total exposure times varying from 300 to 3600 s. The oxygen gas was introduced into the RC by manually adjusting the needle valve to the desired pO_2 (as monitored with a quadrupole mass spectrometer and attaining the desired pO_2 within about 30 s after opening of the valve).

In-situ AR-XPS analysis of the specimen surface before and after oxidation was performed with a Thermo VG Thetaprobe system employing monochromatic incident Al Kα radiation (hν = 1486.68 eV; spot size 400 μm). For details on the calibration of the energy scale of the XPS instrument and the in-situ AR-XPS analysis, see Refs. [49, 50].

Real-time in-situ spectroscopic ellipsometric (RISE) measurements were carried out using a “J. A. Woollam Co., Inc.” rotating compensator ellipsometer (RCE) M-2000L, equipped with a Xe light source (in the range of λ = 245-900 nm in steps of $\lambda \sim 0.8$ nm) and mounted directly on the flanges of the RC. Spectra of $\psi(\lambda)$ and $\Delta(\lambda)$ over the wavelength range λ = 350-700 nm (in intervals of ~0.8 nm) were recorded from the bare and oxidizing alloy over a 2×8 mm^2 ellipse-shaped area with a time step of 2.5 s. The measured values of $\psi(\lambda)$ and $\Delta(\lambda)$ were corrected for possible in-plane and out-of-plane “window effects” due to strain-induced birefringence of the fused-quartz windows. The angles of incidence and reflection of the light were fixed at an angle of 70° with respect to the surface normal.

4.3 Data evaluation

Two typical examples of the change of both ψ and Δ (at λ=525 nm) with increasing oxidation time are shown in Fig. 4.1 for the oxidation of the bare Mg – 7.31 at.% Al alloy substrate for 1 h at 304 K at a low and high pO_2 of 1×10^{-6} and 1×10^{-4} Pa, respectively (for discussion, see

Sec. 4.4). To determine the growth kinetics and optical constants[4] of the developing oxide-film from the measured spectra of $\psi(\lambda)$ and $\Delta(\lambda)$ as function of oxidation time, model descriptions for $\psi(\lambda)$ and $\Delta(\lambda)$ have to be fitted to the measured data. To arrive at an appropriate (i.e. unique and physically realistic) model for the optical behaviour of the substrate/film system, some preknowledge on the developing oxide-film microstructure (e.g. the chemical composition, morphology and phase constitution) is required. In the present study previous results on the evolution of the microstructure of the oxide-film, obtained with AR-XPS, are used [50].

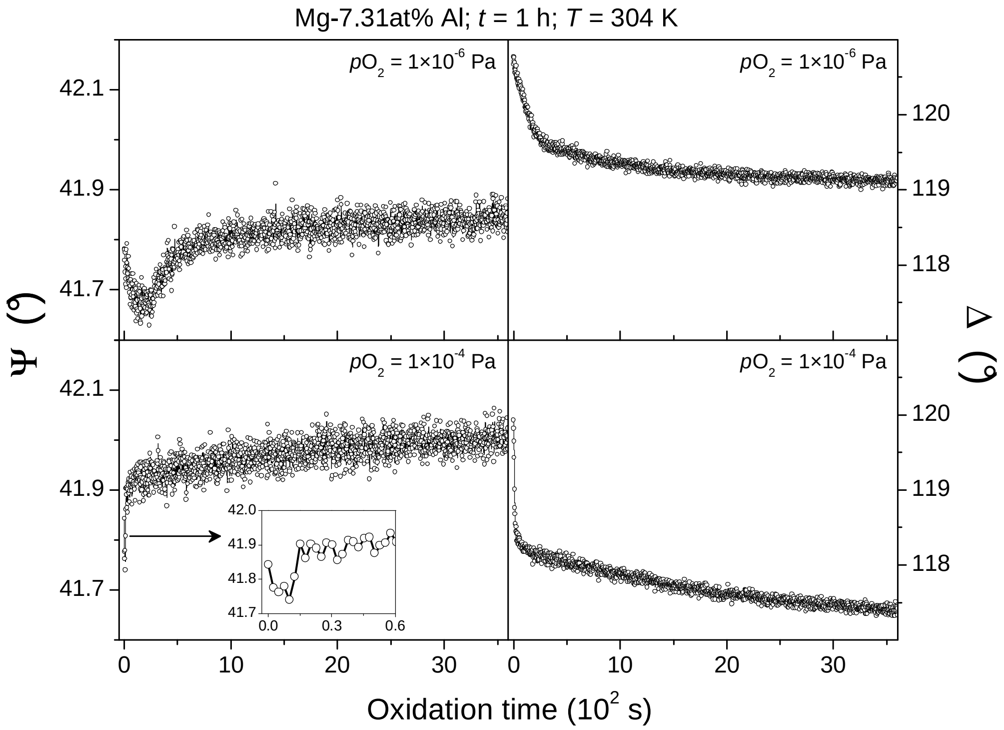

Figure 4.1. Measured values of ψ (*left panels*) and Δ (*right panels*) as a function of oxidation time (at λ = 525 nm) for the oxidation of a bare Mg – 7.31 at.% Al substrate at 304 K for 1 h at $pO_2 = 1\times10^{-6}$ Pa (*upper panels*) and $pO_2 = 1\times10^{-4}$ Pa (*lower panels*). The inset in the lower-left panel shows an enlargement of the time dependence of $\psi(\lambda$ = 525 nm) during the first 60 s of oxidation.

As revealed by the AR-XPS analysis of the oxidized Mg-based MgAl alloys [50], the initial oxide-film consists of an Al-doped MgO-type oxide phase (rather than a $MgAl_2O_4$ spinel-type oxide phase) with Al-enrichments in the regions of the oxide-film and the alloy substrate adjacent to the alloy/oxide interface. The overall Al content of the initial oxide-film

[4] The optical constants of a solid are given by its complex index of refraction, $N = n - ik$, where n and k denote the index of refraction and the extinction coefficient, respectively.

increases with increasing Al bulk content of the alloy. Further, with increasing pO_2, the grown oxide-films approach the stoichiometric composition of MgO. On this basis, three different models were attempted to describe the measured spectra of $\psi(\lambda)$ and $\Delta(\lambda)$ as a function of oxidation time.

4.3.1 The 'alloy|Mg|$MgAl_2O_4$' model

In this model description, further designated as the 'alloy|Mg|$MgAl_2O_4$' model, an intermediate layer of pure Mg of variable thickness (from zero up to a few monolayers) was adopted in-between the bare MgAl substrate and an oxide-film of variable, uniform thickness with optical constants resembling that of $MgAl_2O_4$. The thin intermediate layer of pure Mg was introduced to approximately describe the changes in the optical constants of the parent MgAl substrate as a result of the concurrent processes of preferred oxidation of Mg and oxidation-induced chemical segregation of Mg from the bulk of the alloy to the alloy/oxide interface during the slow (see Sec. 4.4) oxidation regime.

Published values for the refractive index $n(\lambda)$ of $MgAl_2O_4$ [83] were used to approximate the optical constants of the developing, inhomogeneous Al-doped MgO film (see above). Since $MgAl_2O_4$ is transparent over the studied wavelength range (λ = 350–700 nm), the extinction coefficient $k(\lambda) = 0$.

The optical constants of the bare MgAl substrate as a function of λ were straightforwardly determined in this work from the time-averaged values of the $\psi(\lambda)$ and $\Delta(\lambda)$ (cf. Ref. [64, 66]), as recorded in-situ from the bare alloy substrate over a time interval of about 120 s prior to the oxidation. The thus obtained values of $n(\lambda)$ and $k(\lambda)$ for the bare Mg – 7.31 at.% Al substrate prior to its oxidation at various pO_2's between 1×10^{-6} and 1×10^{-4} Pa (i.e. after sputter cleaning with 1 kV Ar^+ beam rastering the entire surface; see Sec. 4.2) have been plotted in Fig. 4.2. Evidently, the values of the $k(\lambda)$ and, in particular, $n(\lambda)$ for the bare MgAl substrate slightly vary upon the successive steps of sputter-cleaning and subsequent oxidation (see Sec. 4.2). These small, apparently random variations in the optical constants of the bare alloy substrate prior to each oxidation step are attributed to one, or a combination, of the following factors:

- Small differences in sputter-induced roughness of the bare alloy surface.
- Compositional differences in the alloy subsurface region due to different extents of the concurrent processes of preferential sputtering of Mg and bombardment-enhanced Gibbsian segregation of Mg during the sputter-cleaning treatment (for details, see Ref. [62]).

- Compositional differences in the alloy subsurface region due to different extents of the competing processes of preferential oxidation of Mg and chemical segregation of Mg from the bulk of the alloy to the alloy/oxide interface during oxidation as inherited from previous oxidation experiments (see Sec. 4.4).

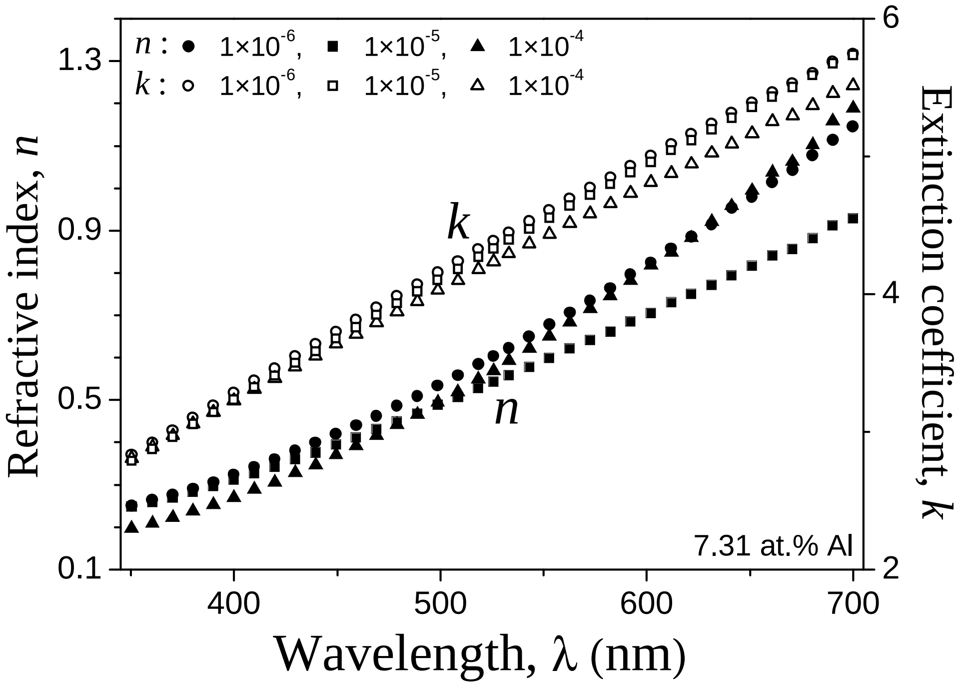

Figure 4.2. The values of the index of refraction (n) and the extinction coefficient (k) as a function of the wavelength (λ), as determined for the bare Mg – 7.31 at.% Al substrate prior to its oxidation for 1 h at 304 K at the designated pO_2.

To exclude any errors in the model calculations introduced by errors in the employed optical constants of the bare alloy substrate at time t = 0, it was therefore essential to separately determine the optical constants of the bare alloy substrate *prior to each* oxidation.

The total oxide-film growth curves were now determined for each oxidation experiment by fitting the calculated spectra of $\Delta(\lambda)$ and $\psi(\lambda)$ to the corresponding measured spectra as a function of the oxidation time and adopting only the thicknesses of the $MgAl_2O_4$ and the intermediate Mg layer as fit parameters. The fitting was performed for each successive time step with the WVASE32 software package (version 3.449) [64] by minimization (using the Lavenberg-Marquardt algorithm) of the mean-squared error (MSE) between the calculated (*mod*) and measured (*exp*) data, as given by

$$\mathrm{MSE} = \frac{1}{2N - M}\sum_{i=1}^{N}\left(\left(\frac{\psi_i^{\mathrm{mod}} - \psi_i^{\mathrm{exp}}}{\sigma_{\psi,i}^{\mathrm{exp}}}\right)^2 + \left(\frac{\Delta_i^{\mathrm{mod}} - \Delta_i^{\mathrm{exp}}}{\sigma_{\Delta,i}^{\mathrm{exp}}}\right)^2\right) \quad \mathbf{(4.1)}$$

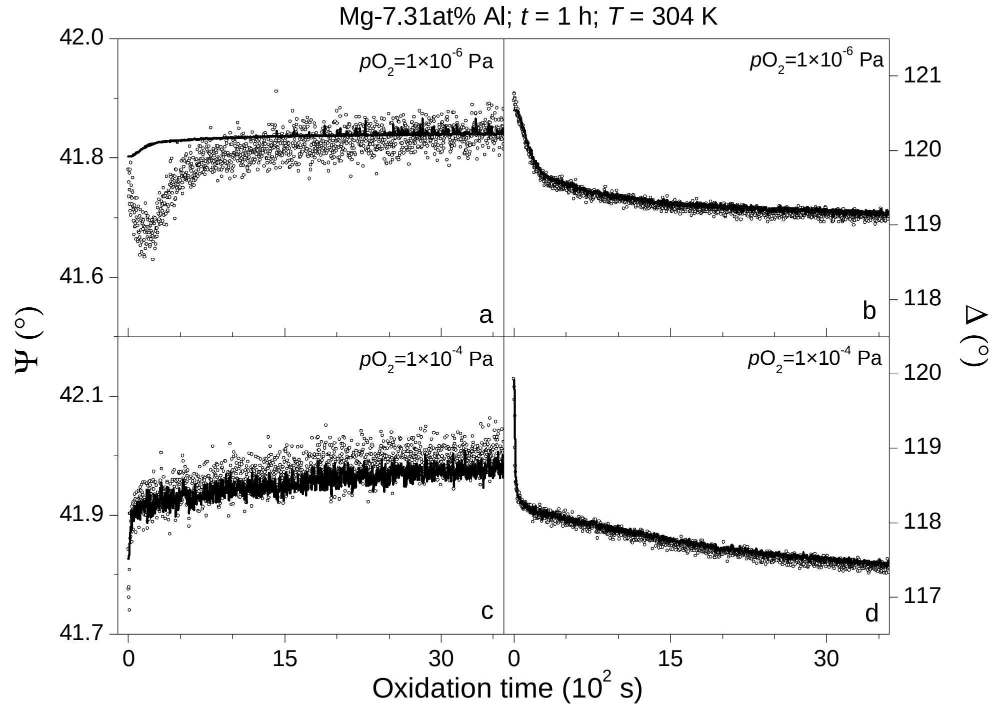

Figure 4.3. The measured (*open markers*) and fitted (*lines*) values of Δ and ψ (at λ = 525 nm) as a function of oxidation time by application of the 'alloy|Mg|$MgAl_2O_4$' model (see Sec. 4.3.1) for the oxidation of the bare Mg – 7.31 at.% Al substrate at 304 K for 1 h at a pO_2 of (a,b) 1×10^{-6} Pa and (c,d) 1×10^{-4} Pa.

where N represents the total number of (Δ , ψ) pairs (as determined by the number of wavelengths considered), M is the number of fit parameters and σ are the standard deviations on the experimental data points. Since each ψ or Δ difference is weighted by the standard deviation of that measured data point (cf. Eq. (4.1)), noisy data are less strongly weighted in the fitting. A result of the fitting of ψ and Δ for λ = 525 nm is shown in Figs. 4.3(a,b) and 4.3(c,d) for the oxidation of the bare Mg – 7.31 at.% Al substrate at a pO_2 of 1×10^{-6} and 1×10^{-4} Pa, respectively. For discussion, see Secs. 4.4.2 and 4.4.3.

4.3.2 The EMA|Grad1 model

In this model description, designated as the 'EMA|Grad1' model, a MgAl substrate with a slight surface enrichment of Mg and covered with a compositionally inhomogeneous, Al-doped MgO oxide-film of variable, uniform thickness is considered.

To describe the changes in optical properties of the parent alloy substrate as a result of the chemical segregation of Mg during the slow (see Sec. 4.4) oxidation regime, an effective medium approximation (EMA) is employed (instead of a thin Mg layer as in the 'alloy|Mg|$MgAl_2O_4$' model; see Sec. 4.3.1). An EMA approach is generally applied to describe a wide range of "mixing" effects, such as surface and interface roughness, compositional or phase mixing and index of refraction grading (cf. Refs. [64, 66, 84]). Here, the optical properties of the parent alloy substrate are estimated with the Bruggeman EMA (BEMA) formalism, employing the complex indices of refraction N_{bare} and N_{Mg} of the bare MgAl substrate (as measured prior to oxidation; see Sec. 4.3.1) and pure Mg, respectively, satisfying:

$$(1-f_{\text{Mg}})\frac{N_{\text{bare}}^2-N_{\text{eff}}^2}{N_{\text{bare}}^2+2N_{\text{eff}}^2}+f_{\text{Mg}}\frac{N_{\text{Mg}}^2-N_{\text{eff}}^2}{N_{\text{Mg}}^2+2N_{\text{eff}}^2}=0 \qquad \textbf{(4.2)}$$

where N_{eff} is the complex index of refraction of the alloy substrate (i.e. the effective medium) and f_{Mg} denotes the equivalent volume fraction (further denoted as EMA fraction) of Mg in the alloy surface region. It is noted that f_{Mg} only represents an *equivalent* volume fraction, which might deviate from the *true* volume fraction in the surface region of the alloy.

To describe the changes in the optical constants of the developing compositionally inhomogeneous, Al-doped MgO film (see above), a graded EMA layer is used. This type of layer is often applied to simulate the effective optical properties of a film of uniform thickness that is inhomogeneous in the direction perpendicular to the sample surface. To this end, two nodes are defined at the top and the bottom of the graded layer, which correspond here with the positions of the oxide surface and the alloy/oxide interface at depths $z = 0$ and $z = L(t)$, respectively ($L(t)$ thus denotes the oxide-film thickness at time t). Further nodes can be defined at intermediate depths $0 \le z \le L(t)$ between the top and the bottom of the graded layer (cf. 'alloy|Grad2' model in Sec. 4.3.3). The film in between two adjacent nodes is sub-divided into multiple, homogenous sublayers of equal thickness (slices) with optical constants that vary slightly from sublayer to sublayer (*here*: a total of 5 slices is adopted). For the graded layer Al-doped MgO films, the complex index of refraction of each slice is described with the Maxwell-Garnet EMA (MGEMA) approach by linearly grading an EMA fraction of Al, $f_{\text{Al}}[z]$, between the top and bottom of a MgO layer of uniform thickness $L(t)$, i.e.

$$\frac{N_{\text{eff},\,i}^2-N_{\text{MgO}}^2}{N_{\text{eff},\,i}^2+2N_{\text{MgO}}^2}+f_{\text{Al},\,i}\frac{N_{\text{Al}}^2-N_{\text{eff},\,i}^2}{N_{\text{Al}}^2+2N_{\text{eff},\,i}^2}=0 \qquad \textbf{(4.3)}$$

where $N_{\text{eff},\,i}$ denotes the complex index of refraction of the i^{th} slice with EMA fraction $f_{\text{Al},\,i}$; N_{MgO} and N_{Al} are the complex indices of refraction of MgO (i.e. the host matrix) and Al metal (i.e. the inclusion). The MGEMA approach has shown to be very successful in describing the changes in optical constants of thin metal-oxide films caused as a result of deviations from their stoichiometric composition [14, 20].

The linear grading of the EMA fraction through the layer implies that the fraction $f_{\mathrm{Al},\,i}$ for any given slice is determined by the total oxide-film thickness, $L(t)$, and the (to be) defined EMA fractions $f_{\mathrm{Al}}[z = 0]$ and $f_{\mathrm{Al}}[z = L(t)]$ at the top and bottom nodes of the graded layer, respectively (for details, see Ref. [64]). To approximately describe a relative enrichment of Al in the oxide-film that increases from the oxide surface towards the alloy/oxide interface (see above and Ref. [50]), the EMA fraction at the top node, $f_{\mathrm{Al}}[z = 0]$, corresponding to Al at oxide surface, was set at zero, while the value of the bottom node, $f_{\mathrm{Al}}[z = L(t)]$, was allowed to vary with oxidation time.

The total oxide-film growth curves were now determined for each oxidation experiment by fitting the calculated spectra of $\Delta(\lambda)$ and $\psi(\lambda)$ to the corresponding measured spectra as a function of the oxidation time (see Sec. 4.3.1) and adopting only the total film thickness and the EMA fraction, $f_{\mathrm{Al}}[z = L(t)]$, at the bottom node of the graded layer (i.e. at the metal/oxide interface) as fit parameters. The EMA fraction, f_{Mg}, of Mg in the parent substrate was fixed at a value of 0.01, 0.05 and 0.05 for the oxidation of the Mg – 2.63 at.% Al substrate at a pO_2 of 1×10^{-6}, 1×10^{-5} and 1×10^{-4} Pa, respectively, as determined from a separate parameter study for each oxidation. Similarly, for the oxidation of the Mg – 7.31 at.% Al substrate at a pO_2 of 1×10^{-6}, 5×10^{-6}, 1×10^{-5}, 5×10^{-5}, 1×10^{-4}, the value of f_{Mg} was fixed at 0.05, 0.05, 0.07, 0.07 and 0.07, respectively. The optical constants adopted for MgO, Mg, and Al over the considered wavelength range (λ = 350–700 nm) were determined in the present study from in-situ spectroscopic measurements of corresponding reference samples. A result of the fitting of ψ and Δ for λ = 525 nm is shown in Figs. 4.4(a,b) and 4.4(c,d) for the oxidation of the bare Mg – 7.31 at.% Al substrate at a pO_2 of 1×10^{-6} and 1×10^{-4} Pa, respectively. For discussion, see Secs. 4.4.2 and 4.4.3.

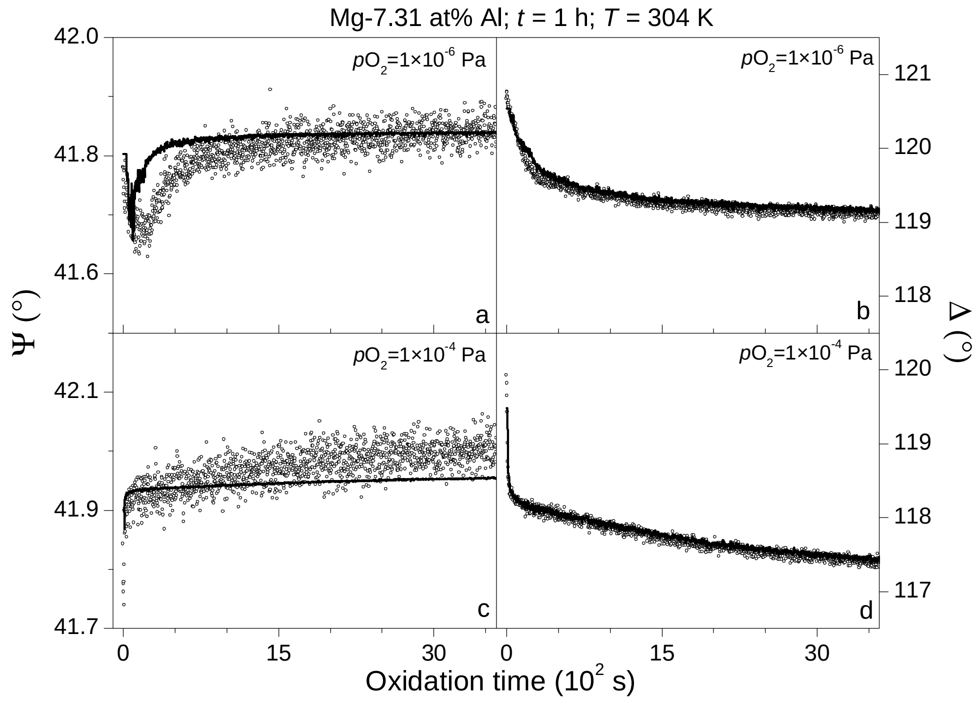

Figure 4.4. The measured (*open markers*) and fitted (*lines*) values of Δ and ψ (at λ = 525 nm) as a function of oxidation time by application of the 'EMA|Grad1' model (see Sec. 4.3.2) for the oxidation of the bare Mg – 7.31 at.% Al substrate at 304 K for 1 h at a pO_2 of (a,b) 1×10^{-6} Pa and (c,d) 1×10^{-4} Pa.

4.3.3 The alloy|Grad2 model

In this model description, designated as the 'alloy|Grad2' model, a bare MgAl substrate covered with compositionally inhomogeneous, Al-doped MgO oxide-film of variable, uniform thickness is adopted.

Thus, any changes in optical properties of the bare MgAl substrate due to variations in the alloy subsurface composition as induced by the competing processes of selective oxidation of Mg and chemical segregation of Mg are neglected in this model. The optical constants of the bare MgAl substrate were experimentally determined from the bare alloy substrate prior to the oxidation (see Sec. 4.3.1).

To describe the effective optical properties of the inhomogeneous Al-doped MgO film, the same graded layer is used as adopted for the 'EMA|Grad1' model described in Sec. 4.3.2 (i.e. using the MGEMA approach and adopting MgO and Al as the host matrix and the inclusion, respectively). However, instead of defining only two nodes at the top and bottom of the graded layer (corresponding with the oxide surface and the alloy/oxide interface, respectively), one additional node is defined at a variable position, $x(t)$, in between the top and bottom node with a fixed EMA fraction of zero, i.e. $f_{Al}[x(t)] = 0$ (with $0 \leq x(t) \leq L(t)$). Further, the EMA fraction at the top node, corresponding with the oxide surface, is also set at zero (i.e.

$f_{Al}[z = 0] = 0$). Thereby, a more flexible description (as compared to the 'EMA|Grad1' model described in Sec. 4.3.2) is obtained for the inhomogeneous distribution of Al in the oxide-film, recognizing that the Al is predominantly concentrated in the bottom part of the film adjacent to the alloy/oxide interface [50].

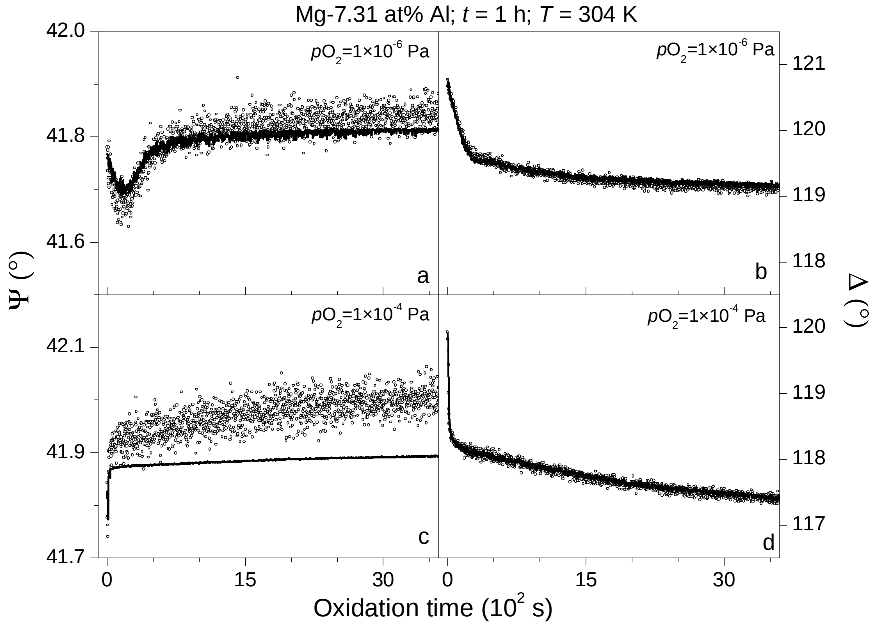

Figure 4.5. The measured (*open markers*) and fitted (*lines*) values of Δ and ψ (at λ = 525 nm) as a function of oxidation time by application of the 'alloy|Grad2' model (see Sec. 4.3.3) for the oxidation of the bare Mg – 7.31 at.% Al substrate at 304 K for 1 h at a pO_2 of (a,b) 1×10^{-6} Pa and (c.d) 1×10^{-4} Pa.

The total oxide-film growth curves were now determined for each oxidation experiment by fitting the calculated spectra of Δ(λ) and ψ(λ) to the corresponding measured spectra as a function of the oxidation time (see Sec. 4.3.1) and adopting only the total thickness and the position of the intermediate node ($f_{Al}[0 \leq x(t) \leq L(t)] = 0$) of the graded layer as fit parameters. The EMA fraction at the bottom node, corresponding with the alloy/oxide interface, was fixed at an average value of 0.75 (i.e. $f_{Al}[z = L(t)\ ] = 0.75$), as determined by a separate fit-parameter study for all oxidation experiments in the present work. A result of the fitting of ψ and Δ for λ = 525 nm is shown in Figs. 4.5(a,b) and 4.5(c,d) for the oxidation of the bare Mg – 7.31 at.% Al substrate at a pO_2 of 1×10^{-6} and 1×10^{-4} Pa, respectively. For discussion, see Secs. 4.4.2 and 4.4.3.

4.4 Results and discussion

4.4.1 The measured time dependences of ψ(λ) and Δ(λ)

The dependences of ψ and Δ (at λ=525 nm) on oxidation time are shown in Fig. 4.1 for the oxidation of the bare Mg – 7.31 at.% Al alloy substrate for 1 h at 304 K at a low and high pO_2 of 1×10^{-6} and 1×10^{-4} Pa, respectively. The maximum variation in ψ over the studied time range is about ten times smaller than the corresponding change in Δ. These behaviours of ψ and Δ with increasing oxidation time for the thermal oxidation of a binary metallic alloy resemble very well to those reported for the thermal oxidation of bare pure metal surfaces (cf. Refs. [69, 76, 77]): Δ decreases as oxidation proceeds, initially very fast, then more gradually during a slow oxidation stage; ψ also shows an initial drop, but then increases, initially fast and subsequently more gradually, during a slow oxidation stage.

The *initial drop* in the value of ψ is of the order of δψ ~ 0.1 - 0.2º, approximately independent of the pO_2, and is comparable to the corresponding values of δψ = 0.164º and δψ = 0.202º as reported for the initial oxidation of a bare Mg(100) and Mg(001) surface, respectively [76]. The time at which the minimum value of ψ is attained increases with decreasing pO_2; e.g. the minimum value of ψ is reached after about 10 s at $pO_2 = 1\times10^{-4}$ Pa and 200 s at $pO_2 = 1\times10^{-6}$ Pa (Fig. 4.1). The initial drop in ψ can be ascribed for the initial incorporation of oxygen into the surface of the parent metal (cf. Refs. [69, 76, 77]) (or, in the present case, alloy) substrate. Because the initial rate of coverage of the alloy surface with chemisorbed oxygen decreases with decreasing pO_2, the concurrent process of oxygen incorporation (and thus the initial decrease ψ) is more prolonged for lower pO_2. Accordingly, it follows that the initial stage of sharply decreasing ψ shows a pronounced temperature dependence (cf. Refs. [50, 69]), because the oxygen sticking coefficient on a bare metal or alloy surface initially increases and subsequently decreases with increasing temperature [19].

The subsequent, *steep increase* of ψ with increasing oxidation time is attributed to the nucleation and growth of 3-dimensional oxide islands on the alloy surface; i.e. a transformation of part of the 'mixed' incorporated layer into three-dimensional oxide islands at the metal surface [19, 76, 77]. With increasing temperature, the initial density of oxide islands decreases and the average islands size increases, because both the surface diffusion of oxygen species and the rate of oxide formation increase with increasing temperature [16].

As soon as a closed 3-dimensional oxide-film has formed on the alloy surface, the values of ψ and Δ increase only gradually upon prolonged oxidation during the final, slow oxidation stage (Fig. 4.3). The onset of this slow oxidation stage is reached after about 20 s at

$pO_2 = 1\times10^{-4}$ Pa and after 750 s at $pO_2 = 1\times10^{-6}$ Pa (Fig. 4.1). At low temperatures (say, $T <$ 600 K), continued oxide-film growth is realized by the coupled currents of cations and/or anions, and of electrons, through the developing oxide-film under influence of the electric field set-up by chemisorbed oxygen species at the oxide surface [7, 15]. The rate of increase of ψ and Δ during the slow oxidation stage increases with increasing pO_2, because the rate of slow, but continuing, oxide-film growth and the rate of segregation of Mg towards the alloy/oxide interface both increase with increasing pO_2 (see Secs. 4.4.2 and 4.4.3). The slow oxidation stage constitutes the main part of the growth curve and is therefore of major interest for the determination of the oxide-film growth kinetics (see Secs. 4.4.2 and 4.4.3).

4.4.2 The fitted time dependences of $\psi(\lambda)$ and $\Delta(\lambda)$

Comparison of the fitted values of Δ (at λ = 525 nm) versus oxidation time, as calculated with the different models presented in Sec. 4.3, with the measured dependence of Δ on oxidation time (i.e. the initial, very fast and the subsequent, gradual decrease in the value of Δ) is accurately and about equally well described for all three models (irrespective of the pO_2 and alloy content; compare Figs. 4.3-4.5). The agreement between the calculated (i.e. fitted) and measured oxidation time dependences of ψ, on the other hand, is very much dependent on the type of model employed, the value of pO_2, as well as on the oxidation stage considered. Further it is noted that, for any given model employed (Sec. 4.3), the changes in Δ and ψ as a function of oxidation time (cf. Figs. 4.3-4.5) are about equally well described over the entire wavelength range of 350-700 nm considered. The 'alloy|Grad2' model describes best the initial drop and subsequent steep increase of ψ during the initial growth stage, which is most pronounced at the lowest pO_2 (1×10^{-6} Pa) (cf. Sec. 4.4.1 and Fig. 4.5). The corresponding oxide-film growth curves, as well as the values attained for the relative position of the intermediate node in the 'Grad2' layer are shown as a function of the oxide-film thickness in Figs. 6a and 6b for the oxidation at low (1×10^{-6} Pa) and high (1×10^{-4} Pa) pO_2, respectively. During the initial, fast growth regime, the position of the intermediate nodein the graded layer shifts from the oxide surface towards the alloy/oxide interface (Fig. 4.6b), suggesting that initially Al-rich oxide islands form on the bare (and Al-rich; see Sec. 4.3.1 and Ref. [62]) alloy surface, (see Sec. 4.4.1). During the subsequent, slow oxidation stage, the intermediate node settles at a position close to the alloy/oxide interface (Fig. 4.6b), suggesting that subsequently overgrowth of a Mg-rich oxide takes place and thereby the Al-enrichment in the oxide-film is confined to the regions in the oxide film adjacent to the alloy/oxide interface.

These results are fully compatible with the results attained by AR-XPS analysis [50]. The 'alloy|Grad2' model does not well describe the subsequent gradual increase of ψ during the slow oxidation stage, which is most pronounced for the highest pO_2 of 1×10^{-4} Pa (Fig. 4.5c).

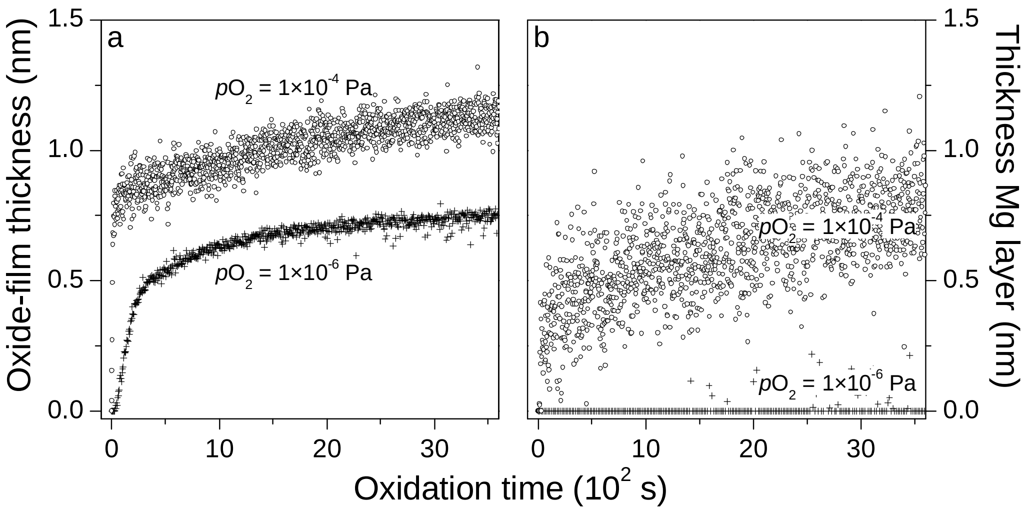

Figure 4.6. Oxidation of the bare Mg – 7.31 at.% Al substrate at 304 K for 1 h at low (1×10^{-6} Pa; *cross markers*) and high (1×10^{-4} Pa; *open markers*) pO_2. (**a**) Oxide-film thickness as a function of oxidation time and (**b**) relative position of the intermediate node in the graded layer as a function of the graded layer thickness. Results shown were obtained by application of the 'alloy|Grad2' model (Sec. 4.3.3).

The 'alloy|Mg|$MgAl_2O_4$' model fails to describe the initial drop and subsequent steep increase of ψ during the initial, fast oxidation stage at low pO_2. However, the 'alloy|Mg|$MgAl_2O_4$' model, which incorporates an intermediate Mg layer of variable thickness (Sec. 4.3.1), does reasonably well describe the gradual increase of ψ during the slow oxidation stage at the highest pO_2 (Fig. 4.3c). The corresponding thicknesses of the graded oxide layer and the intermediate Mg layer have been plotted as a function of oxidation time in Figs. 4.7a and 4.7b for the oxidation at low (1×10^{-6} Pa) and high (1×10^{-4} Pa) pO_2, respectively. The fit parameters for the thicknesses of the graded oxide layer and the intermediate Mg layer are strongly correlated and therefore the results shown exhibit pronounced scatter (compare Figs. 4.7a and 4.7b for $pO_2 = 1\times10^{-4}$ Pa). It follows that, for the highest pO_2 of 1×10^{-4} Pa, the thickness of the intermediate Mg layer, on average, slowly increases with increasing oxidation time during the slow growth regime: from a value of about 0.2 nm to about 0.8 nm (Fig. 4.7b). At $pO_2 \leq 10^{-5}$ Pa, the gradual increase of ψ during the slow growth regime is very small and, consequently, a zero thickness for the intermediate Mg layer is obtained from the fitting (Fig. 4.7b). This suggests that the small, gradual increase of ψ during the slow oxidation stage is

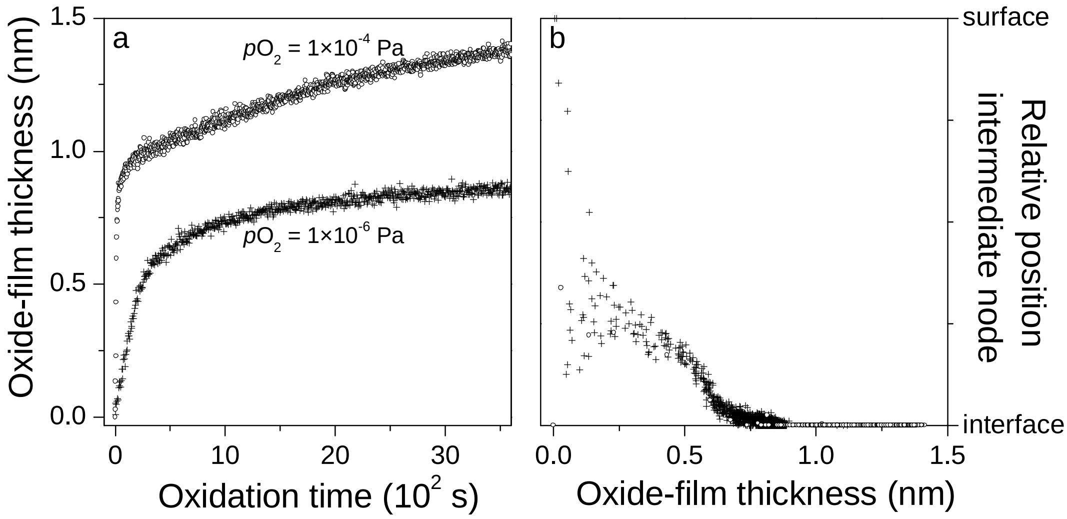

Figure 4.7. Oxidation of the bare Mg – 7.31 at.% Al substrate at 304 K for 1 h at low (1×10^{-6} Pa; *cross markers*) and high (1×10^{-4} Pa; *open markers*) pO_2. Thicknesses of (**a**) the $MgAl_2O_4$ layer and (**b**) the corresponding Mg intermediate layer (i.e. in between the MgAl substrate and the $MgAl_2O_4$ layer) as a function of oxidation time. Results shown were obtained by application of the 'alloy|Mg|$MgAl_2O_4$' model (Sec. 4.3.1).

mainly related to compositional changes in the alloy subsurface region due to the concurrent processes of preferred oxidation of Mg and oxidation-induced chemical segregation of Mg from the bulk alloy towards the alloy/oxide interface. Because an increase of pO_2 is associated with an increase of oxygen activity at the alloy/oxide interface [85], the chemical segregation of Mg increases with increasing pO_2.

The 'EMA|Grad1' model (with a fixed EMA fraction of Mg in the substrate and a two-node, graded layer; Sec. 4.3.2) presents an intermediate case: to some extent, it fits the initial drop and subsequent steep increase of ψ, but fails to describe the subsequent gradual increase of ψ during the prolonged, slow oxidation stage at the highest pO_2 of 1×10^{-4} Pa (Fig. 4.4).

On the basis of the above discussion, it is concluded that the application of a graded layer with a minimum of three nodes (i.e. one top, one bottom and one intermediate node), as employed in the 'alloy|Grad2' model (Sec. 4.3.3), is required to describe the initial drop and subsequent steep increase of ψ at low pO_2, during the initial stage of oxidation which is characterized by oxygen incorporation in the substrate and formation of a continuous closed, 3-dimensional oxide-film. The introduction of an intermediate Mg layer (as in the alloy|Mg|$MgAl_2O_4$ model) or, similarly, adopting a substrate with a variable EMA fraction of Mg (as in the 'EMA|Grad1' model; see Sec. 4.3.2) is needed to describe the gradual increase of ψ during the slow oxidation stage at high pO_2, which is ascribed for the continuous segregation of Mg to the alloy/oxide interface. The above suggests model descriptions incorporating both a 3-node graded layer and an intermediate Mg layer or a variable EMA fraction of Mg in the substrate layer. However, applications of such 'combined' model descriptions all failed, because the fit parameters for the thickness of the graded layer and the thickness of the Mg intermediate layer (or the EMA fraction of Mg in the substrate) are extremely correlated (as already experienced, to a lesser extent, for the 'EMA|Grad1' model; see above discussion of Fig. 4.7): i.e. an increase of the thickness of the intermediate Mg layer (or an increase of the EMA fraction of Mg in the substrate) is associated with a decrease of the thickness of the 3-node, graded layer (and visa versa). This resulted in non-unique values for the fit parameters as a function of oxide time (cf. the strange discontinuity in the oxide-film growth curve for the initial, fast growth regime at low pO_2, as obtained with the 'EMA|Grad1' model in Fig. 4.8a) and a strong scattering of the oxide-film growth curves (especially at high pO_2; cf. Fig. 4.8c). The main purpose of the present work is to establish the oxide-film growth kinetics. Therefore, the results as obtained with the model descriptions that incorporate an intermediate Mg layer (i.e. the 'alloy|Mg|$MgAl_2O_4$' model) or a variable EMA fraction of Mg in the substrate) are further discarded.

4.4.3 The oxide-film growth kinetics

The oxide-film growth curves, as obtained by application of the different models, are shown in Fig. 4.8a-c for the oxidation of the Mg – 7.31 at.% Al substrate for 1 h at 304 K and at pO_2 values of 1×10^{-6}, 1×10^{-5} and 1×10^{-4} Pa, respectively. It follows that the near-limiting thicknesses, as obtained during the slow oxidation stage after 1 h of oxidation, is highest for the 'alloy|Grad2' model and lowest for the 'alloy|Mg|$MgAl_2O_4$' model (intermediate results were obtained for the 'EMA|Grad1' model). The difference between the near-limiting thickness values attained from the 'alloy|Mg|$MgAl_2O_4$' and 'alloy|Grad2' models increases with increasing pO_2 from about 0.12 nm at $pO_2 = 1\times10^{-6}$ Pa to about 0.25 nm at $pO_2 = 1\times10^{-4}$ Pa. As made clear in Sec. 4.4.2, the lower thickness values for the 'alloy|Mg|$MgAl_2O_4$' and 'EMA|Grad1' models are a direct consequence of the introduction in the model descriptions of the intermediate Mg layer or the EMA fraction of Mg in the substrate, respectively (see Sec. 4.3.2).

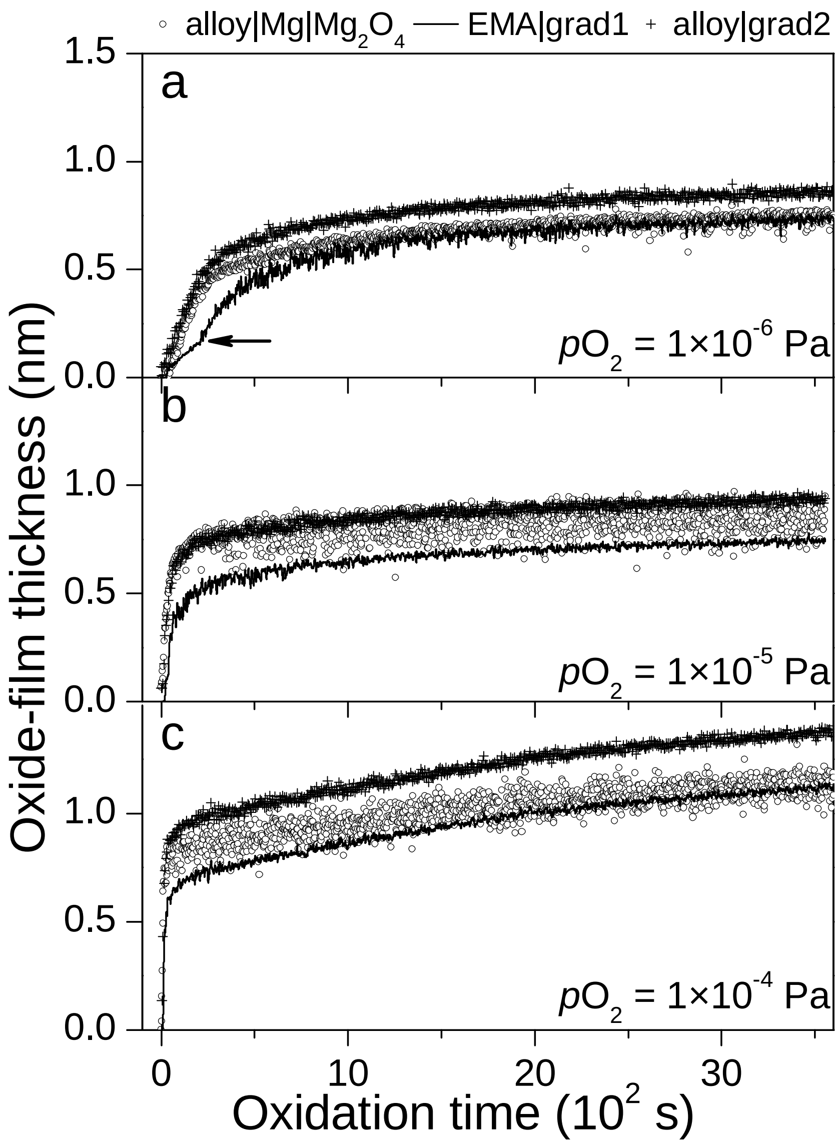

Figure 4.8. The oxide-film growth curves as obtained by application of the various models for the ellipsometric ψ and Δ parameters (Sec. 4.3) for the oxidation of the bare Mg – 7.31 at.% Al substrate at 304 K for 1 h at pO_2s of (a) 1×10^{-6} Pa, (b) 1×10^{-5} Pa and (c) 1×10^{-4} Pa.

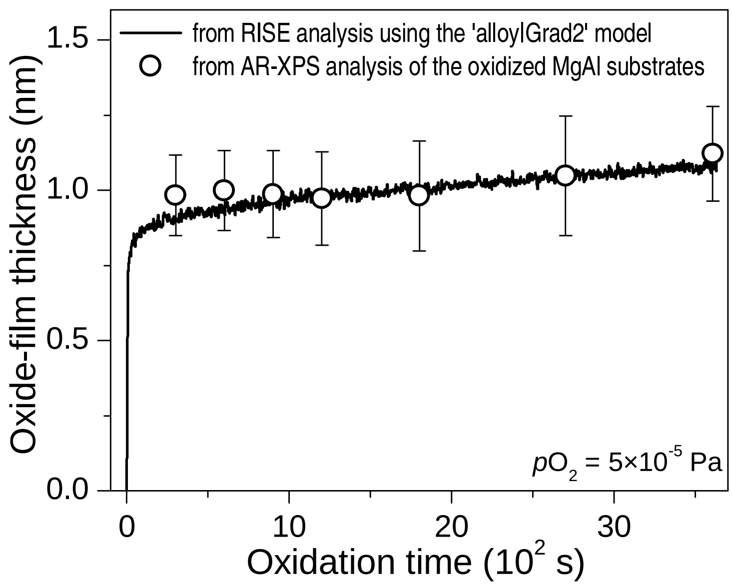

Figure 4.9. Total oxide-film thickness as a function of oxidation time for the oxidation of the bare Mg – 7.31 at.% Al substrate for 1 h at 304 K and $pO_2 = 5\times10^{-5}$ Pa. The thickness values were determined *independently* from in-situ spectroscopic ellipsometry by application of the 'alloy|grad2' model (Sec. 4.3.3; full line in the figure) and from the quantitative analysis of the measured Mg 2p, Al 2p and O 1s AR-XPS spectra of the oxidized alloy substrate (for details, see Ref. [50]; open data points in the figure).

Indeed, only the oxide-film thicknesses as determined using the 'alloy|Grad2' model agree very well with the corresponding oxide-film thickness values, as obtained independently by AR-XPS [50]: see Figs. 4.9 and 4.10. The decrease in Δ (i.e. $\delta\Delta$) upon oxidation of the bare MgAl substrate is approximately linearly related to the corresponding change in the oxide-film thickness, in accordance with the linear approximation for thin ($\leq$ 3 nm) dielectric films (cf. Ref. [25], Chapter 4.4.3.4). For example, as determined using the 'alloy|Grad2' mode for λ = 525 nm, a decrease in Δ ($\delta\Delta$) of 1° corresponds to an increase in the oxide-film thickness of about 0.56 nm. A corresponding linear relationship between ψ and the oxide film thickness is not evident in the present study (i.e. $\delta\psi$), in agreement with the experimental findings in Ref. [86] and the theoretical predictions in Sec. 4.4.3.3 in Ref. [25], stating that, to a first order, the ellipsometric parameter ψ is insensitive to the presence of a transparent thin-film phase between the ambient and substrate media.

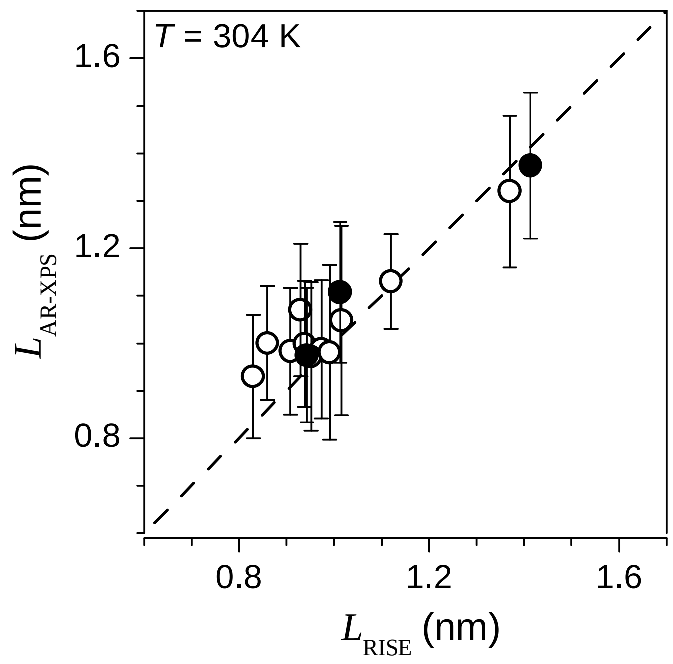

Figure 4.10. Oxide-film thicknesses as obtained from in-situ spectroscopic ellipsometry using the 'alloy|Grad2' model (L_{RISE}; this work) versus the corresponding thicknesses as determined independently by AR-XPS analysis of the oxidized MgAl substrates ($L_{AR\text{-}XPS}$; for details, see Ref. [50]). All data pertain to the thermal oxidation of a bare MgAl substrate alloy at 304 K for various oxidation times (up to 36×10^2 s) and various Al bulk contents (2.63 at.% Al; *solid markers* and 7.31 at.% Al; *open markers*) within the pO_2 range of 10^{-6}-10^{-4} Pa.

4.5 Conclusions

The kinetics of initial growth of oxide films on binary alloys by thermal oxidation at low temperatures can be accurately determined using in-situ, spectroscopic ellipsometry, provided that an appropriate model description, such as a (three-node) graded layer using the Maxwell-Garnet Effective Medium Approximation (MGEMA), is adopted for the compositionally inhomogeneous, multiple-element oxide-film developing on a binary alloy surface.

Application of such modelling to the measured spectra of $\psi(\lambda)$ and $\Delta(\lambda)$ as a function of the oxidation time for the thermal oxidation of bare, Mg-based MgAl substrates at 304 K in the pO_2 range of 10^{-6} to 10^{-4} Pa, then yields a linear relationship between the change in Δ and the change in oxide-film thickness for thicknesses up to about 3 nm. The thus obtained oxide-film thicknesses agree very well with the corresponding thickness values as determined independently by AR-XPS analysis.

The initial drop and subsequent steep increase of ψ during the *initial, fast oxidation stage* is governed by the concurrent processes of oxygen incorporation in the alloy surface, and nucleation and growth of Al-doped MgO islands on the bare MgAl surface. Upon formation of a closed oxide-film (covering the entire alloy surface) during the *slow oxidation stage*, the gradual increase in ψ at high pO_2 is mainly governed by compositional changes in the MgAl subsurface region due to the competing processes of (oxidation-induced) chemical segregation of Mg to the alloy/oxide interface and overgrowth of a Mg-rich oxide by the preferential oxidation of Mg.

Chapter 5

The initial, thermal oxidation of Mg-based MgAl alloys at room temperature

M. S. Vinodh, L. P. H. Jeurgens, E. J. Mittemeijer

Abstract

The initial stages of the thermal oxidation of bare, Mg-based MgAl alloys (containing up to 7.31 at.% Al) at room temperature in the partial oxygen pressure range of $10^{-6} \leq pO_2 \leq 10^{-4}$ Pa were investigated by angle-resolved XPS (AR-XPS) and real-time, in-situ spectroscopic ellipsometry (RISE). It was found that the initial oxide-film microstructure resembles that of an Al-doped MgO-type of oxide. Al-enrichments are present in the oxide film and the alloy subsurface region adjacent to the alloy/oxide interface. The Al-to-Mg content of the grown oxide films is mainly governed by the alloy composition in the subsurface region, which deviates from the bulk alloy composition as a result of the sputter cleaning treatment prior to oxidation. As was shown by performing annealing treatments of the grown oxide films at 450 K in UHV, an observed, additional higher-binding-energy component in the measured O 1s AR-XPS spectra of the oxidized alloys originates from a defect oxide structure adjacent to the oxide-film surface, which acts as a precursor for continued oxide-film growth by outward diffusion of Mg cations under influence of a surface-charge field. The rate of depletion of Mg from the alloy subsurface region during the slow, growth stage upon continual oxidation is governed by the concurrent processes of preferential oxidation of Mg and oxidation-induced, chemical segregation of Mg.

5.1 Introduction

The recent desire to control and optimize the physical and chemical properties (e.g. corrosion resistance, electrical and thermal conductivity, adhesion or catalytic activity) of very thin oxide-films (thickness < 10 nm) on bare alloy surfaces by tailoring both the alloy and oxide-film microstructure has led to a large interest for the low-temperature oxidation behaviour of metallic alloys (cf. Refs. [19, 46, 58, 59]).

Until now, investigations on the thermal oxidation of binary and ternary alloys have been performed mainly at *high* temperatures (i.e. $T > 800$ K) and *high* pressures (i.e. $0.1 < p < 10^5$ Pa), because such conditions are relevant for the application of alloys in high-temperature-resistant coating systems (cf. Refs. [8-10]). At these high temperatures, where relatively thick (in the micrometer range) oxide scales, composed of multiple, *crystalline* oxide phases, develop on the alloy surface by sequential, preferential oxidation of the alloy constituents [8-10], local thermodynamic equilibrium generally prevails at the metal/oxide, oxide/oxide and oxide/gas interfaces. Then, oxide-layer growth is realized by the solid-state diffusion of charged reactants (i.e. cations, anions, electrons, vacancies and holes) through the developing oxide layer under the influence of the (electro)chemical potential gradients [11-13] and, consequently, the oxidation kinetics obeys a parabolic growth law (cf. Refs. [9, 10]).

The thermal oxidation of binary and ternary alloys at *low* temperatures (say, at $T < 600$ K), has been investigated only scarcely up to date. At these temperatures, thermally activated diffusion of reactants through the developing oxide-film is negligibly small and an other driving force, such as due to a surface-charge field set up by negatively charged oxygen species adsorbed onto the oxide surface (cf. Ref. [11, 20, 87]), are required to explain the observed, initially very fast, and subsequent very slow, oxide-film growth kinetics (typically following a logarithmic or cubic growth law). One generally eventually observes a thin oxide-film of near-limiting thickness (< 10 nm) that is constituted of a metastable, multi-element oxide phase [88]. The detailed *microstructure* (i.e. oxide phase constitution, chemical composition, morphology) and the *thickness* of the initial oxide-film formed on an alloy surface at low temperatures is usually unknown. Further, still no comprehensive knowledge exists on the effect of the concurrent processes of (oxidation-induced) chemical segregation and preferential oxidation on both the developing oxide-film microstructure and the induced compositional changes in the alloy subsurface.

In the present contribution, the growth kinetics and the evolution of the microstructure of the initial oxide film grown on Mg-based MgAl surfaces by dry, thermal oxidation at 304K (i.e. room temperature) have been investigated by a combined approach of angle-resolved X-ray photoelectron spectroscopy (AR-XPS) and real-time, in-situ spectroscopic ellipsometry (RISE). Knowledge on and understanding of the low-temperature oxidation of, in particular, Mg-based MgAl alloys is of increasing technological interest in view of a wide range of structural application areas where a low-density (i.e. low weight) alloy is required (e.g. aerospace, automotive industries, laptop casings). Although it is well known that small additions of Al to an Mg base metal improves its corrosion resistance [17, 18], the mechanisms and limits of this improvement is still poorly understood. Against this background, sputter-cleaned, polycrystalline, MgAl alloys of different Al-alloying content (i.e. 2.63, 5.78 and 7.31 at.%) were exposed for various times (up to 1 h) at 304 K to pure oxygen gas at various partial oxygen pressures ($10^{-6} \leq pO_2 \leq 10^{-4}$ Pa) in a UHV reaction chamber. In-situ AR-XPS analysis was applied to determine the thickness, chemical composition and constitution (i.e. the depth distribution of various chemical species within the grown oxide-film) of the developing oxide film as a function of the Al alloying content and the pO_2. RISE analysis was performed to establish the oxide-film growth kinetics [88]. The obtained results on the growth kinetics and developing microstructure of the initial oxide film as a function of oxidation time, bulk Al alloying content and pO_2 could be discussed in terms of the mechanisms and processes governing the initial oxidation.

5.2 Experimental

5.2.1 Material and sample preparation

Three MgAl alloys with an Al content of 2.63, 5.78 and 7.31 at.% were prepared by melting appropriate weight fractions of high purity Mg (< 99.999 wt.%) and Al (<99.99 wt.%) at a temperature of 973K in a graphite crucible in a vacuum–melting furnace (base pressure < 10^{-6} mbar after flushing two times with pure Ar gas) and subsequent casting in a copper mould. The as-cast rods consisted of a MgAl solid-solution matrix (designated as δ-phase) containing small precipitates of the γ-$Mg_{17}Al_{12}$ phase. To dissolve the γ-phase, the as-cast rods were annealed for 24 h at 693 K in a pure Ar gas atmosphere in a sealed quartz tube (sealed after, successively, evacuating, heating and flushing with pure Ar gas) and then quenched in distilled water to obtain a single δ-phase material. The thus obtained rods possessed a non-homogeneous grain-size distribution with pores extending throughout the centre of the rod. To remove the pores, homogenize the grain-size distribution and to decrease the average grain-size, the rods were hammered down by 1 mm (from φ = 11 mm to φ = 10 mm) and subsequently annealed for 1 h at 693 K in a conventional furnace. For each of the thus obtained rods, the Al content, as well as the (impurity) concentrations of Zn, Mn, Fe, Ca, Na, Cu, Ti, Y as determined by Inductive Coupled Plasma – Optical Emission Spectrometry (ICP – OES), have been gathered in Table 5.1.

Table 5.1. Bulk Al content (in at.%) and impurity concentrations (in mass ppm) of the studied Mg-based MgAl alloys (as determined by ICP – OES).

Al (at.%)	Zn (ppm)	Mn (ppm)	Na (ppm)	Fe (ppm)	Ca (ppm)	Cu (ppm)	Ti (ppm)	Y (ppm)
2.63	82 ± 4	38 ± 2	19 ± 2	24 ± 2	< 5	< 5	< 1	< 0.5
5.78	61 ± 3	34 ± 2						
7.31	70 ± 4	38 ± 2	50 ± 5	< 5	< 5	< 5	< 1	19 ± 2

Next, disc-shaped specimens were cut from the thus obtained rods using a diamond saw. The specimen (disc) surfaces were prepared by grinding (using SiC paper down to 5 μm grain size) and subsequent polishing down to 0.25 μm grain size of diamond paste on soft cloths with a mixture of ethanol, soap and distilled water as lubricant. After each polishing step, the specimens were cleaned ultrasonically in ethanol for 15 minutes. Prior to introduction into UHV, the specimens were cleaned ultrasonically for 15 minutes in acetone and 2-propanol. Light optical microscopic analysis showed that all samples possessed an average grain size within the range of 50 – 100 μm.

5.2.2 Oxidation

The specimen was introduced in the UHV chamber for angle-resolved XPS analysis (base pressure < 5×10^{-8} Pa) directly coupled to the UHV reaction chamber for controlled oxidation (RC; base pressure < 3×10^{-8} Pa). Prior to each oxidation, the (native) oxide and other contaminants (generally only adventitious carbon) on the specimen surface were removed by sputter-cleaning (SC) with a 1 kV Ar^+ beam (rastering the entire sample surface) until no other elements than Mg and Al were detected in a measured XPS survey spectrum recorded over the binding energy (BE) range from 0 to 1200 eV (for instrumental details, see Sec.

5.2.3). The MgAl specimens as obtained after the described SC treatment are further designated as *bare* substrates.

Next, an oxide-film was grown on the bare substrate in the RC by exposure to pure oxygen gas (99.997 vol %) for times ranging from 300 to 3600 s at 304 K (i.e. room temperature) at various pO_2's in the range of 10^{-6}-10^{-4} Pa. The oxygen gas was introduced into the RC by manually adjusting the needle valve to set the required pO_2 (as monitored with a quadrupole mass spectrometer) within about 30 s.

5.2.3 AR-XPS analysis and data evaluation

AR-XPS analysis of the specimen surface before and after oxidation was performed with a Thermo VG Thetaprobe system employing monochromatic Al Kα radiation ($h\nu$ = 1486.68 eV; spot size 400 μm). The energy scale of the analyzer was calibrated as described in Ref. [49]. XPS survey spectra, covering a binding energy (BE) range of 0 eV to 1200 eV, were recorded with a step size of 0.2 eV at a constant pass energy of 200 eV. For the bare and oxidized substrate, detailed AR-XPS spectra of the combined Mg 2p and Al 2p regions (BE range 40 - 85 eV) and the O 1s region (BE range 525 - 540 eV; as measured only for the oxidized substrate) were recorded with a step size of 0.1 eV at a constant pass energy of 100 eV. The AR-XPS measurements were performed in so-called parallel data acquisition mode by detecting the photoelectrons simultaneously over the angular detection range of $(\alpha,\phi) = (23^\circ, 43^\circ)$ to $(\alpha,\phi) = (83^\circ, 94^\circ)$ in eight ranges of 7.5° each (for details, see Ref. [49]). The interdependent angles α and ϕ are defined as the angles between the directions of the detected photoelectrons and the sample surface normal and the directions of the detected photoelectrons and the incident photon beam, respectively. To avoid possible grain orientation effects for the weakly textured samples (as verified by X-ray diffraction analysis), the AR-XPS spectra of the bare and oxidized substrates were measured at 9 and 16 defined locations on the surface (spot size 400 μm), respectively, equally distributed over an entire analysis area of 3×3 mm^2.

For the quantification of the measured AR-XPS spectra, the recorded spectra were first averaged over all measured positions of the sample surface for each angular range of photoelectron detection employed (see above). Next, the thus obtained spectra were corrected for the electron kinetic energy dependent transmission of the spectrometer analyzer by adopting the corresponding correction factor as provided by the manufacturer. Then, for each detection angle, the Mg 2p and Al 2p primary zero loss (PZL) intensities [29] of the corresponding asymmetrically shaped Mg 2p and Al 2p metallic main peaks (i.e. including the tail towards higher BE values, but excluding the intrinsic plasmon intensity) [29] and the symmetrically shaped oxidic and O 1s main peaks were resolved from the measured AR-XPS spectra of the bare and the oxidized substrate according to the procedure described in detail in Ref. [89] (see Fig. 5.1). The average BE values (and corresponding standard deviations) as determined for the resolved metallic and oxidic Mg 2p and Al 2p main peaks, as well as for the lower-binding-energy (LBE) and higher-binding-energy (HBE) O1s main peaks, are given in Table 5.2.

The average thicknesses and compositions (and corresponding standard deviations) of the grown oxide films were calculated from the thus resolved Mg 2p, Al 2p and O1s total PZL intensities of the oxidized metal (for various detection angle sets), according to the calculation scheme presented in Ref. [89]. It should be recognized that the *total* metallic Mg 2p and Al 2p PZL intensities, i.e. the PZL intensity of the resolved metallic main peak *plus* its associated intrinsic plasmon intensity [29], were employed in the calculations by utilizing the estimated value of 0.13 [29, 48] for the intrinsic bulk plasmon excitation probability of both the Mg 2p and Al 2p photoelectron emission process in the alloy. Further, the effects of the anisotropy of

Table 5.2. Average binding energy (BE) values (and corresponding standard deviations) of the metallic and oxidic Mg 2p, Al 2p main peaks and the O 1s main peaks (the low binding energy (LBE) and high binding energy (HBE) components), as resolved from the corresponding AR-XPS spectra recorded from the oxidized MgAl substrates.

Species	BE (eV)	FWHM (eV)
metallic Mg 2p	49.64 ± 0.03	
metallic Al 2p	72.52 ± 0.04	
oxidic Mg 2p	51.12 ± 0.08	1.88 ± 0.08
oxidic Al 2p	75.12 ± 0.07	1.87 ± 0.09
O 1s LBE	531.3 ± 0.1	1.67 ± 0.04
O1s HBE	533.4 ± 0.15	1.95 ± 0.05

the photoionization cross-section and elastic scattering of the emitted photoelectrons in the solid were accounted for in the quantification by employing the effective attenuation length, EAL (instead of the inelastic mean free path) and the asymmetry factor in the calculations, respectively [36, 49]. To estimate the EALs of the grown oxide films, the values for the density (3.58 g/cm^3) and band gap (7.8 eV) of MgO were used [89]. The effective depths below the specimen surface for the various identified species (Mg, Al and O) within the oxide film and within the region of the alloy substrate adjacent to the alloy/oxide interface (further designated as the alloy *subsurface* region) were calculated using Eqs. (3.B2) and (3.B3) as given in Ref. [89], respectively.

5.2.4 RISE analysis and data evaluation

RISE measurements were carried out using a “J.A. Woollam Co., Inc.” rotating compensator ellipsometer M-2000L, as equipped with a Xe light source (in the range of λ = 245-900 nm in steps of λ ~ 0.8 nm) and mounted directly on the flanges of the RC. The angles of incidence and reflection of the light are fixed at an angle of 70° with respect to the surface normal. Spectra of the changes in the ellipsometric amplitude ratio and phase shift dependent parameters Δ and ψ versus λ (over λ = 350-700 nm in intervals of ~0.8 nm) were recorded from the bare and oxidizing alloy over a 2×8 mm^2 ellipse-shaped area with a time step of 2.5 s. The Δ and ψ values were corrected for possible in-plane and out-of-plane “window effects” due to strain-induced birefringence of the fused-quartz windows.

To determine the oxide-film growth kinetics, a theoretical model description for the studied substrate/film system was constructed, which describes the measured changes in $\Delta(\lambda)$ and $\psi(\lambda)$ as a function of oxidation time over the wavelength range considered (for details, see Ref. [88]). It followed that the measured changes in $\Delta(\lambda)$ and $\psi(\lambda)$ as a function of time could be accurately fitted by adopting a MgAl alloy substrate covered with an inhomogeneous, Al-doped MgO oxide layer of uniform thickness changing with time (corresponding to the 'alloy|Grad2' model presented in Ref. [88]). The optical constants of the MgAl substrates (as a function of λ) were determined from the in-situ measurement of the bare alloy substrate prior to each oxidation. The optical constants of Al-doped MgO were estimated from the optical constants of pure MgO and Al metal using the effective medium approximation (EMA), while adopting the Maxwell-Garnett formulation and defining MgO as the host matrix [20, 88]. To describe the depth distribution of Al within the Al-doped MgO layer (the Al is mainly located in the part of the oxide film adjacent to the alloy/oxide interface; see Sec. 5.3.2), a so-called 3-node graded EMA layer was employed. To this end, the EMA fraction of Al was graded linearly from 0.75 to zero in-between the bottom and an intermediate, taken variably, position within the MgO layer, while fixing the EMA fraction of Al to zero in the remaining top (i.e. surface-adjacent) part of the MgO layer. For details on the theoretical model description and the corresponding fitting procedure employed to describe the changes in $\Delta(\lambda)$ and $\psi(\lambda)$ as a function of time, see Ref. [88].

5.3 Results

5.3.1 Resolved spectral components

A typical spectral reconstruction for a measured Mg 2p - Al 2p XPS spectrum recorded from the oxidized Mg – 2.63 at.% Al alloy substrate (oxidized for 1 h at 304 K and pO_2 = 1×10^{-4} Pa) at a detection angle-set of $(\alpha,\phi)=(41.8^{\circ},57.9^{\circ})$ is presented in Fig. 5.1. Since the second bulk plasmon peak associated with the metallic Mg 2p main peak further designated as BP_2 peak) overlaps with the metallic and oxidic Al 2p main peaks, serious errors in determination of the corresponding total PZL intensities (and thus in the quantifications) arise if these peaks are not resolved properly. The metallic and oxidic Mg 2p and Al 2p main peaks (plus their individual inelastic backgrounds), as well as the corresponding spectral contribution of the BP_2 peak to the Al 2p PZL intensity, have been resolved according to the procedure described in detail in Ref. [89]: see Figs. 5.1b and 5.1c for the reconstructed Mg 2p and Al 2p regions, respectively. The Mg 2p and Al 2p region could each be accurately described by adopting a single oxidic main peak in combination with the corresponding metallic main peak (plus a reconstructed BP_2 peak present in the Al 2p region; cf. Fig. 5.1c). This already implies that both Mg and Al are incorporated in the developing oxide-film upon oxidation of the bare alloy substrates at 304 K.

The corresponding O 1s spectra of the oxidized MgAl substrates could be well described by adopting two O 1s components, one at the lower and one at the higher BE side of the O 1s peak envelop (further designated as LBE and HBE O 1s main peaks, respectively). Spectral reconstructions for the measured O 1s spectra of the oxidized Mg – 2.63 at.% Al and Mg – 7.31 at.% Al substrates for a near-normal and grazing detection angle sets are shown in Fig. 5.2. It follows that the relative contribution of the HBE O 1s component (with respect to that of the LBE O 1s component) increases with decreasing detection angle (with respect to the oxide surface), indicating that the HBE O 1s component is concentrated in the oxide film closer to the surface (for details, see Sec. 5.4.3). Further, it was found that the relative contribution of the O 1s HBE component to the total O 1s PZL intensity increases with increasing pO_2.

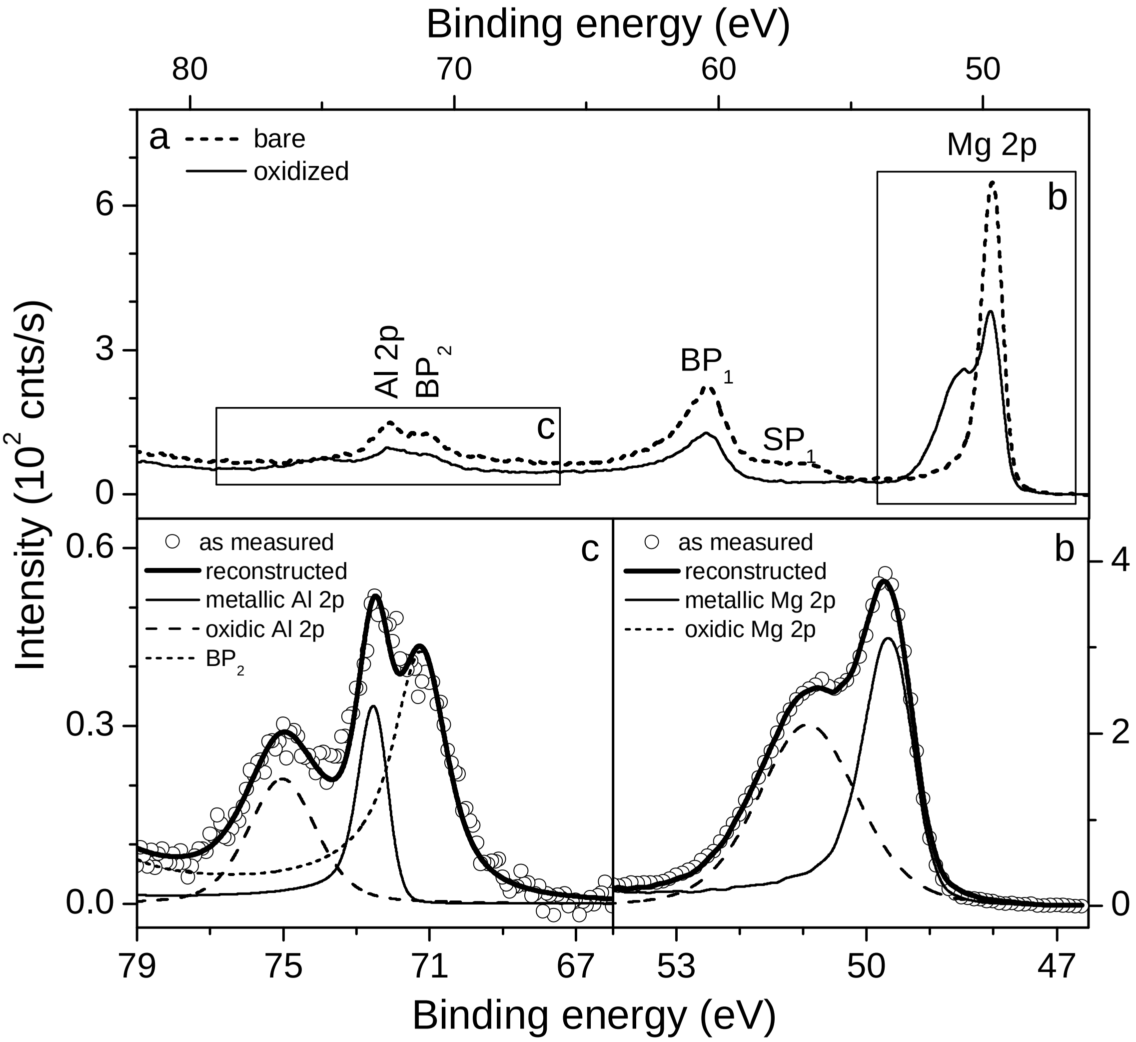

Figure 5.1. (a) As-measured Mg 2p - Al 2p XPS spectra of the bare and oxidized Mg – 2.63 at.% Al substrate recorded at a detection angle set of $(\alpha,\phi) = (41.8^{\circ}, 57.9^{\circ})$ (see Sec. 5.2.2). The spectra of the oxidized alloy pertains to the bare alloy substrate after exposure for 1 h to pure oxygen gas at 304 K and $pO_2 = 1\times10^{-4}$ Pa. The 'as-measured' spectra have been corrected for the analyzer transmission function and zero-background offset [89]. The positions of the Mg 2p and Al 2p main peaks, the first surface plasmon peak (SP_1), as well as the first (BP_1) and second bulk (BP_2) plasmon peaks, associated with the Mg main peak, have been indicated. **(b)** Reconstruction of the metallic and oxidic Mg 2p main peaks (plus their associated inelastic backgrounds, but excluding the asymmetric tail of the metallic main peak occurring towards higher BE's; see Ref. [89]) from the as-measured spectrum of the oxidized alloy shown in (a). **(c)** Reconstruction of the metallic and oxidic Al 2p main peaks (plus their associated inelastic backgrounds), as well as the contribution of the second bulk plasmon peak (BP_2) due to the Mg 2p main peak, from the as-measured spectrum of the oxidized alloy shown in (a). For details, see Ref. [89].

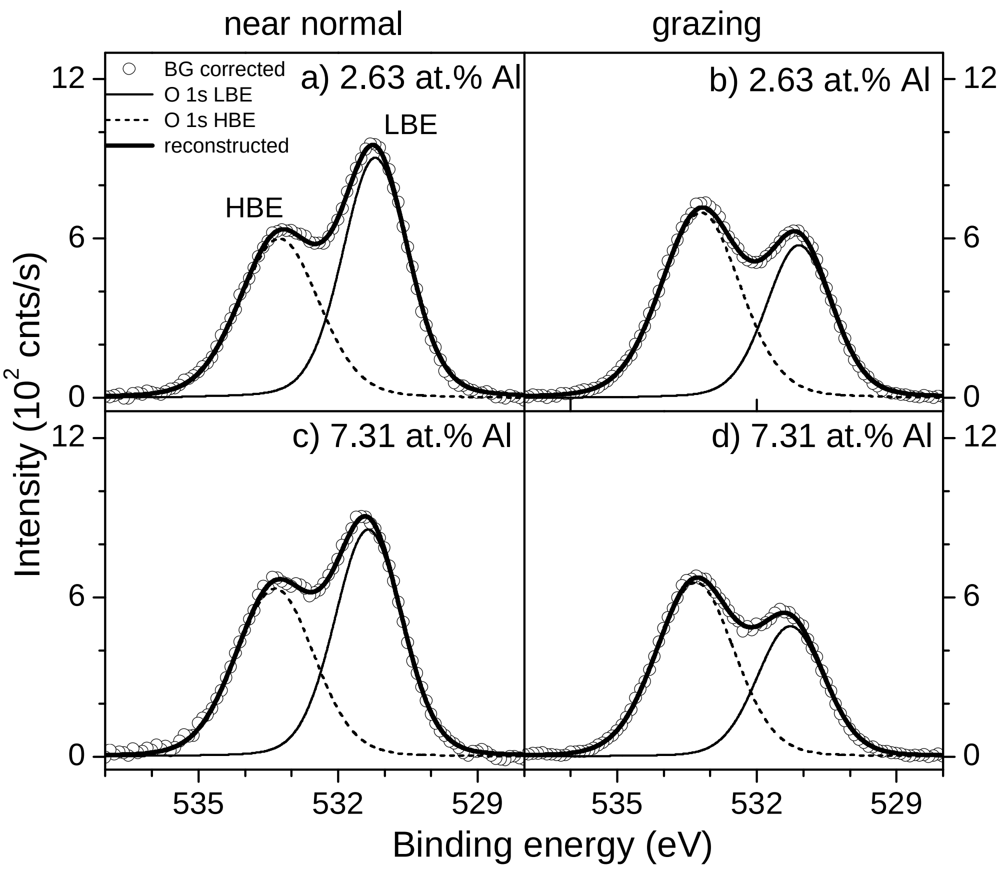

Figure 5.2. The as-measured and reconstructed O 1s spectra of the oxidized 2.63 at.% Al and 7.31 at.% Al substrates (oxidized for 1 h at 304 K and pO_2 = 1×10^{-4} Pa) as recorded at (**a**),(**c**) near-normal and (**b**),(**d**) grazing detection angle-sets of (α,ϕ)=(34.3°,51.7°) and $(\alpha,\phi)=(71.8°,83.8°)$, respectively. For details, see Ref. [89].

5.3.2 Oxide-film constitution

Knowledge on the effective depth distributions of the identified spectral components in the developing oxide film, as well as in the alloy subsurface region adjacent to the alloy/oxide interface, is obtained from the variations of the corresponding, resolved PZL intensities with detection angle (see and Sec. 5.2.3). Adopting the method describe in Ref. [89], the effective depths of the metallic and oxidic Mg 2p and Al 2p species, as well as of the resolved O 1s LBE and HBE species, have been calculated and are shown as a function of pO_2 for the oxidized Mg – 2.63 at.% Al and Mg – 7.31 at.% Al substrates in Figs. 5.3a and b, respectively. It follows that, the *relative* depth distribution of the resolved species is independent of both the bulk Al content and the pO_2. That is, the grown oxide films are relatively enriched in Al *at* the alloy-oxide interface (because the oxidic Al 2p signal pertains to oxide species that is always located at a larger effective depth than oxide given rise to the oxidic Mg 2p signal; Fig. 5.3a). Further it follows that also the alloy subsurface region adjacent to the alloy/oxide interface is relatively enriched in Al (because the metallic Al 2p signal originates from metal located at a smaller effective depth than the metal given rise to the metallic Mg 2p signal; Fig. 5.3a). Finally, the oxide given rise to the O 1s LBE component constitutes the interior of the grown oxide films, whereas the O 1s HBE signal is due to oxide at the outer oxide surface (compare Figs. 5.3a and 5.3b).

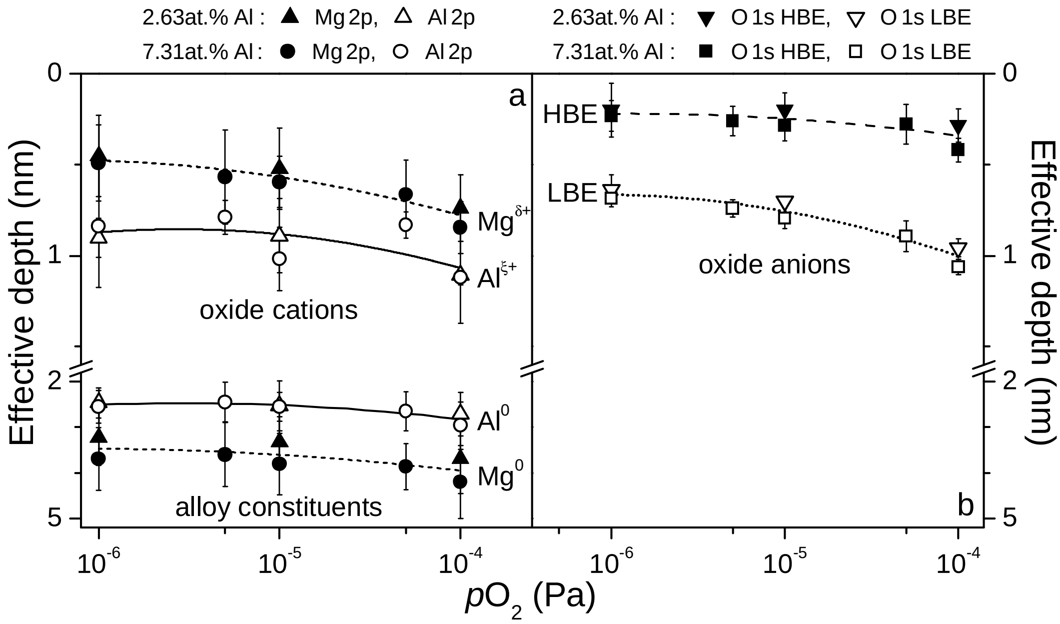

Figure 5.3. Effective depths below the oxide surface, calculated adoping the method described in Ref. [88] as a function of pO_2 for the (**a**) metallic and oxidic Mg and Al species and (**b**) the low binding energy (LBE) and high binding energy (HBE) O species, from the measured AR-XPS spectra of the oxidized 2.63 at.% Al and 7.31 at.% Al substrate (oxidized for 1 h at 304 K at various pO_2). The dashed and dotted lines are 2nd-order polynomial fits through the data points (to guide the eyes).

Further, the effective depth plot calculated for the metallic Mg and Al species of the *bare* MgAl substrates (not shown here) also indicated the presence of a pronounced enrichment of Al in the alloy adjacent to the surface prior to oxidation (i.e. a smaller effective depth for the metallic Al species; see Sec. 5.4.1).

5.3.3 Oxide-film composition

The overall anion-to-cation ratio, calculated from AR-XPS spectra, of the grown oxide films has been plotted as a function of pO_2 for various bulk Al contents in Fig. 5.4a. The corresponding average anion (i.e. oxygen) and cation (i.e. Mg plus Al) molar densities, as

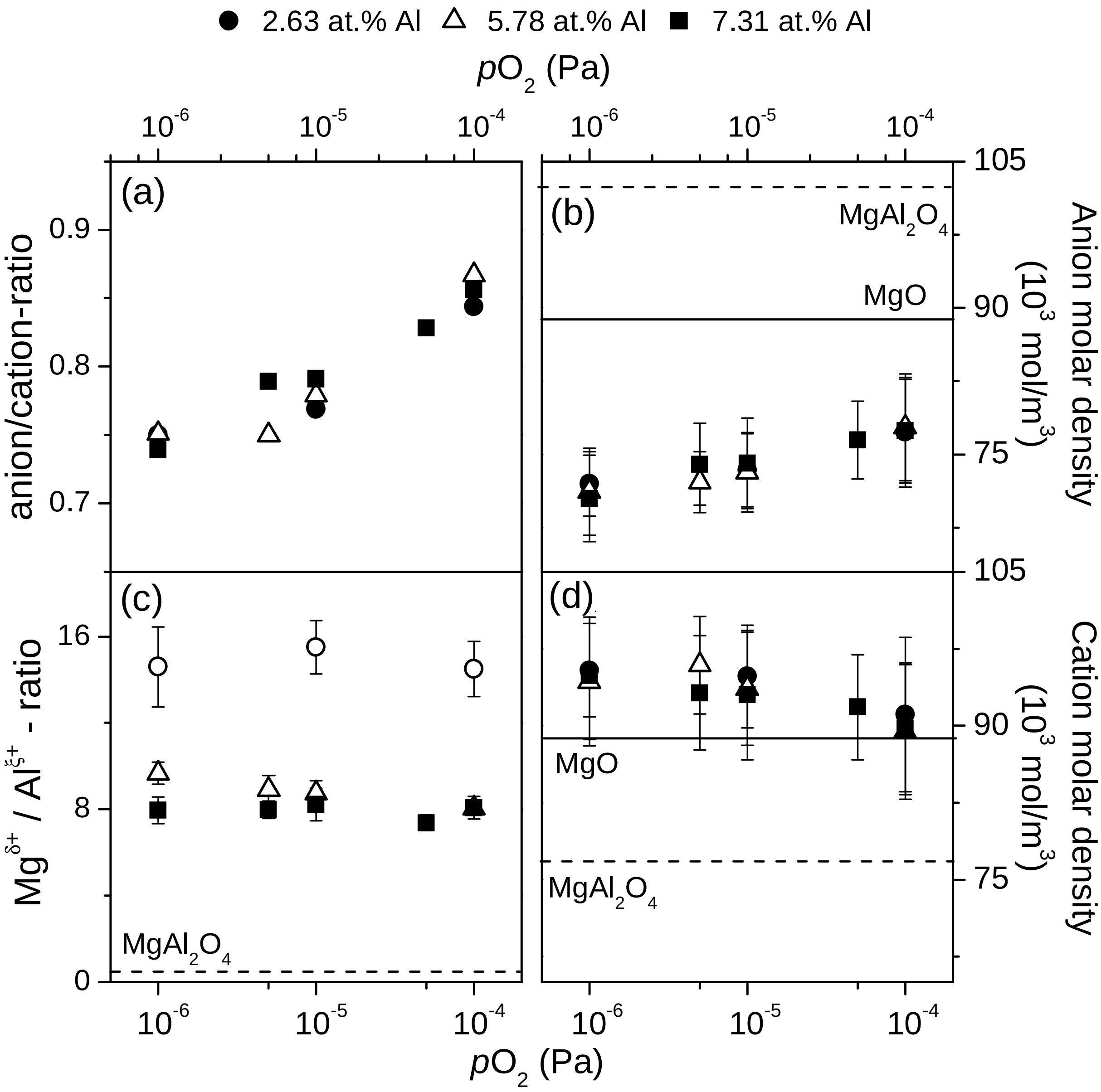

Figure 5.4. (**a**) The overall oxide-film composition, expressed as the overall anion-to-cation ratio (i.e. O/MgAl-ratio) of the grown oxide-films as a function of the pO_2 for various bulk Al alloying contents (as obtained from the AR-XPS analysis of the oxidized alloy substrates; see Sec. 5.2.3 and Ref. [89]). Corresponding (**b**) average anion (i.e. O) molar density, (**d**) average cation (i.e. Mg plus Al) molar density, as well as the (**c**) overall atomic Mg/Al-ratio, of the grown oxide-films. The corresponding values for stoichiometric MgO and $MgAl_2O_4$ are indicated by the dashed and dotted lines, respectively. All data pertain to the oxidation of the bare substrates for 1h at 304 K.

well as the overall Mg-to-Al ratio of the oxide films, are shown in Figs. 5.4b, 5.4d and 5.4c, respectively. It follows that the overall anion-to-cation ratio of the grown oxide-films is lower than the corresponding ratios of 1 and $^4/_3$ for MgO and $MgAl_2O_4$, respectively (Fig. 5.4a): i.e.

the grown oxide films, on average, possess a non-stoichiometric composition with respect to both MgO and $MgAl_2O_4$.

The overall anion-to-cation (i.e. O/(MgAl)) ratio increases with increasing pO_2 from 0.74±0.02 at $pO_2 = 1\times10^{-6}$ Pa to 0.85±0.02 at $pO_2 = 1\times10^{-4}$ Pa, approximately independent of the bulk Al content of the alloy. This increase of the O/(MgAl)-ratio of the grown oxide films with increasing pO_2 is due to an increase of the overall anion molar density (Fig. 5.4b) in combination with a decrease of the overall cation molar density (Fig. 5.4d) with increasing pO_2. The average anion molar density of the grown oxide films is lower (Fig. 5.4b), whereas the overall molar density of cationic species (i.e. Mg and Al) is higher (Fig. 5.4d), than their corresponding molar densities in either MgO or $MgAl_2O_4$. This suggests that, provided that a crystalline oxide film has formed,[5] the oxide-film defect structure consists of both anion vacancies and cation interstitials. With increasing pO_2 from 10^{-6} to 10^{-4} Pa (independent of the bulk Al content), the overall cation molar density approaches the corresponding value for stoichiometric MgO (Fig. 5.4d). The overall Mg/Al atomic ratio of the grown oxide films in the range of 8-12 (Fig. 5.4c) is much higher than the corresponding atomic Mg/Al-ratio of $^1/_2$ in $MgAl_2O_4$.: i.e. the oxide films are relatively deficient of Al with respect to $MgAl_2O_4$.

Whereas the overall anion-to-cation ratio of the grown oxide films is about independent of the bulk Al content (see above), the relative amount of Al incorporated in the oxide films, as expressed by the overall Mg/Al-ratio of the grown oxide films, does vary with the bulk Al content. For the lowest Al alloying bulk content of 2.63 at.%, the relative Mg/Al-ratio is significantly higher (i.e. Mg/Al-ratio ~ 15) than for the higher Al bulk contents of 5.78 at.% and 7.31 at.% (i.e. Mg/Al-ratio ~ 8) (see Fig. 5.4c).

On the basis of the above results it is concluded that the structure of grown oxide-films resemble that of an Al-doped MgO oxide rather than of a $MgAl_2O_4$ (spinel) oxide with an overall defect structure of anion vacancies and cation interstitials (since the grown oxide-films are, on average, enriched in cationic species and depleted in O).

5.3.4 Oxide-film growth kinetics

The oxide-film growth curves as determined *independently* by AR-XPS [89] and RISE [88] (see also Secs. 5.2.3 and 5.2.4, respectively) for the oxidation of the bare Mg – 7.31 at.% Al substrate for 1 h at 304 K at pO_2 of 5×10^{-5} Pa are shown in Fig. 5.5. Clearly, the values for the

[5] The grown oxide films are assumed to be amorphous with some degree of long range ordering (as for the grown Al-oxide films in Ref. 23).

oxide-film thickness as determined by AR-XPS [89] agree very well with the corresponding thickness values as determined independently by RISE [88].

The oxide-film growth curves, as obtained by RISE [88] for the oxidation of the bare MgAl substrates for 1 h at 304 K at various pO_2 and for low (2.63 at.%) and high (7.31 at.%) bulk Al alloying content are shown in Figs. 5.6a and 5.6b, respectively. Evidently, the *total*

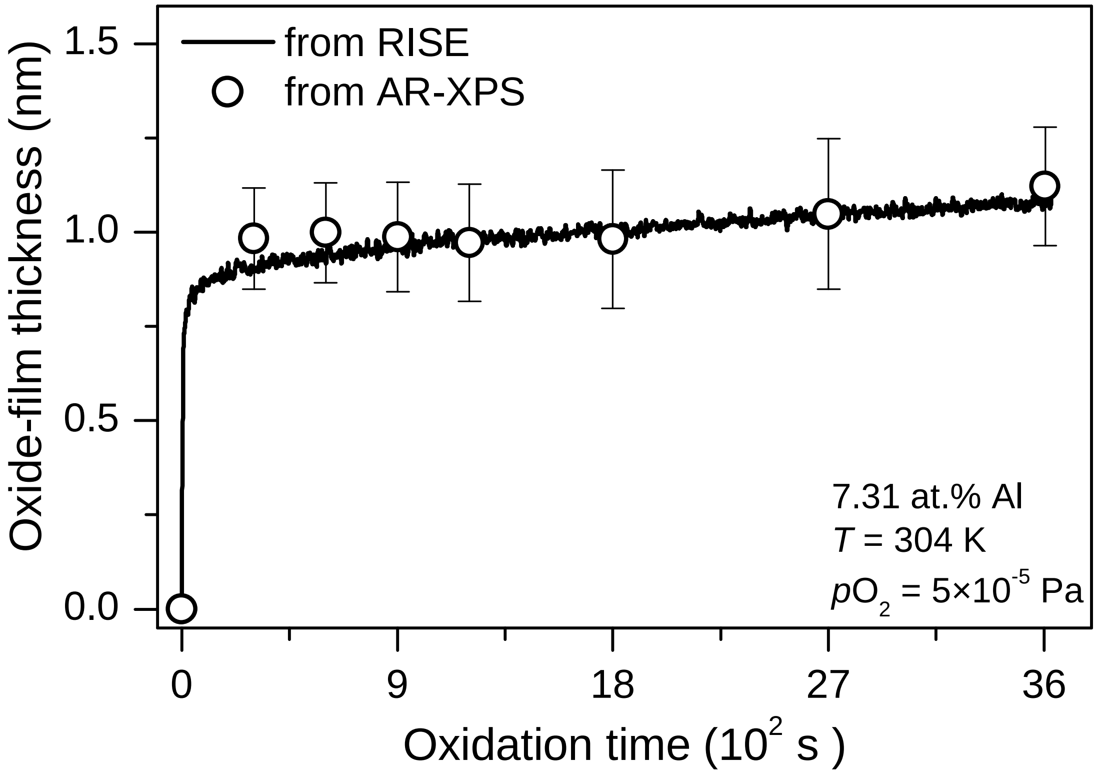

Figure 5.5. Oxide-film thickness as a function of oxidation time, for the oxidation of the bare 7.31 at.% Al alloy substrate at 304 K and pO_2 = 5×10^{-5} Pa. The oxide-film thickness values were determined independently from (*i*) measured Mg 2p –Al 2p and O 1s AR-XPS spectra of the oxidized alloy substrates [89] and (*ii*) measured spectra of the phase and amplitude parameters, $\Delta(\lambda)$ and $\psi(\lambda)$, over the wavelength range of 350-700 nm recorded with ellipsometry (RISE) [88]. The error bars for the AR-XPS thicknesses correspond to the standard deviation of a total of 30 thickness values, obtained by five different methods of calculation using the resolved metallic Mg 2p and Al 2p, oxidic Mg 2p and Al 2p and O 1 s PZL intensities, as resolved from a set of 6 measured AR-XPS spectra of the oxidized alloy (each recorded at a different detection angle set) (see Ref. [89] for details).

oxide-film growth kinetics can be subdivided into two different growth regimes: a short, initial regime of very fast oxide-film growth, which is followed by a second, much slower growth stage of about constant growth rate. The constant growth rate during the second growth stage is approximately independent of the pO_2 in the range of 1×10^{-6} to 5×10^{-5} Pa, but is significantly higher for the highest studied pO_2 of 1×10^{-4} Pa (Fig. 5.5). The length of the initial, very fast growth regime decreases, whereas the value of the total oxide-film thickness

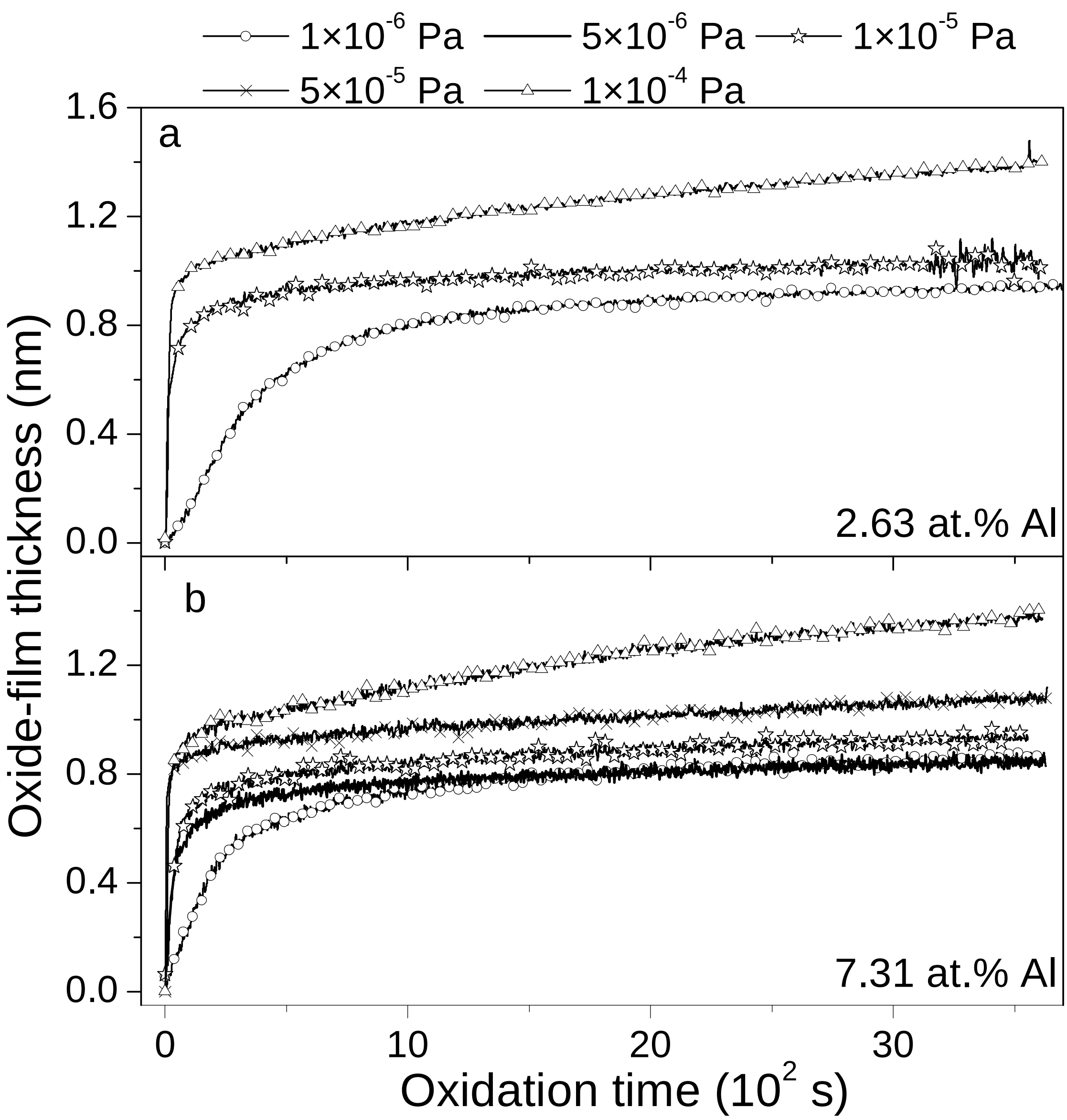

Figure 5.6. Oxide-film growth curves for the oxidation of bare (**a**) Mg – 2.63 at.%Al and (**b**) Mg – 7.31 at.% Al alloy substrates at 304 K at various pO_2 within the range of 10^{-6} – 10^{-4} Pa. The oxide-film thickness-time curves were determined from the measured spectra of the phase and amplitude parameters, $\Delta(\lambda)$ and $\psi(\lambda)$, over the wavelength range of 350 – 700 nm, as recorded with real-time, in situ spectroscopic ellipsometry.

attained during the slow oxidation regime after 1 h of oxidation (designated here as the near-limiting oxide-film thickness) increases, with increasing pO_2 (see Figs. 5.6 and 5.7). For the oxidations in the pO_2 range of 1×10^{-6} - 1×10^{-4} Pa, an oxide-film thickness in the range of about 0.6 - 1.0 nm (increasing with increasing pO_2; see Fig. 5.6) is reached at the onset of the transition to the second, slow oxidation stage. Near-limiting oxide-film thicknesses in the range of about 0.8 to 1.4 nm are observed during the second, slow oxidation stage after 1 h of oxidation (Figs. 5.6 and 5.7); the thickness increases significantly with pO_2 in the range of 1×10^{-6} - 1×10^{-4} Pa, but only slightly increases with bulk Al alloying content in the range of 2.63 at.% to 7.31 at.% (see Fig. 5.7).

The near-limiting thickness values in the range of 0.8 to 1.0, as obtained for $pO_2 \leq 1\times10^{-5}$ Pa (Fig. 5.6), are about 0.2 to 0.4 nm lower than the corresponding near-limiting thickness value reported for the oxidation of a bare polycrystalline Mg substrate in the pO_2 range of 1×10^{-8} - 1.3×10^{-5} Pa [78], and are considerably higher than the near-limiting thickness of ~0.5 nm reported for the oxidation of bare Al substrates at 373 K and a relatively high pO_2 of 1.3×10^{-4} Pa [19].

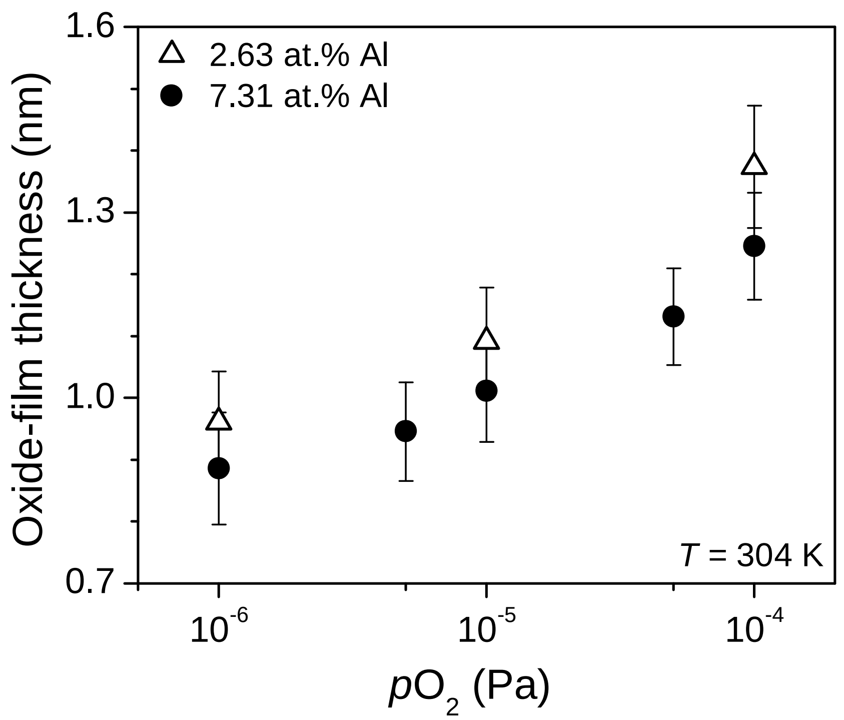

Figure 5.7. Average, total oxide-film thickness as a function of the pO_2 as reached after 1h of oxidation of a bare Mg – 2.63 at.% Al and Mg – 7.31 at.% Al alloy substrate at 304 K. The oxide-film thicknesses were determined by the quantitative analysis of sets of measured Mg 2p –Al 2p and O 1s AR-XPS spectra as recorded (at various detection angle sets) from the oxidized alloy substrates [89].

5.4 Discussion

5.4.1 Compositional changes induced by sputter cleaning

To explain the observed microstructure of the initial oxide film grown on *bare* Mg-based MgAl alloys by thermal oxidation (see Sec. 5.3), it is essential to know and understand the compositional changes induced in the surface adjacent regions of the Mg-based alloys by the sputter-cleaning treatment prior to each oxidation step (to remove the native oxide; see Sec. 5.2.2). A model, based on the combined processes of preferential sputtering and bombardment enhanced Gibbsian segregation has been developed by our group [62] for the calculation of

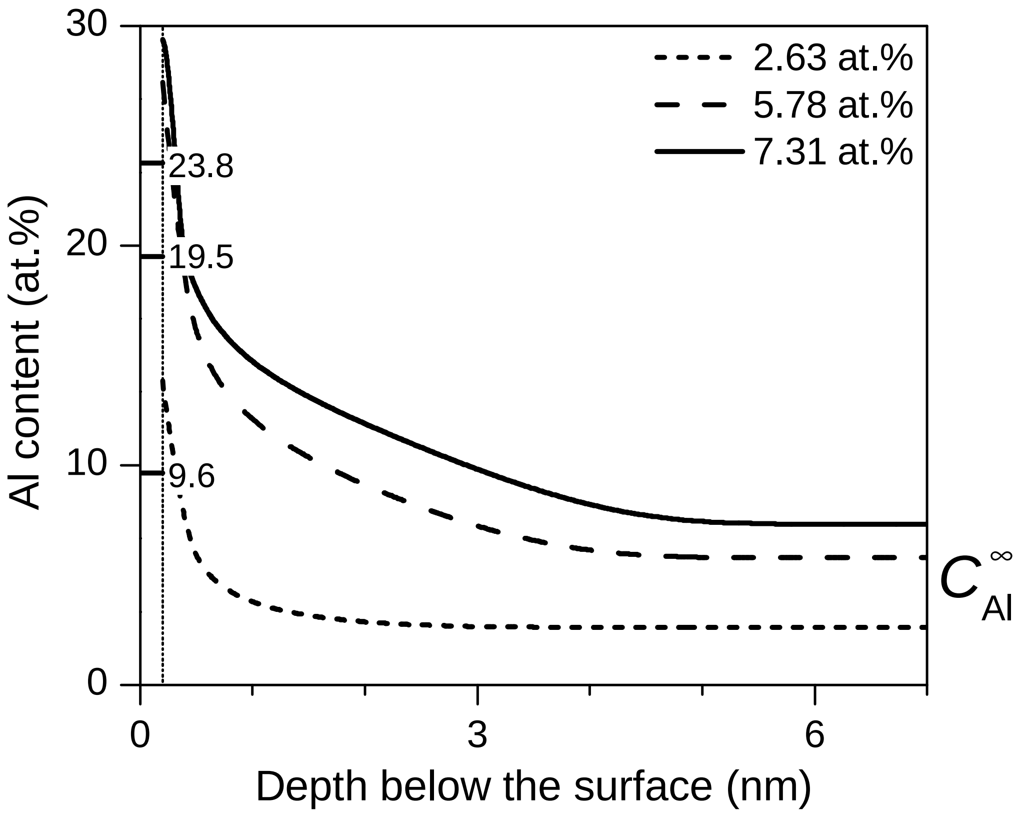

Figure 5.8. Calculated steady state Al concentration-depth profiles set up in the surface adjacent region of a Mg-based MgAl alloy under continuous bombardment with 1 keV Ar^+ ions for various bulk Al alloying contents (C_{Al}^{∞}). Note that a distinct drop in the degree of Al enrichment occurs at the outer surface: the composition at the very surface is governed only by preferential sputtering (leading to an Al content *at* the bombarded alloy surface of 9.6 at.%, 19.5 at.% and 23.8 at.% for the 2.63 at.% Al, 5.78 at.% Al and 7.31 at.% Al substrates, respectively). The composition at larger depths is determined by the competing processes of preferential sputtering of Mg at the outer surface and bombardment-enhanced Gibbsian segregation of Mg from the interior of the alloy to the outer surface. For details, see Ref. [62].

the steady state Al concentration-depth profile set up in the alloy subsurface region under continuous ion (Ar^+) bombardment as a function of the bulk (Al) content and the incident ion (Ar^+) energy. Thus, the calculated Al concentration-depth profiles set up in the MgAl alloy subsurface region after continuous bombardment with 1 keV Ar^+ ions (as employed in the present investigation; see Sec. 5.2.2) for various bulk Al alloying contents are shown in Fig. 5.8. As discussed in Ref. [62], due to the preferential sputtering (i.e. removal) of Mg from the bombarded alloy surface in combination with the simultaneous bombardment-enhanced Gibbsian segregation of Mg from the interior of the alloy to the free surface, a strong Al-enrichment develops in the alloy subsurface region upon sputter-cleaning (Fig. 5.8). Indeed, results obtained in this work confirm the enrichment of Al in the alloy adjacent to the surface for the bare alloy substrates: see the relatively smaller effective depth for Al (as compared to Mg) in the alloy subsurface region after sputter-cleaning (Fig. 5.3 in Sec. 5.3.2).

The degree of Al enrichment in the alloy subsurface region rapidly falls off with increasing depth below the alloy surface (Fig. 5.8). The bombarded alloy attains its bulk composition in the depth range of 4-6 nm below the specimen surface (the depth at which the bulk composition is reached increases with increasing bulk Al alloying content; see Fig. 5.8). Since preferential sputtering of Mg from the outer surface layer is the much faster process as compared to bombardment-enhanced Gibbsian segregation, the composition *at* the outer surface is only determined by preferential sputtering. Consequently, a lower degree of Al enrichment occurs *at* the outer surface (i.e. the first atom layer; see Fig. 5.8), as was confirmed experimentally by ion scattering spectroscopy [62].

5.4.2 Oxide-film growth mechanism

Ellipsometric analysis of the measured changes in the ellipsometric parameters Δ and ψ as a function of oxidation time revealed that the onset of oxidation of the bare alloy substrates is associated with the initial incorporation of oxygen into the alloy surface followed by the subsequent nucleation and growth of 3-dimensional oxide islands on the alloy surface ([88]; see also Ref. [19]). Because the rates of oxygen chemisorption and oxide nucleation at the onset of oxidation decrease with decreasing pO_2, the competing process of oxygen incorporation is promoted at a lower pO_2 [88]. Upon formation of a closed oxide-film, the transition to the second, slow oxidation stage occurs [88], which stage is reached after a shorter oxidation time for oxidation at a higher pO_2 (see Sec. 5.3.4 and Fig. 5.6).

For the oxidation of the bare MgAl substrates, the total energy gain of the reacting system per mole O_2(g) has to be considered [90]. Because the Gibbs free energy of formation per mole reacting O_2(g) is lower for crystalline MgO (2×-569 = -1138 kJ kJ/mole O_2 [91]) than for amorphous Al_2O_3 (2/3 × -1531 = -1021 kJ/mole O_2 [90]), it is suggested that preferential oxidation of Mg occurs. At the initial stages of oxygen incorporation and oxide nucleation (with relatively very high oxidation rate), the rate of uptake of Mg by the developing oxide film will exceed the rate of supply of Mg from the interior of the alloy towards the reacting alloy/oxide/oxygen interface. Since a strong Al enrichment already exists in the surface region of the bare alloy substrate (as compared to the bulk) at the onset of oxidation (see Sec. 5.4.1 and Fig. 5.8), it follows that the alloy surface region is almost instantaneously depleted of Mg upon exposure to oxygen gas.[6] Hence, a relatively Al-rich oxide is formed at the onset of oxidation (i.e. Al-rich as compared to the oxide formed during the second, slow growth stage; see below and Sec. 5.4.3), as confirmed by RISE in Ref. [88]. Since the degree of Al enrichment in the subsurface region of the sputter-cleaned alloy substrate is much less for the alloy with the lowest bulk Al content of 2.63 at.% (see Sec. 5.3.3 and Fig. 5.8), it follows that the relative Al-content of the resulting oxide film grown on the Mg – 2.63 at.% Al substrate is also strongly reduced as compared to the oxide films grown on the other alloys, which has been confirmed by AR-XPS (see Fig. 5.4c). As a direct consequence of the relatively low Al content of the oxide grown initially on the Mg – 2.63 at.% Al substrate, the corresponding near-limiting oxide-film thickness as attained after 1 h of oxidation, is practically equal to the corresponding near-limiting thickness value as reported for pure Mg (see Sec. 5.3.4 and Fig. 5.7).

It can be concluded that the Al content of the initial oxide film formed on Mg-based MgAl substrate at room temperature is dictated by the compositional changes in the alloy subsurface region induced by the sputter-cleaning treatment prior to oxidation and not by the bulk Al alloying content.

As soon as the entire alloy substrate area is covered with at least one oxide monolayer (= ML with one oxide ML ~ 0.2 nm [90]), the surface plasmon (SP) structure associated with the Mg 2p metallic main peak should have disappeared in the measured XPS spectrum of the

[6] Even for the onset of oxidation of ternary alloys at high temperatures (i.e. T > 1300 K; for which the rate of supply of the preferentially oxidized alloy constituent from the alloy's interior is much faster), such an approximately instantaneous depletion of the preferentially oxidized alloy constituent at the onset of oxidation has been theoretically predicted [9] and experimentally observed [10].

oxidized metal [16, 29].[7] Indeed, even for the shortest oxidation time studied here (300 s), the SP peak associated with the metallic Mg 2p main peak has disappeared (cf. Fig. 5.1a). Growth of the closed oxide film is then expected to proceed by the preferential oxidation of Mg (see above). Indeed, as follows from the larger effective depth of the oxidic Al species in the developing oxide film (as compared to that of the oxidic Mg species; see Fig. 5.3), continued oxide-film growth after the formation of a closed oxide film (see above) is realized by the development of an *overgrowth* of a Mg-rich oxide, by the preferential uptake and subsequent outward diffusion of Mg from the alloy/oxide interface towards the oxide surface (see also Sec. 5.4.3). Note that the value determined for the effective depth of Al in the developing oxide film in this stage approximately equals that of the total near-limiting oxide-film thickness, suggesting that the Al-enrichment in the oxide film is concentrated *at* the alloy/oxide interface (compare Fig. 5.3a with Figs. 5.6 and 5.7).

As indicated by ellipsometric investigation [88], after formation of a closed oxide film, the amount of supply of Mg from the interior of the alloy towards the alloy/oxide interface is promoted by the oxidation-induced chemical "segregation" of Mg. The extent of Mg depletion in the alloy subsurface region is governed by the relative rates of the concurrent processes of transport of Mg through the growing oxide film and the oxidation-induced chemical "segregation" of Mg in the substrate. The process of oxidation-induced chemical segregation of Mg becomes more important at elevated pO_2 (and thus at the highest pO_2 = 1×10^{-4} Pa studied in this work) [88].[8]

At the low temperatures considered here (i.e. room temperature), thermally activated diffusion of Mg through the developing oxide film under influence of the (electro)chemical potential (i.e. concentration) gradients is negligibly small [7, 11, 13, 15, 19, 87]. Instead, subsequent growth (during the second oxidation stage) is realized by coupled currents of cations and electrons through the developing oxide-film under influence of the electric field

---

[7] As soon as the alloy becomes covered with an oxide monolayer, the 'free' electrons in the surface region of the metallic alloy become localized as a result of the chemical bonding to oxygen. Consequently, the probability for plasmon excitations in the surface region of the alloy (i.e. at the alloy/oxide interface) becomes strongly reduced (cf. Refs. 16, 29).

[8] AES investigations on the thermal oxidation of ~ 1 ML thick Ag film on top of a Cu{100} substrate and of polycrystalline Cu(Ag) alloy substrates [92] also revealed a strong (oxidation-induced) chemical segregation of the less noble element (i.e. Cu) to the surface and subsequent overgrowth of Cu_2O (i.e. the oxide phase with the most negative free Gibbs energy of oxide formation per mole O_2) at an elevated pO_2 of 200 Pa.

due to the kinetic potential set-up by chemisorbed oxygen species at the oxide surface [7, 11, 13, 15, 19, 87]. If the intrinsic electron transport rate by tunneling is much faster than the intrinsic cationic transport rate, the kinetic potential will approach that of the so-called Mott potential (cf. Refs. [7, 15]).

5.4.3 The origin of the O 1s HBE component

Two different chemical states have been identified for the oxygen ions in the developing oxide film, corresponding to the resolved LBE and HBE O 1s component (Figs. 5.2 and 5.3b). Similar observations have been reported for the thermal oxidation of pure magnesium [78, 93-96]. The LBE peak at around 531.3 eV is generally attributed to lattice oxygen anions (O^{2-}) in the 'bulk' oxide film [93-96], in agreement with the present interpretation on the basis of the reconstructed depth plot (Fig. 5.3). The origin of the O 1s HBE component has been discussed controversially: it has been attributed to hydroxide species (i.e. a hydroxylated oxide surface) [78, 93] or to atoms acting as precursors for oxide formation [96].

To clarify the origin of the HBE component in the present study, the oxide film formed on a bare Mg – 2.63 at.% Al substrate by thermal oxidation at 304 K for 1 h at 1×10^{-4} Pa was subjected to a post annealing treatment for 0.5 h at a temperature of 450 K under UHV conditions. After the annealing treatment, the relative contribution of the HBE component (as compared to the LBE component) had decreased, whereas the total O 1s PZL intensity had remained constant (Fig. 5.9a). Apparently, upon annealing of the grown oxide film above its growth temperature, part of the surface-adjacent region of the grown oxide-film, associated with the O 1s HBE component, is transformed into 'bulk' oxide (resulting in a relative increase of the O 1s LBE component). Note that any significant desorption of chemisorption species or a dehydroxylation of the oxide-film surface upon annealing is expected to result in a decrease of the total O 1s PZL intensity, in contrast with what was observed here (see Fig. 5.9a). In addition, the PZL intensity of the oxidic Mg 2p peak (and too a much lesser extent that of the oxidic Al 2p peak; see Fig. 5.9b) had increased upon annealing, in apparently in parallel with an increase of the oxide-film thickness upon annealing, as determined using AR-XPS (see Fig. 5.9c). The increase of the Mg content of the oxide film in combination with transformation of part of the O 1s HBE component into the O 1s LBE component upon annealing, indicate that outward diffusion of Mg from the alloy/oxide interface towards the oxide surface to react with the HBE oxygen species had occurred (in association with an increase of the oxide-film thickness, as observed by AR-XPS [89]). It is therefore concluded that the (initial) O 1s HBE component is associated with a highly defective oxide structure in the oxide-film surface region (and thus cannot be ascribed to hydroxide or hydroxyl oxide species).

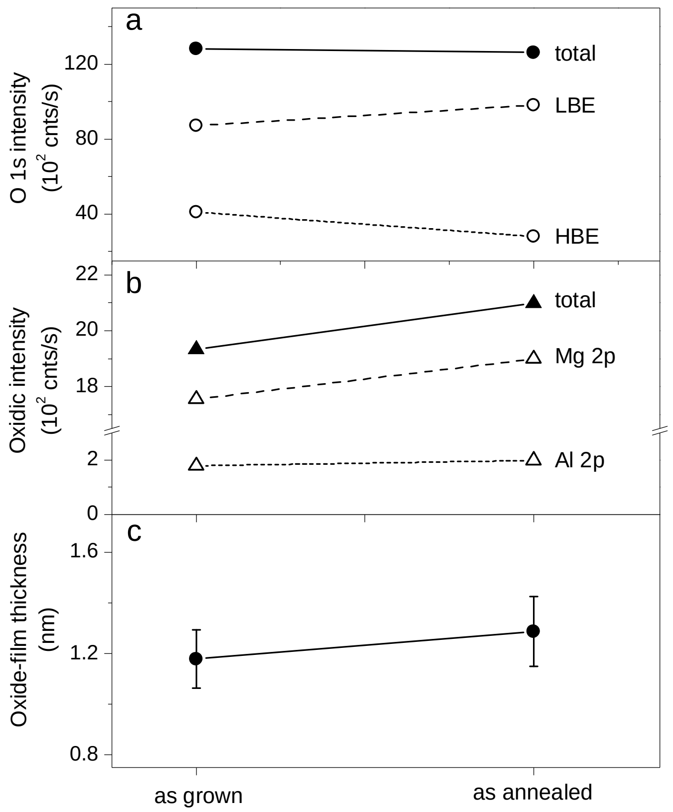

Figure 5.9. (**a**) O 1s LBE, O 1s HBE and total O 1s PZL photoelectron intensity as resolved from the measured AR-XPS spectra recorded from the oxidized Mg – 2.63 at.% Al alloy (for 1 h at 304 K and $pO_2 = 1\times10^{-4}$ Pa; designated as 'as grown') and after annealing of the grown oxide film in UHV at 450 K for 1800 s (designated as 'as annealed'). (b) Corresponding oxidic Mg 2p, oxidic Al 2p and total oxidic (i.e. Mg 2p plus Al 2p) PZL intensities before and after the annealing. (c) Corresponding average, total oxide-film thickness as determined from the resolved metallic and oxidic Mg 2p and Al 2p and O 1s PZL intensities before and after the annealing [89]. All PZL intensities shown correspond to the total PZL intensity after summing over the entire angle detection range from $(\alpha,\phi) = (23^\circ, 43^\circ)$ to $(\alpha,\phi) = (83^\circ, 94^\circ)$ (see Sec. 5.2.3).

5.5 Conclusions

The measured Mg 2p and Al 2p (AR-)XPS spectra of the oxidized Mg-based MgAl alloys can each be accurately fitted with one metallic and one oxidic component. Two different components are identified in the O 1s (AR-)XPS spectra (designated as the lower-binding energy (LBE) and higher-binding-energy (HBE) component). The XPS analysis shows that oxide-film microstructure resembles that of an Al-doped MgO-type of oxide. Al-enrichments are present in the oxide film and in the alloy subsurface region adjacent to the alloy/oxide interface. The oxide films are non-stoichiometric (with respect to MgO) and possess oxygen deficiency and slight overall cation enrichment. With increasing pO_2, the overall anion molar density increases and the overall cation molar density decreases (and approaches the value for stoichiometric MgO).

The resolved LBE O 1s species are attributed to oxygen anions in the interior of the oxide film, whereas the HBE O 1s component originates from a defect oxide structure in the surface-adjacent region of the oxide film. After the formation of a 'closed' oxide film on the bare alloy surface, this defect oxide structure acts as a precursor for continued oxide-film growth by the outward diffusion of Mg cations under the influence of a surface-charge field.

Two different growth stages were recognized for the oxidation of the bare alloy substrates (at 304 K). The short, initial growth regime is associated with oxygen incorporation in the alloy surface and subsequent oxide nucleation and growth, forming a relatively Al-rich, closed oxide film on the alloy surface. Subsequent growth is realized by the preferential oxidation of Mg from the alloy subsurface region and overgrowth of a Mg-rich oxide by the electric-field controlled, outward migration of Mg cations through the developing oxide film The extent of depletion of Mg in the alloy subsurface region during this slow, but continuing, growth stage is governed by the competing processes of preferential oxidation of Mg and oxidation-induced, chemical segregation of Mg from the interior of the alloy towards the alloy/oxide interface.

The Al-content incorporated in the grown oxide films, as well as the corresponding (near-) limiting oxide-film thickness reached at the end of the slow growth stage, are governed by the degree of Al enrichment in the alloy subsurface region prior to oxidation as induced by the sputter-cleaning treatment; i.e. the Al content and the near-limiting thickness of the grown oxide film only marginally depend on the bulk Al content of the alloy.

Acknowledgements

We are grateful to Dipl.–Ing. F. Reichel for assistance provided with the presented model calculations of the Al concentration-depth profiles for the sputter-cleaned alloys.

Chapter 6

Summary: On the initial oxidation of MgAl alloys

Fundamental and comprehensive understanding of the oxidation behaviour of bare metal and alloy surfaces is of great importance for numerous application areas, such as heterogeneous catalysis, microelectronics, surface coatings and gas sensors. For instance, the recent desire to tune the physical and chemical properties (e.g. corrosion resistance, electrical and thermal conductivity, adhesion or catalytic activity) of very thin (< 10 nm) oxide-films grown on bare alloy surfaces by tailoring both the alloy substrate and oxide-film microstructure has increased the interest for the initial stages of thermal oxidation of binary alloy surfaces at low temperatures.

This study addresses the initial stages of the thermal oxidation of Mg-based MgAl alloys at room temperature. Mg-based alloys are an attractive candidate for technological applications where light weight in combination with improved recyclability is required (e.g. the automobile, computer and space industry). Although the addition of Al to the Mg base metal is known to improve its castability, hardness and oxidation resistance, the underlying mechanisms and limits of these improvements are still poorly understood. Further, a fundamental investigation of the low-temperature oxidation of Mg-based MgAl alloys represents a scientific challenge, because the chemical and physical nature of the two alloy constituents (i.e. Mg and Al) are very alike (in contrast to binary alloys like Cu-Au, Ag-Cu or Pt-Al, which consist of one relatively nobler alloy constituent).

The initial stages of the thermal oxidation of bare, polycrystalline Mg-based MgAl alloys has been investigated by a combined approach of angle-resolved X-ray photoelectron spectroscopy (AR-XPS) and real-time, in-situ, spectroscopic ellipsometry (RISE). All oxidation experiments have been performed under controlled conditions in a UHV reaction chamber (RC; base pressure < 2.5×10^{-8} Pa), which is equipped with (*i*) a unit for controlled admission of pure O_2 gas, (*ii*) a quadrupole mass spectrometer to monitor the residual gas content and control the partial oxygen pressure (pO_2) during growth, and (*iii*) an in-situ spectroscopic ellipsometer for real-time analysis of the oxide-film growth kinetics. This UHV RC is directly coupled to the UHV chamber (base pressure < 5×10^{-8} Pa) for AR-XPS analysis of the grown oxide films.

Due to its high reactivity with the ambient, the MgAl sample surface is always covered with a several nanometers thick, native oxide film prior to its introduction into the UHV system. To remove this native oxide and other contaminants from the alloy surface, prior to each oxidation experiment, the MgAl substrates were sputter-cleaned by ion-bombardment with a focused 1 kV Ar^+ beam rastering the entire sample surface area. The alloy substrates as received after this sputter-cleaning treatment are further designated as *bare* substrates. Subsequently, bare MgAl substrates of various bulk Al alloying contents (i.e. 2.63 at.%, 5,78 at.%, 7.31 at.%) were oxidized by exposure to pure O_2 gas for various oxidation times (from 300 s up to 1 h) at T = 304 K (i.e. room temperature) and various partial oxygen pressures (pO_2) within the range of 10^{-6} – 10^{-4} Pa. RISE was employed to determine the oxide-film growth kinetics and the evolution of the oxide-film constitution (as evidenced from the variation of the optical constants of the growing oxide film). The oxide-film microstructure in terms of thickness, morphology, constitution (i.e. the depth distribution of different chemical species), composition and defect structure of the grown oxide films, has been determined using AR-XPS.

The state-of-the-art instrument for AR-XPS analysis employed in the present investigation has the capability of detecting the emitted photoelectrons simultaneously over a wide angular range without tilting of the sample (so-called parallel data acquisition mode), which greatly speeds up the recording of a series of AR-XPS spectra and ensures a constant analyzed area and position. In contrast to a conventional XPS setup, the angle ϕ between the incident X-rays and detected photoelectrons is not a constant, but varies with the detection angle α (with respect to the sample surface normal) for the AR-XPS spectra recorded in the parallel data acquisition mode. Consequently, as demonstrated by a fundamental investigation in the present work (Chapter 2 of this thesis), accurate quantitative analysis of these AR-XPS spectra requires knowledge of the anisotropy of the photoionization cross-section for each core-level photoelectron line studied, as well as of the effect of elastic scattering of the detected photoelectrons in the solid. As demonstrated for the quantitative analysis of the Al 2p and O 1s photoelectron lines recorded from an α-Al_2O_3 reference, ignoring the effects of the anisotropy of photoionization cross-section and elastic scattering can introduce errors as high as 16% in the compositional analysis of AR-XPS spectra recorded from binary solids in parallel data acquisition mode. Cumbersome corrections for the effects of the anisotropies of the photoionization cross-sections and elastic scattering can be avoided (e.g. for the quantitative analysis of solids and thin film structures of unknown composition and/or thickness) by adopting values for the relative sensitivity factors as a function of the angles α and ϕ determined experimentally from a reference solid of known composition (Chapter 2 of this thesis).

Now, to accurately determine the thickness, composition and constitution (i.e. the depth distribution of the resolved chemical species) of the oxide films grown on the bare MgAl substrates as a function of the oxidation conditions by AR-XPS, a total of six different primary zero-loss (PZL) photoelectron intensities[9] need to be considered in the quantification: i.e. the PZL intensities of the metallic and oxidic Mg 2p peaks (Fig. 6.1a), the PZL intensities of the metallic and oxidic Al 2p peaks (Fig. 6.1b) and the PZL intensities of the resolved O 1s main peaks (Fig. 6.1c). Further, in the quantification, pre-existing knowledge and/or reasonable estimates of the intrinsic plasmon excitation probabilities for the Mg 2p and Al 2p photoemission process in the alloy, as well as of the oxide-film density and/or the effective attenuation lengths of the detected photoelectrons in the oxide film are required.

Therefore, a novel procedure has been developed for the quantitative analysis of the measured AR-XPS spectra of the bare and oxidized MgAl substrates, which provides a framework for accurate quantitative analysis of AR-XPS spectra recorded from thin oxide films as grown on their alloy substrates by thermal or plasma oxidation (Chapter 3 of this thesis). To this end, first a procedure for spectral evaluation was developed to retrieve the total metallic Mg 2p and Al 2p, oxidic Mg 2p and Al 2p and oxygen O 1s PZL intensitiesfrom the measured XPS spectra of the bare and oxidized MgAl substrates (cf. Fig. 6.1). Next, the expressions and associated calculation schemes for the determination of the average oxide-film thickness, the overall composition and the effective depth distribution of the resolved chemical species were deduced from the principle equations for the corresponding Mg 2p, Al 2p and O 1s PZL photoelectron intensities. It follows that the thus obtained values for the thickness of the grown oxide films as determined by AR-XPS agree well with the corresponding oxide-film growth curves as obtained by RISE (cf. Fig. 6.2).

For the in-situ investigation of the oxide-film growth kinetics by RISE, the changes in the ellipsometric amplitude ratio and phase shift dependent parameters ψ and Δ as a function of oxidation time have been measured simultaneously for various wavelengths, λ, of the incident polarized light source over the wavelength range from 350 to 700 nm (cf. Fig. 6.3). The tangent of the angle ψ corresponds to the ratio of the magnitudes of the total reflection

[9] The total primary zero-loss photoelectron intensity of a given core-electron level comprises all detected photoelectrons that have been left unaffected after their emission from the given core-level in the solid (i.e. all recorded unscattered or elastically scattered photoelectrons).

coefficients (i.e. the relative amplitude of the reflected wave with respect to that of the incident wave) for the components of the electric field vector of the polarized light vibrating in the plane of incidence (p-wave) and perpendicular to it (s-wave), respectively. The angle Δ is the difference between the phase shifts experienced upon reflection by the p- and s-waves, respectively.

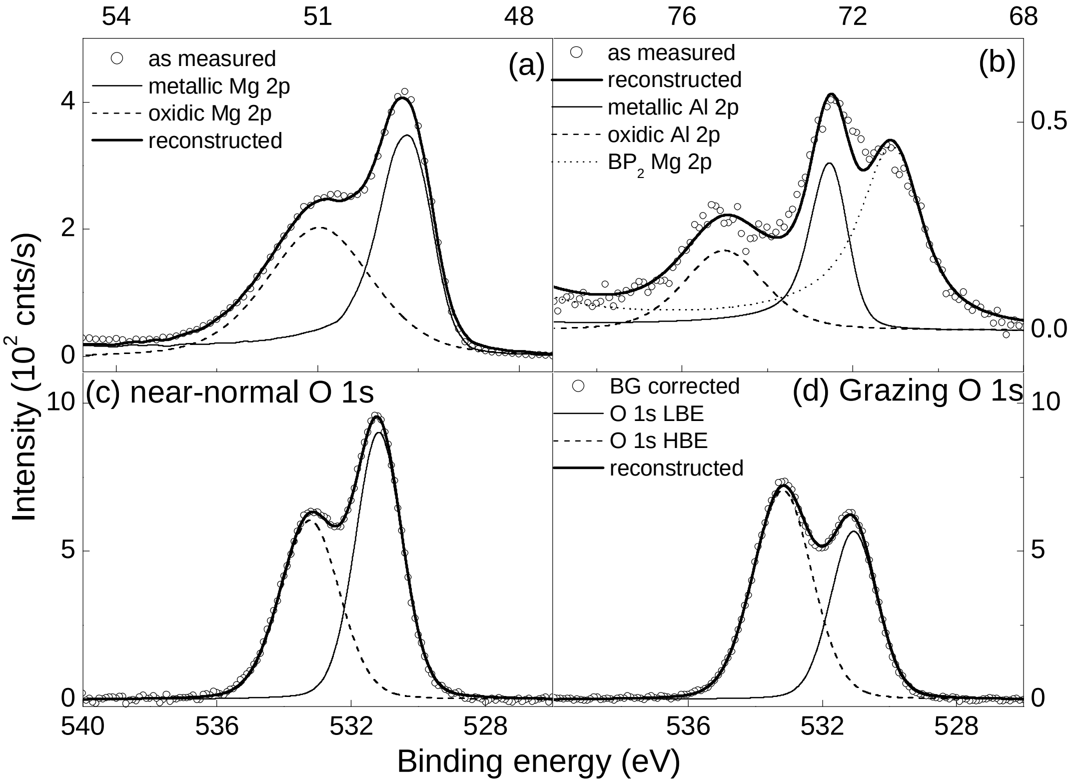

Figure 6.1. (**a**) As-measured and reconstructed Mg 2p spectra of the oxidized Mg - 2.63 at.% Al substrate (1 h at 304 K and pO_2 = 1×10^{-4} Pa) as recorded at a detection angle set of $(\alpha,\phi)=(34.3^o,51.7^o)$. The reconstructed Mg 2p spectrum is constituted of a single metallic and a single oxidic Mg 2p main peak. (**b**) Corresponding as-measured and reconstructed Al 2p spectra of the oxidized alloy. Besides a single metallic and a single oxidic Al 2p main peak, the total reconstructed Al 2p spectrum also contains a contribution due to the second bulk plasmon peak (BP_2) of the metallic Mg 2p main peak in (a). Corresponding background-corrected and reconstructed O 1s spectra of the oxidized alloy as recorded at (**c**) near-normal and (**d**) grazing detection angle-sets of $(\alpha,\phi)=(34.3^o,51.7^o)$ and $(\alpha,\phi)=(71.8^o,83.8^o)$, respectively. The reconstructed O 1s spectrum is constituted of two components at the lower (LBE) and higher binding energy (HBE) side of the peak envelop. The relative contributions of the LBE and HBE component predominate at a near-normal and grazing detection angle, respectively.

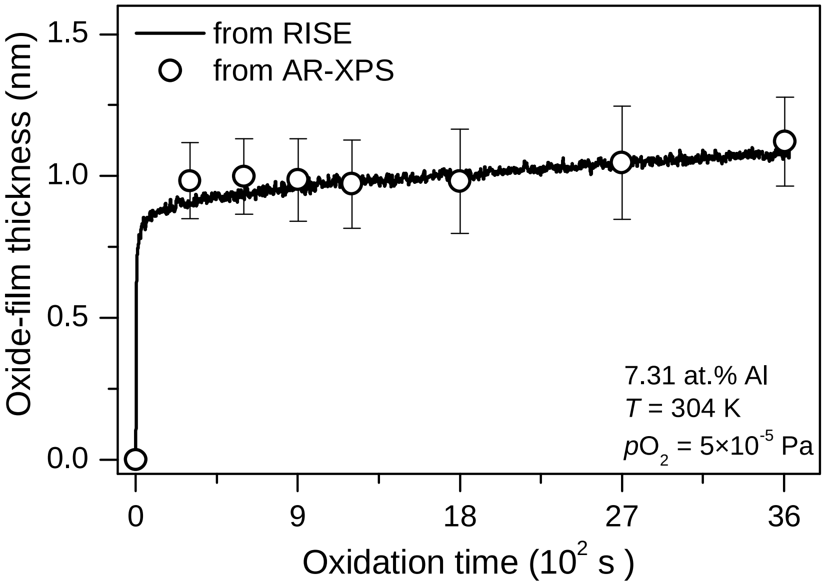

Figure 6.2. Total oxide-film thickness as a function of oxidation time, for the oxidation of the bare Mg – 7.31 at.% Al substrate at 304 K and pO_2 = 5 x 10^{-5} Pa. The average, total oxide-film thickness values were determined independently from (*i*) the measured Mg 2p –Al 2p and O 1s photoelectron spectra of the oxidized alloy substrates as recorded using AR-XPS (cf. Fig. 6.1) and (*ii*) the measured spectra of the phase and amplitude parameters, Δ and ψ, over the wavelength range of 350-700 nm as recorded with real-time, in-situ ellipsometry (cf. Fig. 6.3).

Various models have been developed to describe the measured time dependence of the spectra of $\Delta(\lambda)$ and $\psi(\lambda)$ for the initial and subsequent stages of oxidation. It followed that the measured changes in $\Delta(\lambda)$ and $\psi(\lambda)$ as a function of time could be accurately fitted by adopting a compositionally inhomogeneous, Al-doped MgO oxide film developing on the MgAl alloy surface (Chapter 4 of this thesis and Fig. 6.3). The optical constants of the MgAl substrates (as a function of λ) were determined from the in-situ measurement of the bare alloy substrate prior to each oxidation. The optical constants for Al-doped MgO were estimated from the optical constants of pure MgO and Al metal using the effective medium approximation, while adopting the Maxwell-Garnett formulation and defining MgO as the host matrix. To describe an inhomogeneous depth distribution of Al within this Al-doped MgO layer (i.e. Al is mainly located in the oxide film adjacent to the alloy/oxide interface; see below), a so-called 3-node graded EMA layer approach was used by linearly grading the EMA fraction of Al from 0.75 to zero in between the bottom and some variable, intermediate position within the MgO layer, while fixing the EMA fraction of Al to zero in the remaining top (i.e. surface-adjacent) part of the MgO layer.

Application of such modelling to the measured spectra of $\psi(\lambda)$ and $\Delta(\lambda)$ as a function of oxidation time for the thermal oxidation of bare, Mg-based MgAl substrates at 304 K in the

pO_2 range of 10^{-6} to 10^{-4} Pa then yields a linear relationship between the change in Δ (i.e. δΔ) and the change in oxide-film thickness for thicknesses up to about 3 nm. The thus obtained oxide-film thicknesses agree very well with the corresponding thickness values as determined independently by AR-XPS analysis (cf. Fig. 6.2). A corresponding linear relationship between δψ and the oxide film thickness is not evident from the present study, indicating that, to a first order, the ellipsometric parameter ψ is insensitive to the presence of a transparent thin-film phase between the ambient and substrate media. Instead, the initial drop and subsequent steep increase of ψ during the initial, fast oxidation stage (cf. Figs. 6.3a, c) is governed by the concurrent processes of oxygen incorporation in the alloy surface, and nucleation and growth of Al-doped MgO islands on the bare MgAl surface. Upon formation of a closed oxide-film

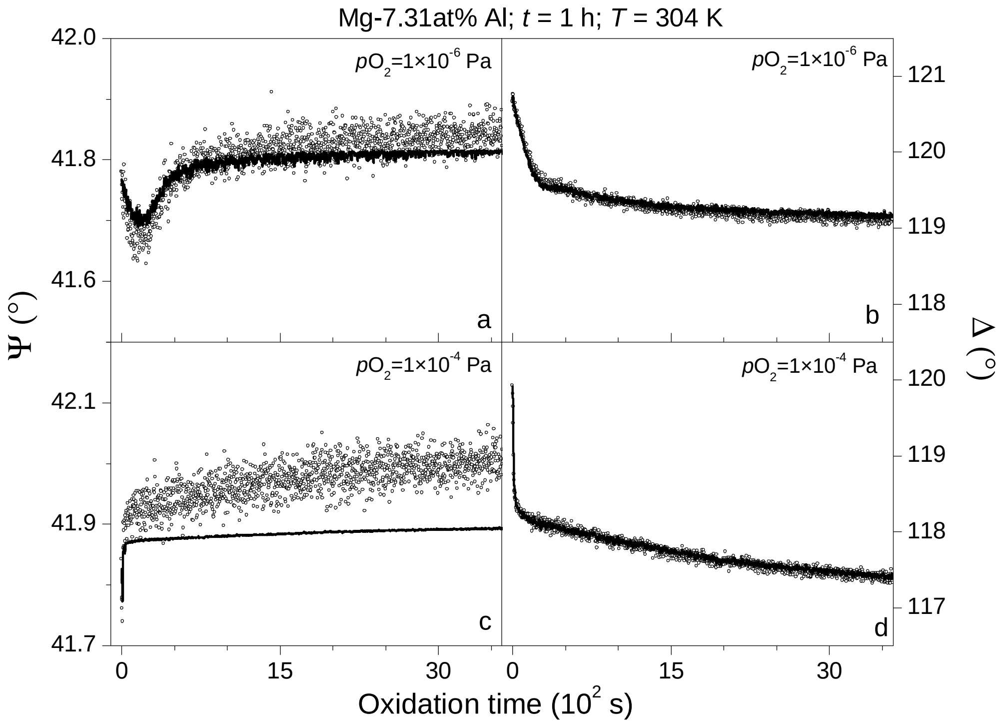

Figure 6.3. The measured (*markers*) and fitted (*lines*) values of the ellipsometric phase and amplitude parameters, Δ and ψ, as a function of oxidation time for a single wavelength of λ = 525 nm. The measured data pertains to the oxidation of the bare Mg – 7.31at.% Al substrate at 304 K for 1 h at a low (1×10^{-6} Pa) and high pO_2 (1×10^{-4} Pa), respectively. The measured changes in Δ(λ) and ψ(λ) as a function of time could be accurately fitted by adopting a compositionally inhomogeneous, Al-doped MgO oxide film developing on the MgAl alloy surface (Chapter 4 of this thesis)

(covering the entire alloy surface) during the slow oxidation stage, the gradual increase in ψ at high pO_2 (cf. Fig. 6.3c) is mainly governed by compositional changes in the MgAl subsurface region due to the competing processes of (oxidation-induced) chemical segregation of Mg from the interior of the alloy to the alloy/oxide interface and the overgrowth of a Mg-rich oxide by the preferential oxidation of Mg.

Application of the aforementioned techniques, and employing the appropriate procedures for the quantification, led to the following results for the initial stages of the thermal oxidation of bare, polycrystalline MgAl substrates of various bulk Al alloying contents (i.e. 2.63 at.%, 5,78 at.%, 7.31 at.%) at T = 304 K in the pO_2 range of 10^{-6} – 10^{-4} Pa (Chapter 5 of this thesis).

Due to the concurrent processes of preferential sputtering (i.e. removal) of Mg from the ion-bombarded alloy surface and bombardment-enhanced Gibbsian segregation of Mg from the interior of the alloy to the ion-bombarded surface, a strong Al-enrichment develops in the alloy subsurface region upon sputter-cleaning. Consequently, at the onset of each oxidation, the Al content in the alloy subsurface by far exceeds the bulk Al content of alloy. The degree of Al enrichment in the alloy subsurface region rapidly falls off with increasing depths below the alloy surface and approaches the bulk composition in the depth range of 4-6 nm below the sample surface. The depth at which the bulk composition is reached decreases with decreasing bulk Al content in the alloy.

Two different growth regimes have been recognised for the oxidation of the bare MgAl substrates: a short, initial regime of very fast oxide-film growth, which is followed by a much slower, but continuing, growth stage. The very onset of oxidation of the bare alloy substrates proceeds with the initial incorporation of oxygen into the alloy surface and concurrent nucleation and growth of Al-doped MgO-type of oxide islands on the alloy surface. Because the initial rate of coverage of the alloy surface with chemisorbed oxygen decreases with decreasing pO_2, the competing process of oxygen incorporation is promoted at a lower pO_2, whereas the formation of a closed oxide film on the bare alloy surface is promoted at a higher pO_2. As evidenced from the disappearance of the surface plasmon structure in the measured Mg 2p AR-XPS spectra of the oxidized alloys, a closed oxide film has in all cases formed within an oxidation time of 300 s, which corresponds to the shortest time employed in the AR-XPS investigations.

During the initial stages of oxygen incorporation, oxide nucleation and very fast oxide-film growth, the preferential oxidation of Mg from the alloy surface is much faster than the rate of supply of Mg from the interior of the alloy towards the reacting alloy/oxide/oxygen interface. Since a strong Al enrichment already exists in the alloy subsurface region at the onset of oxidation (due to the sputter-cleaning treatment; see above), it follows that the bare alloy surface is almost instantaneous depleted of Mg upon exposure to oxygen gas.

Consequently, a relatively Al-rich MgO-type of oxide phase is formed during the initial stages of oxide-film growth (i.e. Al-rich as compared to the Al-doped MgO-type of oxide formed during the subsequent, slow oxidation stage; see below). This implies that the Al-content incorporated in the developing oxide film is governed by the degree of Al enrichment in the alloy subsurface region prior to oxidation as induced by the sputter-cleaning treatment and *not* by the bulk Al content of the alloy. Consequently, a relatively much lower Al content in the grown oxide films was found for the alloy with the lowest bulk Al content of 2.63 at.% (since it also develops a relatively much weaker degree of Al-enrichment in the subsurface region upon sputter cleaning; see above).

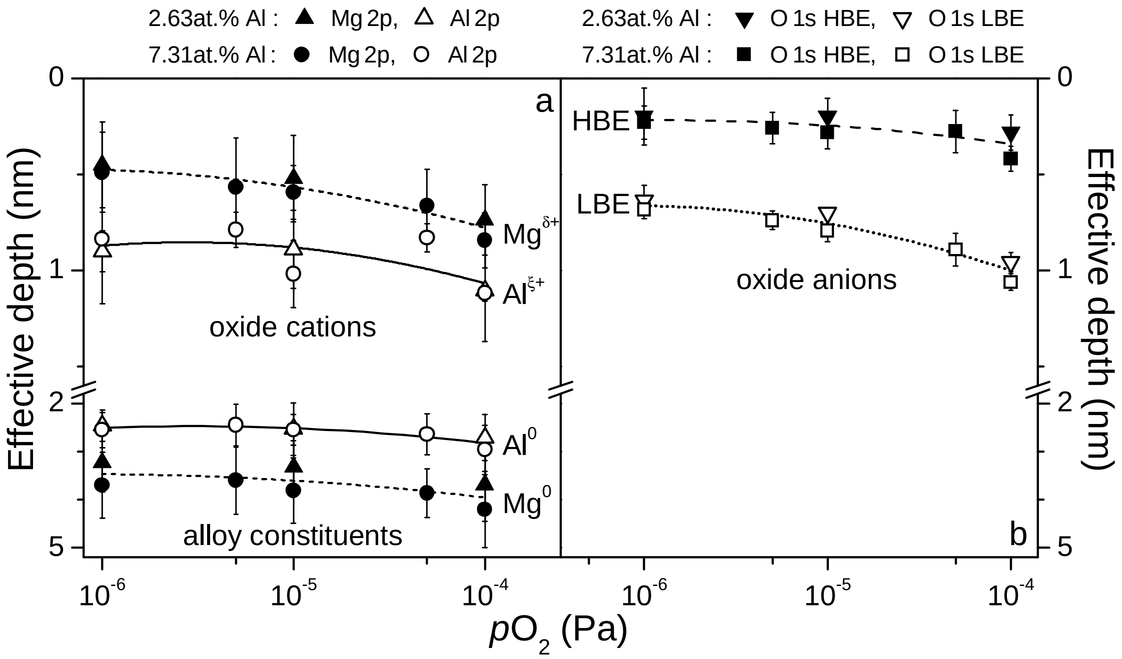

Figure 6.4. Effective depths below the oxide surface as a function of pO_2 for the (**a**) metallic and oxidic Mg 2p and Al 2p species and (**b**) the lower (LBE) and higher binding energy (HBE) O 1s species, as resolved from the measured AR-XPS spectra of the oxidized MgAl substrates (for 1 h at 304 K) of low (2.63 at.%) and high (7.31 at.%) bulk Al alloying content.

Subsequent growth after the formation of a closed oxide film on the bare alloy surface proceeds by the overgrowth of Mg-rich oxide by preferential oxidation of Mg from the alloy. The structure of the oxide films resembles an Al-doped MgO-type of oxide phase (rather than a $MgAl_2O_4$ spinel-type of oxide phase). The resulting, overall, non-stoichiometric oxide films are, on average, deficient of oxygen anions and slightly enriched of cations (with respect to MgO). With increasing pO_2, the overall anion molar density increases and the overall cation molar density decreases (approaching the value for stoichiometric MgO), while maintaining a constant ratio of Mg to Al cations in the oxide film (about independent of the bulk Al alloying content). As evidenced from the reconstructed effective depth plot in Fig. 6.4a, which provides a direct indication of the effective depths of different chemical species below the oxide-film surface, the oxide films are enriched of Al in the regions of the alloy and the oxide film adjacent to the alloy/oxide interface. The resolved LBE O 1s species is attributed to oxygen anions in the interior of the oxide film, whereas the HBE O 1s component has been shown to originate from a defect oxide structure in the surface-adjacent region of the oxide film (cf. Figs. 6.1 and 6.4b). After the formation of a 'closed' oxide film on the bare alloy surface, this defect oxide structure acts as a precursor for continued growth by the outward diffusion of Mg cations under influence of the surface-charge field setup up by chemisorbed oxygen species onto the oxide surface. The corresponding (approximately constant) growth rate during this slow growth stage increases with increasing pO_2. The associated depletion of Mg in the alloy subsurface region during the slow growth stage is then governed by the competing processes of preferential oxidation of Mg and oxidation-induced, chemical segregation of Mg from the interior of the alloy towards the alloy/oxide interface (with the relative contribution by chemical segregation increasing with increasing pO_2).

Chapter 7

Zusammenfassung: Über die anfängliche Oxidation von MgAl-Legierungen

Grundlegendes und weitreichendes Verständnis des Oxidationsverhaltens von reinen Metal- und Legierungsoberflächen ist von großer Bedeutung für zahlreiche Anwendungsgebiete wie die heterogene Katalyse, die Mikroelektronik, Oberflächenbeschichtungen oder Gassensoren. Zum Beispiel erhöhte sich das Interesse an den Anfangsstadien der thermischen Oxidation von Oberflächen binärer Legierungen bei niedrigen Temperaturen, weil die Anforderung besteht die physikalischen und chemischen Eigenschaften (wie Korrosionsbeständigkeit, elektrische und thermische Leitfähigkeit, Adhäsion oder katalytische Aktivität) von sehr dünnen (< 10 nm) Oxidschichten zu verbessern, indem man die Mikrostruktur von sowohl dem Legierungssubstrat als auch der Oxidschicht optimiert.

Diese Arbeit behandelt die anfänglichen Stadien der thermischen Oxidation von MgAl-Legierungen auf Mg-Basis bei Raumtemperatur. Legierungen auf Mg-Basis sind interessant für strukturelle Anwendungen, bei denen geringes Gewicht in Kombination mit einer verbesserten Recyclingfähigkeit verlangt wird (z.B. in der Automobil-, der Computer- oder der Luft- und Raumfahrtindustrie). Obwohl bekannt ist, dass das Zufügen von Al zu Mg dessen Gießbarkeit, Festigkeit, Härte und Oxidationsbeständigkeit erhöht, fehlt ein grundlegendes Wissen über die Mechanismen und Grenzen dieser Verbesserungen. Desweiteren stellt die Untersuchung der Oxidation von MgAl-Legierungen auf Mg-Basis bei niedrigen Temperaturen eine wissenschaftliche Herausforderung dar, weil die chemischen und physikalischen Naturen der beiden Legierungselemente (d.h. Mg und Al) sehr ähnlich sind (im Gegensatz zu binären Legierungen mit einem relativ gesehen edlerem Legierungselement, wie Cu-Au, Ag-Cu oder Pt-Al).

Die Anfangsstadien der thermischen Oxidation von reinen, polykristallinen MgAl-Legierungen auf Mg-Basis wurden durch Anwendung der Kombination aus winkelabhängiger Röntgen-Photoelektronenspektroskopie (AR-XPS) und dynamischer, in-situ spektroskopischer Ellipsometrie (RISE) untersucht. Alle Oxidationsexperimente wurden unter kontrollierten Bedingungen in einer UHV-Reaktionskammer (RC; Basisdruck < 2.5×10^{-8} Pa) durchgeführt, die ausgestattet ist mit: (*i*) einer Einheit zur kontrollierten Einführung von reinem O_2-Gas, (*ii*) einem Massenspektrometer zur Bestimmung des Restgasgehalts und zur Kontrolle des Sauerstoffpartialdrucks (pO_2) während des Schichtwachstums, und (*iii*) einem in-situ, spektroskopischen Ellipsometers für Echtzeitanalysen der Oxidschichtwachstumskinetik. Diese UHV-RC ist direkt mit der UHV-Kammer (Basisdruck $< 5\times10^{-8}$ Pa) für AR-XPS der gewachsenen Oxidschichten verbunden.

Auf Grund ihrer hohen Reaktivität sind die MgAl-Probenoberflächen, bevor sie in das UHV System gebracht werden, immer mit einer natürlichen Oxidschicht einer Dicke von einigen Nanometern bedeckt. Um diese natürliche Oxidschicht und andere Verunreinigungen von der Legierungsoberfläche zu entfernen, werden die MgAl-Substrate durch Ionenbeschuß gereinigt, indem die gesamte Probenoberfläche von einem fokussiertem 1 kV Ar^+-Strahl abgerastert wird. Die so erhaltenen Legierungssubstrate werden hier als *blanke* Substrate bezeichnet. Blanke MgAl-Substrate mit verschiedenen Al-Volumengehalten (2,63 At.%, 5,78 At.%, 7,31 At.%) wurden anschließend für verschiedene Zeiten (von 300 s bis zu 1 h) bei T = 304 K (Raumtemperatur) und bei verschieden Sauerstoffpartialdrücken (pO_2) im Bereich von 10^{-6} – 10^{-4} Pa mit reinem O_2 Gas oxidiert. RISE wurde angewandt um die Oxidschichtwachstumskinetik und die Entwicklung des Oxidschichtsaufbaus (die durch die Änderung der optischen Konstanten der wachsenden Oxidschicht angezeigt wird) zu ermitteln. Die Mikrostruktur der wachsenden Oxidschicht, d.h. die Dicke, die Morphologie, die Tiefenverteilung von verschiedenen chemischen Spezies, die Zusammensetzung und die Defektstruktur der wachsenden Oxidschicht, wurde mit AR-XPS bestimmt.

Das verwendete XPS-Instrument, das dem neusten Stand der Technik entspricht, besitzt die Möglichkeit die emittierten Photoelektronen gleichzeitig über einen großen Winkelbereich zu detektieren ohne die Probe zu verkippen (im Folgenden bezeichnet als paralleler Datenaufzeichnungsmodus). Dieses reduziert die Aufnahmezeit einer Serie von AR-XPS Spektren erheblich und garantiert eine konstante Analysefläche und Position. Im Gegensatz zu einem konventionellen XPS-Aufbau ist der Winkel ϕ zwischen den einfallenden Röntgenstrahlen und den detektierten Photoelektronen bei XPS-Spektren, die im parallelen Datenaufzeichnungsmodus aufgenommen wurden, keine Konstante, sondern variiert mit dem Winkel α zwischen dem Detektor und der Probenoberflächennormale. Wie bei einer grundlegenden Untersuchung in der vorliegenden Arbeit (Kapitel 2) gezeigt wurde, müssen die Anisotropie der Photoionisationsquerschnitte jeder untersuchten Grundniveauphotoelektronenlinie, sowie die Auswirkungen von elastischen Streuungen der detektierten Photoelektronen im Festkörper für eine genaue quantitative Analyse dieser AR-XPS Spektren berücksichtigt werden. Wie für die quantitative Analyse der Al 2p und O 1s Photoelektronenlinien eines α-Al_2O_3 Standards gezeigt wurde, führt hier das Ignorieren der

Auswirkungen der Anisotropie der Photoionisationsquerschnitte und der elastischen Streuungen zu Fehlern von bis zu 16% bei der AR-XPS Analyse der Zusammensetzung. Umständliche Korrekturen für die Auswirkungen der Anisotropie der Photoionisationsquerschnitte und der elastischen Streuungen (z.B. für die quantitative Analyse von Festkörpern und Dünnschichtstrukturen unbekannter Zusammensetzung und/oder Dicke) können umgangen werden, wenn Werte für die relativen Sensitivitätsfaktoren als Funktion der Winkel α und ϕ eingeführt werden, die experimentell mit Hilfe von geeigneten Standards bekannter Zusammensetzung ermittelt wurden (Kapitel 2 dieser Arbeit).

Um die Dicke, die Zusammensetzung und den Aufbau (d.h. die Tiefenverteilung der vorhandenen chemischen Spezies) der Oxidschichten, die auf den blanken MgAl-Substraten gewachsen sind, als Funktion der Oxidationsbedingungen mit AR-XPS zu ermitteln, muss die Gesamtintensität von sechs verschiedenen verlustfreien primären (PZL) Photoelektronenintensitäten[10] in der Quantifizierung berücksichtigt werden: d.h. die PZL-Intensitäten der metallischen und oxidischen Mg 2p Hauptpeaks (Abb. 7.1a), die PZL-Intensitäten der metallischen und oxidischen Al 2p Hauptpeaks (Abb. 7.1b) und die PZL-Intensitäten der ermittelten O 1s Hauptpeaks (Abb. 7.1c). Desweiteren sind in der Quantifizierung bereits existierende oder abgeschätzte Werte für die Wahrscheinlichkeiten der intrinsischen Mg 2p und Al 2p Plasmonenanregungen in der Legierung, sowie auch für die Oxidschichtdichte und/oder für die effektiven Abschwächungslängen der detektierten Photoelektronen in der Oxidschicht erforderlich.

Deshalb wurde ein neues Verfahren für die quantitative Analyse der gemessenen AR-XPS Spektren von blanken und oxidierten MgAl-Substraten entwickelt, welches die genaue quantitative Analyse von AR-XPS Spektren dünner Oxidschichten ermöglicht, welche auf binäre Legierungssubstraten durch thermische oder Plasma-Oxidation gewachsen sind (Kapitel 3 dieser Arbeit). Dazu wurden zuerst die metallischen Mg 2p und Al 2p, die oxidischen Mg 2p und Al 2p und die O 1s PZL-Gesamtintensitäten aus den gemessen XPS Spektren der blanken und oxidierten MgAl-Substrate aufgelöst (siehe z.B. Abb. 7.1). Als nächstes wurden die Gleichungen und dazugehörigen Berechnungsschritte für die

[10] Die verlustfreie primäre Photoelektronengesamtintensität eines gegebenen Rumpfelektronenniveaus umfasst alle aufgenommenen Photoelektronen, die nach dem Verlassen des Rumpfelektronenniveaus des Atoms in dem Festkörper unbeeinflusst bleiben (d.h. alle aufgenommenen ungestreuten oder elastisch gestreuten Photoelektronen).

Bestimmung der durchschnittlichen Oxidschichtdicke, der Gesamtzusammensetzung und der effektiven Tiefenverteilung der vorhandenen chemischen Spezies aus den Grundgleichungen der zugehörigen Mg 2p, Al 2p und O 1s PZL Photoelektronenintensitäten hergeleitet. Die so mittels AR-XPS erhaltenen Werte der Schichtdicke der gewachsenen Oxidschichten stimmen gut mit den dazugehörigen Oxidschichtwachtumkurven überein, welche durch RISE ermittelt wurden (siehe z.B. Abb. 7.2).

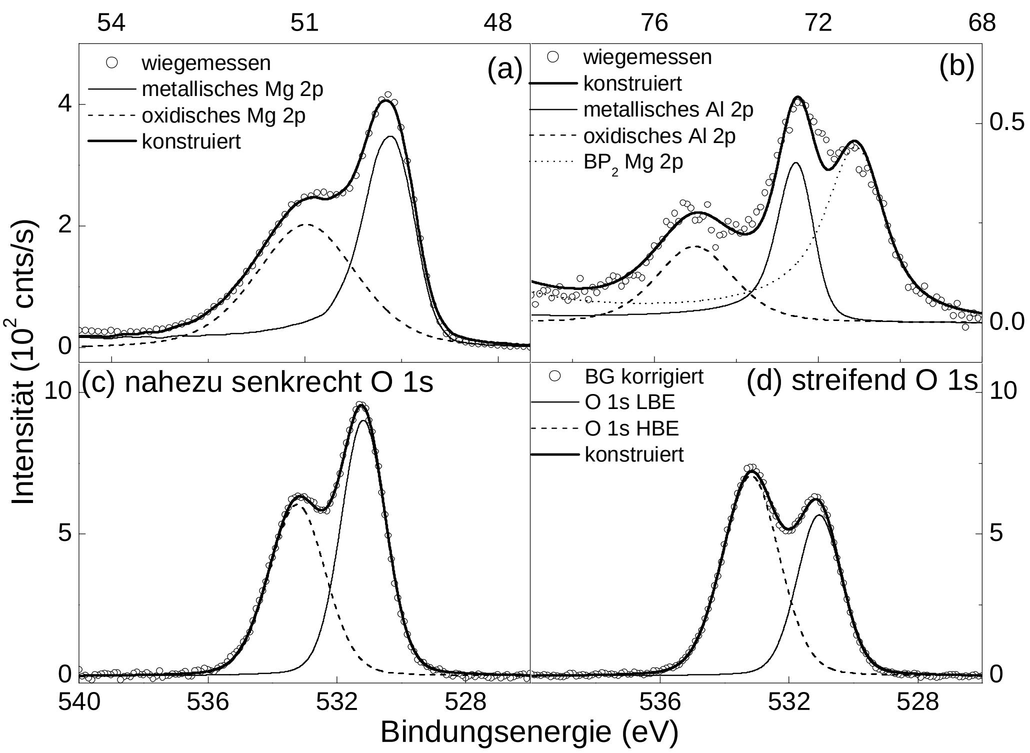

Abbildung 7.1. (**a**) Gemessenes und rekonstruiertes Mg 2p Spektrum des oxidierten Mg-2,63 At. % Al Substrats (1 h bei 304 K und pO_2 = 1×10^{-4} Pa), wie es unter den Detektorwinkeln (α,ϕ)=(34.3°,51.7°) aufgenommen wurde. Das rekonstruierte Mg 2p Spektrum besteht aus einem einzelnen metallischen und einem einzelnen oxidischen Mg 2p Hauptpeak. (**b**) Die dazugehörigen gemessenen und rekonstruierten Al 2p Spektren der oxidierten Legierung. Neben einem einzelnen metallischen und einem einzelnen oxidischen Al 2p Hauptpeak, enthält das gesamte rekonstruierte Al 2p Spektrum auch einen Anteil von dem zweiten Volumenplasmonpeak (BP_2) des metallischen Mg 2p Hauptpeaks aus (a). Die zugehörigen hintergrundkorrigierten und rekonstruierten O 1s Spektren der oxidierten Legierung, die unter (**c**) nahezu senkrechtem mit (α,ϕ)=(34.3°,51.7°) und (**d**) streifendem mit $(\alpha,\phi) = (71.8^{\circ}, 83.8^{\circ})$ Detektorwinkel aufgenommen wurden. Das rekonstruierte O 1s Spektrum enthält zwei Komponenten an der niedrigen (LBE) bzw. der hohen Bindungsenergieseite (HBE). Die relativen Beiträge der LBE und HBE Komponente dominieren bei nahezu senkrechtem bzw. streifendem Detektorwinkel.

Für die in-situ Untersuchung der Oxidschichtwachstumskinetik mittels RISE wurden die Änderungen der amplituden- und phasenabhängigen Ellipsometrieparameter ψ und Δ als Funktion der Oxidationszeit gleichzeitig für verschiedene Wellenlängen, λ, des eintreffenden polarisierten Lichts über einen Wellenlängenbereich von 350 nm bis 700 nm gemessen (siehe z.B. Abb. 7.3). Der Tangens des Winkels ψ entspricht dem Verhältnis der Gesamtreflektionskoeffizienten (d.h. der Amplitude der reflektierten Welle relativ zu der der einfallenden Welle) der Anteile des elektrischen Feldvektors des polarisierten Lichts parallel (p-Welle) bzw. senkrecht (s-Welle) zur Einfallsebene. Der Winkel Δ entspricht dem Unterschied zwischen den Phasenverschiebungen der p- bzw. s-Wellen während der Reflektion.

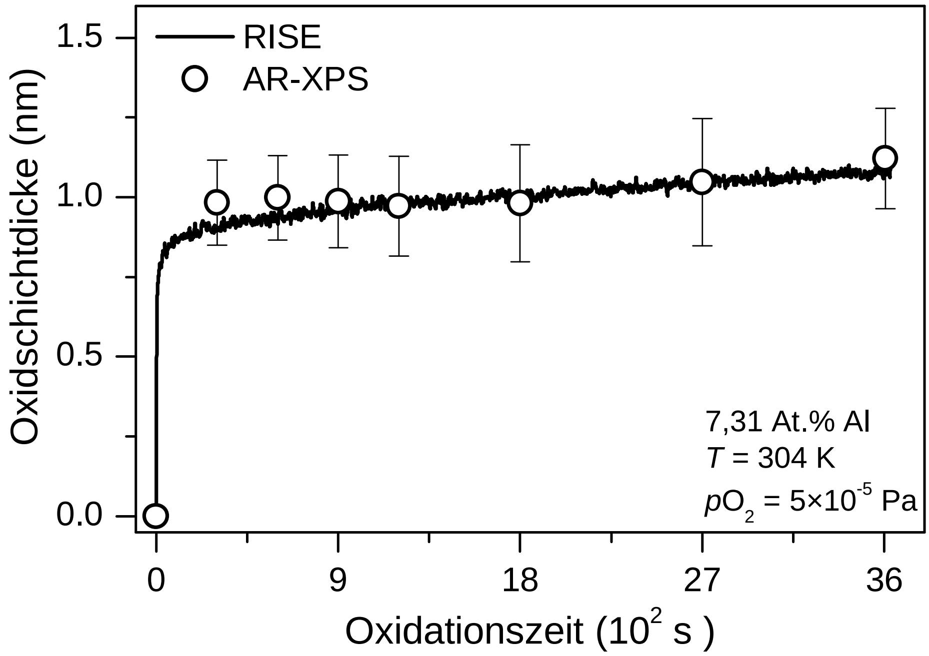

Abbildung 7.2. Gesamtoxidschichtdicke als Funktion der Oxidationszeit, für die Oxidation des blanken Mg – 7,31 At.% Al Substrats bei 304 K und pO_2 = 5×10^{-5} Pa. Die durchschnittlichen Gesamtoxidschichtdickenwerte wurden unabhängig von einander aus (*i*) den mit AR-XPS gemessenen Mg 2p –Al 2p und O 1s Photoelektronenspektren der oxidierten Legierungssubstrate (siehe Abb. 7.1), und (*ii*) aus den mit in-situ Ellipsometrie gemessenen Spektren der Phasen- und Amplitudenparameter, Δ and ψ, über einen Wellenlängenbereich von 350-700 nm (siehe Abb. 7.3), ermittelt.

Verschiedene Modelle wurden entwickelt um die gemessene Zeitabhängigkeit der Spektren von $\Delta(\lambda)$ und $\psi(\lambda)$ während der anfänglichen und folgenden Oxidationsstadien zu beschreiben. Die gemessenen Änderungen von $\Delta(\lambda)$ und $\psi(\lambda)$ als Funktion der Zeit konnten gut beschrieben werden, indem angenommen wird, dass sich eine Al-dotierte MgO-ähnliche Schicht mit einer inhomogenen Al-Verteilung auf der MgAl-Legierungsoberfläche bildet

(Kapitel 4 dieser Arbeit und Abb. 7.3). Die optischen Konstanten des MgAl-Substrats (als Funktion von λ) wurden aus der in-situ Messung des blanken Legierungssubstrats vor jeder Oxidation bestimmt. Die optischen Konstanten für Al-dotiertes MgO wurden über die optischen Konstanten von reinem MgO und Al-Metall abgeschätzt, indem ein 'Effective Medium Approach' auf Basis des Maxwell-Garnett-Formalismus mit MgO als Matrix verwendet wurde. Um eine inhomogene Tiefenverteilung des Al in dieser Al-dotierten MgO-ähnlichen Schicht zu beschreiben (Al ist in der Oxidschicht an der Legierungs/Oxid-Grenzfläche konzentriert; siehe unten), wurde eine so genannte 3-Knoten EMA-Schicht-Näherung angewendet, indem der EMA-Anteil von Al von der Grenzfläche zu einer variablen Position innerhalb der MgO-Schicht linear von 0,75 bis Null abfällt, während der EMA-Anteil von Al in dem restlichen, oberen Teil der MgO-Schicht (d.h. nahe der Oberfläche) Null ist.

Die Anwendung einer solchen Modellierung auf die gemessenen Spektren von $\Delta(\lambda)$ und $\psi(\lambda)$ als Funktion der Oxidationszeit bei thermischer Oxidation von blanken MgAl-Legierungen bei 304 K in dem pO_2 Bereich von 10^{-6} bis 10^{-4} Pa ergibt einen linearen Zusammenhang zwischen der Änderung von Δ (d.h. $\delta\Delta$) und der Änderung in der Oxidschichtdicke für Dicken von bis zu etwa 3 nm. Die so erhaltenen Oxidschichtdicken stimmen gut mit den dazugehörigen Dickenwerten überein, welche unabhängig durch AR-XPS Analyse ermittelt wurden (siehe z.B. Abb. 7.2). Ein entsprechender linearer Zusammenhang zwischen $\delta\psi$ und der Oxidschichtdicke ist aus der vorliegenden Arbeit nicht ersichtlich, was bedeutet, dass in erster Näherung der ellipsometrische Parameter ψ für die Anwesenheit einer transparenten Dünnschichtphase zwischen der Umgebung und dem Substrat nicht empfindlich ist. Stattdessen wird der anfängliche Abfall und der anschließende steile Anstieg von ψ während des ersten Stadiums mit schnellem Oxidschichtwachstum (siehe z.B. Abb. 7.3a, c) durch die gleichzeitig stattfindenden Vorgänge von Sauerstoffaufnahme in die Legierungsoberfläche, sowie von Keimbildung und Wachstum Al-dotierter MgO-Inseln auf der blanken Legierungsoberfläche verursacht. Während des folgenden Stadiums mit langsamem Oxidschichtwachstums nach der Bildung einer geschlossenen Oxidschicht auf der Legierungsoberfläche wird der schrittweise Anstieg von ψ bei hohen pO_2 (siehe z.B. Abb. 7.3c) hauptsächlich durch die Zusammensetzungsänderungen im MgAl-Substrat an der Legierungs/Oxid-Grenzfläche bestimmt. Diese Zusammensetzungsänderungen finden auf Grund von zwei gleichzeitig ablaufenden Vorgängen statt: der (durch Oxidation verursachten) Segregation von Mg aus dem Inneren der Legierung an die Legierungs/Oxid-Grenzfläche und der bevorzugten Oxidation von Mg.

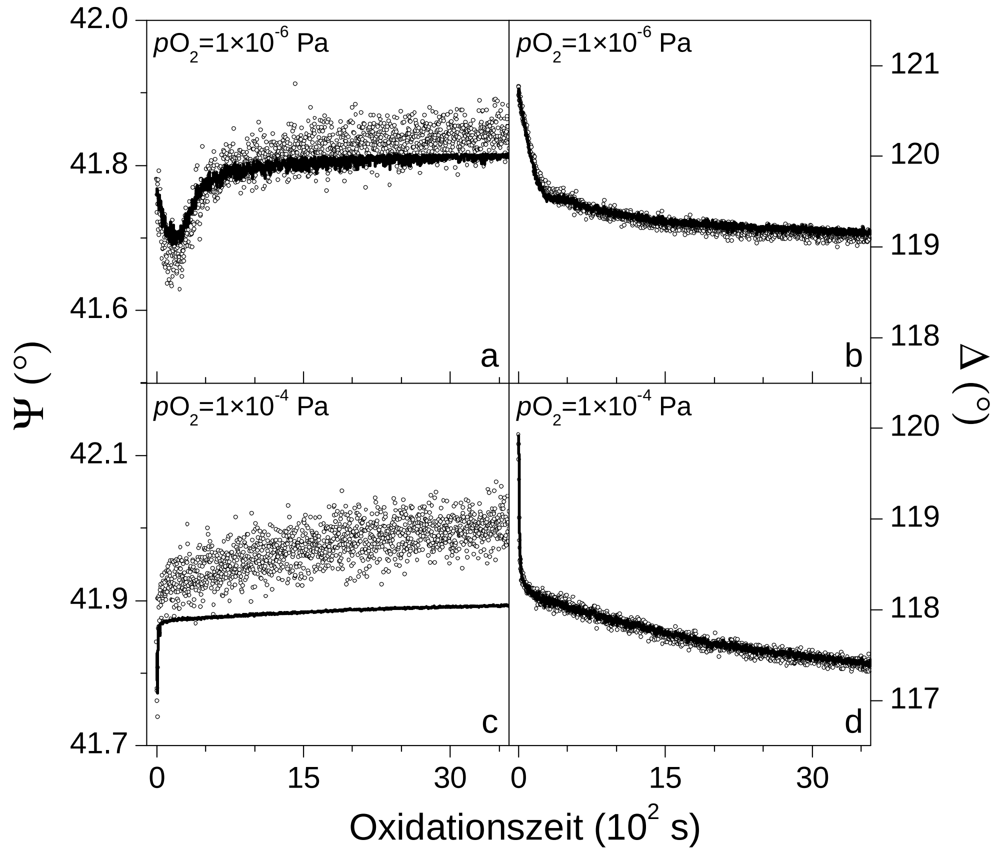

Abbildung 7.3. Die gemessenen (*Symbole*) und gefitteten (*Linien*) Werte der ellipsometrischen Phasen- und Amplitudenparameter, Δ und ψ, als Funktion der Oxidationszeit für eine einzelne Wellenlänge von λ = 525 nm. Die Daten wurden während der Oxidation eines blanken Mg – 7,31At.% Al Substrats bei 304 K für 1 h bei einem niedrigen (1×10^{-6} Pa) bzw. einem hohen pO_2 (1×10^{-4} Pa) gemessenen. Die gemessenen Änderungen in $\Delta(\lambda)$ und $\psi(\lambda)$ als Funktion der Zeit konnten beschrieben werden, indem angenommen wurde, dass auf der MgAl Legierungsoberfläche eine Al-dotierte MgO-ähnliche Oxidschicht mit inhomogener Verteilung von Al wächst (Kapitel 4 dieser Arbeit).

Durch die Anwendung der zuvor genannten Techniken und die Verwendung geeigneter Verfahren zur Quantifizierung wurden die folgenden Ergebnisse für die Anfangsstadien der thermischen Oxidation von reinen, polykristallinen MgAl-Substraten verschiedener Al-Legierungskonzentrationen (d.h. 2,63 At.%, 5,78 At.%, 7,31 At.%) bei T = 304 K im pO_2 Bereich von 10^{-6} – 10^{-4} Pa ermittelt (Kapitel 5 dieser Arbeit).

Auf Grund der konkurrierenden Prozesse des bevorzugten Sputterns (d.h. der Entfernung) von Mg aus der mit Ionen beschossenen Legierungsoberfläche und der durch den Ionenbeschuss verstärkten Gibbs'schen Segregation von Mg aus dem Inneren der Legierung an die mit Ionen beschossene Oberfläche entsteht eine starke Al-Anreicherung an der Legierungsoberfläche während des Sputterreinigungsschritts (vor der Oxidation). Daraus folgt, dass zu Beginn jeder Oxidation der Al-Gehalt in der Oberflächenregion der Legierung bei weitem den Al-Volumengehalt der Legierung übersteigt. Die Stärke der Al-Anreicherung in der Oberflächenregion der Legierung fällt stark mit zunehmender Tiefe unterhalb der Legierungsoberfläche ab und erreicht die Volumenzusammensetzung in einer Tiefe von 4-6 nm unterhalb der Probenoberfläche. Die Tiefe, in der die Volumenzusammensetzung erreicht wird, fällt mit sinkendem Al-Volumengehalt in der Legierung ab.

Zwei verschiedene Wachstumsstadien wurden bei der Oxidation von blanken MgAl-Substraten identifiziert: ein kurzes, Anfangsstadium mit sehr schnellem Oxidschichtwachstum und ein folgendes, viel langsameres, aber fortlaufendes Wachstumsstadium. Die erste Reaktion von Sauerstoffgas mit dem blanken Legierungssubstrat läuft durch die anfängliche Aufnahme von Sauerstoff in die Legierungsoberfläche und gleichzeitige Keimbildung und Wachstum von Al-dotierten MgO-ähnlichen Oxidinseln auf der Legierungsoberfläche ab. Weil die anfängliche Bedeckungsrate der Legierungsoberfläche mit chemisorbiertem Sauerstoff geringer ist für niedrigen pO_2, wird der konkurrierende Prozess der Sauerstoffaufnahme in die Legierungsoberfläche bei niedrigem pO_2 bevorzugt, während die Bildung einer geschlossenen Oxidschicht auf der blanken Legierungsoberfläche bei hohem pO_2 bevorzugt wird. Wie durch das Verschwinden der Oberflächenplasmonstruktur in dem gemessenen Mg 2p AR-XPS Spektrum der oxidierten Legierung angezeigt wird, hat sich in allen Fällen innerhalb einer Oxidationszeit von 300 s eine geschlossene Oxidschicht gebildet, was der kürzesten Zeit entspricht, nach welcher AR-XPS Untersuchungen durchgeführt wurden.

Während der Anfangsstadien der Sauerstoffaufnahme, der Oxidkeimbildung und des sehr schnellen Oxidschichtwachstums ist die bevorzugte Oxidation von Mg aus der Legierungsoberfläche wesentlich schneller als die Nachschubrate von Mg aus dem Inneren der Legierung zu der reagierenden Legierungs/Oxid/Sauerstoff-Grenzfläche. Da schon beim Einsetzen der Oxidation eine starke Al-Anreicherung in der Oberflächenregion der Legierung vorhanden ist (auf Grund des Sputterreinigungsschritts, siehe oben), folgt, dass beim Begasen mit Sauerstoff die blanke Legierungsoberfläche fast augenblicklich vollständig an Mg verarmt. Folglich entsteht während der Anfangsstadien des Oxidschichtwachstums eine relativ Al-reiche MgO-ähnliche Oxidphase (d.h. Al-reich im Vergleich zu dem Al-dotierten MgO-ähnlichen Oxid, welches während des folgenden, langsameren Oxidationsstadiums entsteht, siehe unten). Das bedeutet, dass der Al-Gehalt in der gewachsenen Oxidschicht durch die Höhe der Al-Anreicherung in der Oberflächenregion der Legierung vor der Oxidation bestimmt wird (d.h. durch den Sputterreinigungsschritt) und *nicht* durch den Al-Volumengehalt der Legierung. Deshalb wurde ein relativ gesehen viel geringerer Al-Gehalt in der Oxidschicht gefunden, die auf der Legierung mit dem geringsten Al-Gehalt von 2,63 At.% gewachsen ist (da hier auch eine relativ gesehen viel schwächere Al-Anreicherung in der Oberflächenregion der Legierung während des Sputterreinigungsschritts entsteht, siehe oben).

Fortschreitendes Wachstum nach der Bildung einer geschlossenen Oxidschicht auf der Legierungsoberfläche geschieht durch bevorzugte Oxidation von Mg aus der Legierung und das Aufwachsen eines Mg-reichen Oxids. Die Struktur der Oxidschicht gleicht eher einer Al-dotierten MgO-Phase als einer $MgAl_2O_4$ Spinelphase. Die erhaltenen, insgesamt unstöchiometrischen Oxidschichten sind im Durchschnitt an Sauerstoffanionen verarmt und mit Kationen leicht angereichert (in Bezug auf MgO). Ein höherer pO_2 ergibt eine höhere molare Gesamtdichte der Anionen und eine niedrigere molare Gesamtdichte der Kationen, während das Verhältnis von Mg- zu Al-Kationen in der Oxidschicht konstant bleibt (nahezu unabhängig vom Al-Volumengehalt der Legierung). Der effektiven Tiefenplot in Abb. 7.4a ist

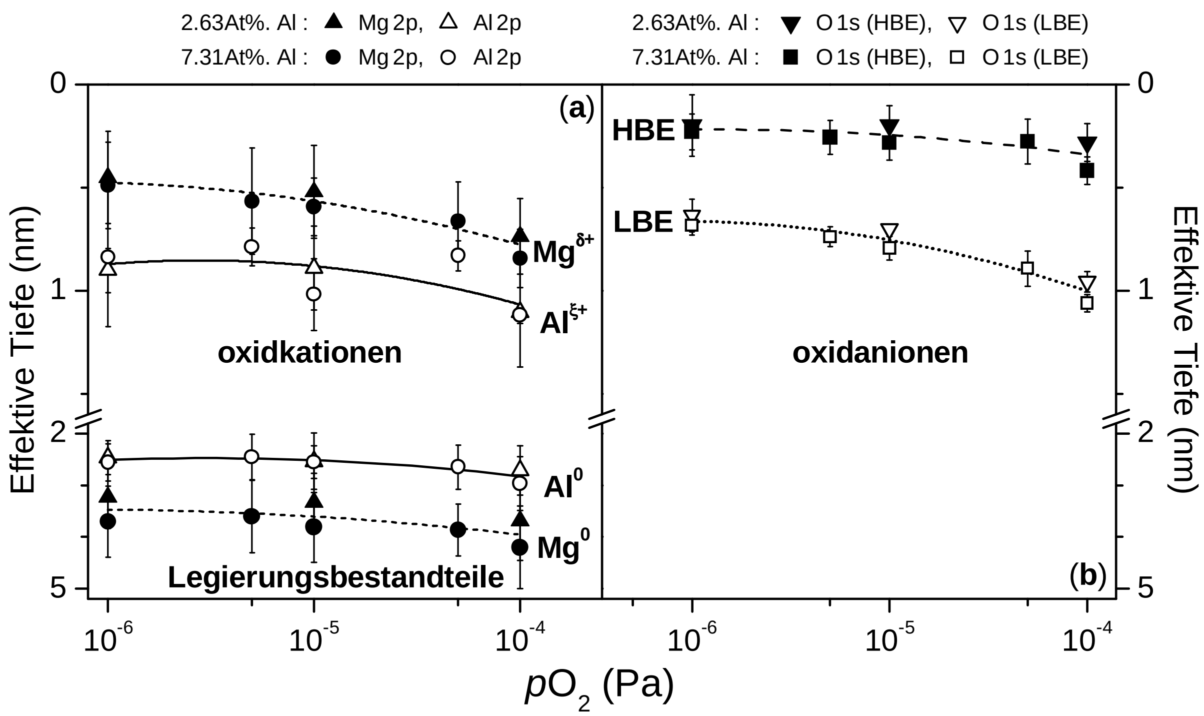

Abbildung 7.4. Effektive Tiefe unterhalb der Oxidoberfläche als Funktion des pO_2 für (**a**) die metallischen und oxidischen Mg 2p und Al 2p Spezies und (**b**) die niedrigen (LBE) und hohen Bindungsenergie (HBE) O 1s Spezies, wie sie aus den gemessenen AR-XPS Spektren der oxidierten MgAl-Substrate (für 1 h bei 304 K) mit geringem (2,63 at.%) und hohem (7,31 at.%) Al-Volumengehalt in der Legierung ermittelt wurde.

eine direkte Darstellung der effektiven Tiefen der verschiedenen chemischen Spezies unterhalb der Oxidschichtoberfläche. Es folgt daraus, dass die Oxidschichten in den Regionen der Legierung und der Oxidschicht in der Nähe der Legierungs/Oxid-Grenzfläche mit Al angereichert sind. Die identifizierten LBE O 1s Spezies kann auf Sauerstoffanionen im Inneren der Oxidschicht zurückgeführt werden, während die identifizierten HBE O 1s Spezies auf eine Defektstruktur in der oberflächennahen Region der Oxidschicht zurückzuführen ist (siehe z.B. Abb. 7.1 und 7.4b). Nach der Bildung einer geschlossenen Oxidschicht auf der Legierungsoberfläche agiert diese Oxiddefektstruktur als Precursor für kontinuierliches Oxidschichtwachstum durch Auswärtsdiffusion von Mg-Kationen unter dem Einfluss eines Oberflächenladungsfeldes, welches durch chemisorbierte (negativ geladene) Sauerstoffspezies an der Oxidoberfläche verursacht wird. Die zugehörige (ungefähr konstante) Wachstumsrate während dieses langsamen Wachstumsstadiums ist bei höherem pO_2 höher. Die gleichzeitige Verarmung von Mg in der Oberflächenregion der Legierung während des langsamen Wachstumsstadiums wird dann von den konkurrierenden Abläufen der bevorzugten Oxidation von Mg und der durch die Oxidation hervorgerufenen, chemischen Segregation von Mg aus dem Inneren der Legierung zur Legierungs/Oxid-Grenzfläche bestimmt (wobei der relative Anteil der chemischen Segregation bei höheren pO_2 größer ist).

References

1. H.H. Kung, *Transition Metal Oxides: Surface Chemistry and Catalysis*, (Elsevier, Amsterdam, 1989).
2. *Adsorption on Ordered Surfaces of Ionic Solids and Thin Films*, Vol. 33, Eds. H.-J. Freund and E. Umbach, (Springer Verlag, Heidelberg, 1993).
3. S.M. Goodnick, M. Fathipour, D.L. Ellsworth, and C.W. Wilmsen, *J. Vac. Sci. Technol.*, **18** (1981), 949.
4. A.G. Revesz and J. Kruger, *Passivity of Metals*, Eds. R.P. Frankenthal and J. Kruger, (The Electrochemical Society, Princeton, NJ, 1978), p. 137.
5. R. Franchy, *Surf. Sci. Rep.*, **38** (6-8) (2000), 195.
6. J. A. T. Fromhold, *Defects in Crystalline Solids*, Vol. 9, (North-Holland, New York, 1976).
7. N. Cabrera and N.F. Mott, *Rep. Progr. Phys.*, **12** (1949), 163.
8. P. Kofstad, *High-Temperature Oxidation of Metals*,(John Wiley & Sons, Inc., 1966).
9. T.J. Nijdam, L.P.H. Jeurgens, and W.G. Sloof, *Acta Materialia*, **51** (2003), 5295.
10. T.J. Nijdam, L.P.H. Jeurgens, and W.G. Sloof, *Acta Materialia*, **53** (2005), 1643.
11. J.A.T. Fromhold and E.L. Cook, *Phys. Rev*, **158** (3) (1967), 600.
12. A.T. Fromhold and E.L. Cook, *Phys. Rev.*, **163** (1967), 650.
13. E. Fromm, *Kinetics of Metal-Gas Interactions at Low Temperatures Hydriding, Oxidation, Poisoning*, (Springer-Verlag, Heidelberg, 1998).
14. A. Lyapin, L.P.H. Jeurgens, and E.J. Mittemeijer, *Acta Materialia*, **53** (2005), 2925.
15. L.P.H. Jeurgens, A. Lyapin, and E.J. Mittemeijer, *Acta Materialia*, **53** (2005), 4871.
16. L.P.H. Jeurgens, W.G. Sloof, F.D. Tichelaar, and E.J. Mittemeijer, *Thin Solid Films*, **418** (2) (2002), 89.
17. G.L. Maker, J. Kruger, and A. Joshi, eds. Proc. Advances in Magnesium Alloys and Composites, ed. H. Paris and W. Hunt. 1988, TMS: Phoenix. p. 105.
18. J.D. Hanawalt, C.E. Nelson, and J.A. Peloubet, *Trans. AMIE*, **147** (1942), 273.
19. L.P.H. Jeurgens, W.G. Sloof, F.D. Tichelaar, and E.J. Mittemeijer, *J. Appl. Phys.*, **92** (2002), 1649.
20. A. Lyapin, L.P.H. Jeurgens, P.C.J. Graat, and E.J. Mittemeijer, *J. Appl. Phys.*, **96** (12) (2004), 7126.

21. P.J. Cumpson, in *Surface Analysis by Auger and X-Ray Photoelectron Spectroscopy*, D. Briggs and J.T. Grant, (IM Publications and SurfaceSpectra Limited, Manchester, 2003), Chptr. 23.
22. L.P.H. Jeurgens, W.G. Sloof, F.D. Tichelaar, and E.J. Mittemeijer, *Surf. Sci.*, **506** (3) (2002), 313.
23. P.C. Snijders and L.P.H. Jeurgens, *Surf. Sci.*, **589** (2005), 98.
24. P. Kappen, K. Reihs, C. Seidel, M. Voetz, and H. Fuchs, *Surf. Sci.*, **465** (2000), 40.
25. R.M.A. Azzam and N.M. Bashara, *Ellipsometry and Polarized Light*, (North-Holland, Amsterdam, 1987).
26. C.S. Fadley, R.J. Baird, W. Seikhaus, T. Novakov, and S.A.L. Bergstroem, *J. Elec. Spectrosc.*, **4** (1974), 93.
27. C.S. Fadley, in *Electron Spectroscopy: Theory, Techniques and Applications*, C.R. Brundle and A.D. Baker, (Academic Press, London, 1978).
28. A. Jablonski, *Surf. Interface Anal.*, **14** (1989), 659.
29. L.P.H. Jeurgens, W.G. Sloof, C.G. Borsboom, F.D. Tichelaar, and E.J. Mittemeijer, *Appl. Surf. Sci.*, **161** (2000), 139.
30. L.P.H. Jeurgens, *On the initial oxidation of aluminium in oxygen gas* Delft University of Technology, The Netherlands, 2001.
31. J. Yeh and I. Lindau, *At. Data Nucl. Data Tables*, **32** (1985), 1.
32. M. Band, Y.I. Kharitonov, and M.B. Trzhaskovskaja, *At. Data Nucl. Data Tables*, **23** (1979), 443.
33. R.F. Reilman, A. Msezane, and S.T. Manson, *J. Electron Spectrosc. Relat. Phenom.*, **8** (1976), 389.
34. A. Jablonski and J. Zemek, *Phys. Rev. B*, **48** (7) (1993), 4799.
35. A. Jablonski and C.J. Powell, *Phys. Rev. B*, **50** (7) (1994), 4739.
36. A. Jablonski and C.J. Powell, *Surf. Sci. Reports*, **47** (2002), 33.
37. A. Jablonski and I.S. Tilinin, *J. Electron Spectrosc. Relat. Phenom.*, **74** (1995), 207.
38. A. Jablonski, *Phys. Rev. B*, **58** (24) (1998), 16470.
39. S. Chandrasekhar, *Radiative Transfer*, (Dover Publications Inc., New York, 1960), Chptr. 5.
40. M.P. Seah and I.S. Gilmore, *Surf. Interface Anal.*, **31** (2001), 835.
41. C.J. Powell, *Appl. Surf. Sci.*, **89** (1995), 141.
42. C.D. Wagner, D.E. Passoja, H.F. Hillery, T.G. Kinisky, H.A. Six, W.T. Jansen, and J.A. Taylor, *J. Vac. Sci. Tech. A*, **21** (4) (1982), 933.

43. W.Y. Ching and Y.-N. Xu, *J. Am. Ceram. Soc.*, **77** (1994), 412.
44. S. Tanuma, C.J. Powell, and D.R. Penn, *Surf. Interface Anal.*, **21** (1994), 165.
45. A. Jablonski and C.J. Powell, *NIST Electron Elastic-Scattering Cross-Section Database*, (U.S. Department of Commerce, Technology Administration, NIST, Standard Reference Data Program, Gaithesburg, Maryland 20899, 2000).
46. R.L. Opila and J.E. Jr., *Progr. Surf. Sci.*, **69** (2002), 125.
47. L.P.H. Jeurgens, W.G. Sloof, C.G. Borsboom, F.D. Tichelaar, and E.J. Mittemeijer, *Appl. Surf. Sci.*, **144-145** (1999), 11.
48. M. Kurth, P.C.J. Graat, and E.J. Mittemeijer, *Appl. Surf. Sci.*, **220** (1-4) (2003), 60.
49. M.S. Vinodh and L.P.H. Jeurgens, *Surf. Interface Anal.*, **36** (2004), 1629.
50. M.S. Vinodh, L.P.H. Jeurgens, and E.J. Mittemeijer, (2005), to be communicated to *Acta Materialia* (Chapter 5 in this thesis).
51. S. Tougaard, *Surf. Interface Anal.*, **11** (1988), 453.
52. M. Kurth and P.C.J. Graat, *Surf. Interface Anal.*, **34** (2002), 220.
53. A. Lyapin and P.C.J. Graat, *Surf. Sci.*, **552** (2004), 160.
54. S. Doniach and M. Sunjic, *J. Phys. C*, **3** (1970), 285.
55. S. Tougaard, *Surf. Interface Anal.*, **25** (1997), 137.
56. Matlab, The MathWorks Inc., Natick, 2001.
57. C. Jansson, S. Tougaard, G. Beamson, D. Briggs, S.F. Davies, A. Rossi, R. Hauert, G. Hobi, N.M.D. Brown, B.J. Meenan, C.A. Anderson, M. Repoux, C. Malitesta, and L. Sabbatini, *Surf. Interface Anal.*, **23** (1998), 484.
58. H. Muellejans and R.H. French, *Microsc. Microanal.*, **6** (2000), 297.
59. S.D. Mo and W.Y. Ching, *Phys. Rev. B*, **54** (1996), 16555.
60. J.H. Scofield, *J. Elect. Spectrosc. Relat. Phenom.*, **8** (1976), 129.
61. L.P.H. Jeurgens, A. Lyapin, and E.J. Mittemeijer, *Surf. Interface Anal.*, (2005), Submitted.
62. F. Reichel, L.P.H. Jeurgens, and E.J. Mittemeijer, *Phys. Rev. B*, (2006), in print.
63. P.C.J. Graat, M.A.J. Somers, and A.J. Boettger, *Surf. Interface Anal.*, **23** (1995), 44.
64. J.A. Woollam, *Guide to Using WVASE^{TM}*., J. A. Woollam Co. Inc., Lincoln, 1997.
65. F.H.P.M. Habraken, O.L.J. Gijzeman, and G.A. Bootsma, *Surf. Sci.*, **96** (1980), 482.
66. H.G. Tompkins, *A User's Guide to ELLIPSOMETRY*, (Academic Press, 1993).
67. B.E. Hayden, W. Wyrobisch, W. Oppermann, S. Hachicha, P. Hoffmann, and A.M. Bradshaw, *Surf. Sci.*, **109** (1981), 207.
68. P.C.J. Graat, M.A.J. Somers, and E.J. Mittemeijer, *Thin Solid Films*, **340** (1999), 87.

69. T.M. Christensen and J.M. Blakely, *J. Vac. Sci. Technol. A*, **3** (3) (1985), 1607.

70. J. Grimblot and J.M. Eldridge, *J. Electrochem. Soc.*, **129** (10) (1982), 2366.

71. R.A. Synowicki, *Thin Solid Films*, **313-314** (1998), 394.

72. M. Rauh and P. Wissmann, *Thin Solid Films*, **228** (1993), 121.

73. H. Kuroki, T. Kawabe, and M. Kitajima, *Solid State Communications*, **88** (10) (1993), 785.

74. P.R. Lefebvre, C. Zhao, and E.A. Irene, *Thin Solid Films*, **313-314** (1998), 454.

75. S. Deckers, F.H.P.M. Habraken, W.F.v.d. Weg, and J.W. Geus, *Appl. Surf. Sci.*, **45** (3) (1990), 207.

76. B.E. Hayden, E. Schweizer, R. Koetz, and A.M. Bradshaw, *Surf. Sci.*, **111** (1-2) (1981), 26.

77. R. Koetz, B. Hayden, E. Schweizer, and A.M. Bradshaw, *Surf. Sci.*, **112** (1981), 229.

78. M. Kurth, *The Initial Oxidation of Magnesium*. 2004, University of Stuttgart.

79. M. Losurdo, P. Capezzuto, and G. Bruno, *Phys. Rev. B*, **56** (16) (1997), 10621.

80. S.O. Saied and J.L. Sullivan, *J. Phys.: Condes Matter*, **5** (33A) (1993), A165.

81. F.J. Esposto, C.S. Zhang, P.R. Norton, and R.S. Timsit, *Surf. Sci.*, **302** (1-2) (1994), 109.

82. J. Bloch, D.J. Bottomley, J.G. Mihaychuk, H.M.v. Driel, and R.S. Timsit, *Surf. Sci.*, **322** (1-3) (1995), 168.

83. *Handbook of Optical Constants of Solids II,* Eds. E.D. Palik, (Academic Press, New York, 1991).

84. D.E. Aspnes, *Thin Solid Films,* **89** (3) (1982), 249.

85. T.J. Nijdam, L.P.H. Jeurgens, and W.G. Sloof, *Materials at High Temperatures*, **20** (3) (2003), 311.

86. R.M.A. Azzam, M. Elschazly-Zaghloul, and N.M. Bashara, *Applied Optics*, **14** (7) (1975), 1652.

87. P.C.J. Graat, M.A.J. Somers, and E.J. Mittemeijer, *Z. Metallkd.*, **93** (2002), 532.

88. M.S. Vinodh, L.P.H. Jeurgens, and E.J. Mittemeijer, (2005), communicated to *J. Appl. Phys.* (Chapter 4 in this thesis).

89. L.P.H. Jeurgens, M.S. Vinodh, and E.J. Mittemeijer, *Appl. Surf. Sci.*, (2006), in press, (Chapter 3 in this thesis).

90. L.P.H. Jeurgens, W.G. Sloof, F.D. Tichelaar, and E.J. Mittemeijer, *Phys. Rev. B*, **62** (2000), 4707.

91. *CRC Handbook of Chemistry and Physics*, edn. 85, Eds. D.R. Lide, 2004-05.

92. M. Hirsimaeki, M. Lampimaeki, K. Lahtonen, I. Chorkendorff, and M. Valden, *Surf. Sci.*, **583** (2005), 157.

93. J.C. Fuggle, L.M. Watson, D.J. Fabian, and S. Affrossman, *Surf. Sci.*, **49** (1975), 61.

94. J.C. Fuggle, *Surf. Sci.*, **69** (1977), 581.

95. G.C. Allen, P.M. Tucker, B.E. Hayden, and D.F. Klemperer, *Surf. Sci.*, **102** (1981), 207.

96. J. Ghijsen, H. Namba, P.A. Thiry, J.J. Pireaux, and R. Caudano, *Appl. Surf. Sci.*, **8** (1981), 397.

Curriculum Vitae

Personal

Name	M. S. Vinodh
Date and Place of Birth	13.11.1976, Erode, India
Marital Status	Married
Nationality	Indian

Schooling

1980 – 1994	Sri Vidya Mandir Higher Secondary School, Salem, India.

Higher education

June 1994 – May 1997	B. Sc (Physics), St. Joseph's College, Tiruchirapalli, India.
Aug. 1997 – May 1999	M. Sc (Materials Science), Anna University, Chennai, India.
Jan. 2000 – Aug. 2002	M. Sc (Engg.) in Instrumentation, Indian Institute of Science, Bangalore, India.

Dissertation

Sept. 2002 – Jan. 2006	Ph.D. at the Max-Planck-Institut für Metallforschung and Universität Stuttgart Title: "On the Initial Oxidation of MgAl Alloys".

Acknowledgements

The present work was performed at the Institut für Metallkunde in the Universität Stuttgart and at the Max-Planck-Institut für Metallforschung, Stuttgart.

My grateful acknowledgements to my research supervisor Prof. Dr. Ir. E. J. Mittemeijer for introducing me into this fascinating world of oxidation. I have immensely benefited from his stimulating discussions, valuable inputs and continuous encouragement. His enthusiasm and integral view on research and his mission for providing 'only high-quality work and not less', has made a deep impression on me.

I am greatly indebted to Dr. Lars P. H. Jeurgens for being such a wonderful advisor and friend. Working with him was a great learning experience – both academically and personally. This thesis would not have been what it is now but for his invaluable guidance, support, discussions and critical evaluation at each and every stage of my progress.

My special thanks to Friederike for taking the pain to write the German version of the summary at a very short notice.

My many thanks to all the collegues of both the Max-Planck Institutes for their assistance during my research and hearty thanks to my friends who made my stay at Stuttgart pleasant and enjoyable.